공학박사 학위논문

Study on the spin-orbit-coupled transport properties of prototype ferroelectric Rashba semiconductors (FeRSCs); α-GeTe

강유전 **Rashba** 반도체 재료인 α**-GeTe**의

스핀궤도 결합 전하수송특성 연구

2023년 2월

서울대학교 대학원

재료공학부

조 성 원

Study on the spin-orbit-coupled transport properties of prototype ferroelectric Rashba semiconductors (FeRSCs); α-GeTe

지도 교수 한 승 우

이 논문을 공학박사 학위논문으로 제출함
2023 년 2 월

서울대학교 대학원
재료공학부
조성원

조성원의 박사 학위논문을 인준함
2023 년 2 월

위 원 장 장 호 원 (인)

부위원장 한 승 우 (인)

위 원 강 기 훈 (인)

위 원 장 영 준 (인)

위 원 이 수 연 (인)

Abstract

Study on the spin-orbit-coupled transport properties of prototype ferroelectric Rashba semiconductors (FeRSCs); α-GeTe

Seong Won Cho

Dept. of Materials science and Engineering

The Graduate School

Seoul National University

The discovery of new electronics materials not only improves the performance of existing devices but also leads to the development of completely new functional devices. Ferroelectric Rashba Semiconductors (FeRSCs), as one of these material systems, feature the Rashba effect controllable by ferroelectric polarization. The Rashba effect coupled with the ferroelectricity enables the development of novel spintronics devices such as non-volatile spin-transistors. Germanium telluride (GeTe), a prototype ferroelectric Rashba semiconductor, is a material that is being actively studied in recent years due to its huge Rashba effect (Rashba constant, α_R= ~4.3eVÅ). Researchers have been focussing on theoretical calculations and verification of the Rashba band splitting by optical measurements, and by less than 10% of the total studies on electrical properties that have practical implications for spintronics. This seems to reflect the poor applicability compared to the high academic interest in the bulk Rashba effect of GeTe. The lack of research on the application of GeTe is associated with the metallic property of GeTe despite its ferroelectricity. The high hole concentration of

$10^{20}/cm^3$ or more of GeTe lowers the ferroelectric switching efficiency and adversely affects the Rashba effect. This thesis contains studies that are conducted to improve the applicability of GeTe, as a FeRSCs. Using a high-quality epitaxial GeTe thin film grown by thermal evaporation, the Rashba effect of GeTe was investigated based on electrical measurements such as magnetoresistance and harmonic Hall resistance. In addition, we attempt to reduce the carrier density of GeTe through the formation of a superlattice with bismuth telluride (Bi_2Te_3), an n-type topological insulator. The carrier density of GeTe was reduced by 1/10 improving ferroelectric switching efficiency and restoring the Rashba effect. This comprehensive research for utilizing GeTe as a FeRSCs, from the growth of GeTe thin films to basic characterization, application characterization, and superlattice research for carrier density reduction would provide a lot of motivation for the field of spintronics applications of FeRSCs.

Keywords: GeTe, epitaxy growth, bulk Rashba effect, ferroelectricity, superlattice, strong spin-orbit coupled system

Student Number: 2018-30391

Contents

List of Tables

List of Figures

Chapter 1.

Introduction

Germanium telluride (GeTe) is a chalcogenide material with a rhombohedrally distorted rock-salt structure which has a stoichiometry of Ge:Te = 1:1. Despite having a simple structure and stoichiometry, GeTe featuring interesting optical and electrical properties, has been actively studied since the mid-20th century [1-4]. In particular, GeTe's excellent properties of phase change memory (PCM), thermoelectric [5], and optoelectronic [6] have attracted much interest.

Recently, in addition to these traditional applications of GeTe, the potential of GeTe as a spintronics-applied material is starting to attract attention. Since Di Sante [7] reported through DFT calculation that a very large bulk Rashba effect can occur in GeTe in 2013, many related theoretical and experimental results have followed [8-12]. The bulk Rashba effect of GeTe is very special for the following two reasons, which make it promising as a spintronics application material.

The first is Rashba band splitting in the bulk state coupled with the ferroelectric (FE) polarization of GeTe. Unlike the surface Rashba effect, which is generally observed mainly in the 2D electron gas,

which can be modulated only when a gate voltage is applied, the ferroelectric coupled Rashba effect enables non-volatile Rashba effect modulation [13] through ferroelectric switching.

Second, the Rashba effect in GeTe has the largest value among the Rashba effects reported so far. The optically measured Rashba constant of GeTe is ~4.2 eV/Å [12], which corresponds to the largest value among the Rashba constants known to date.

These two special characteristics enable the development of new types of spintronics memory [7,14-16] devices such as non-volatile spin-transistors or the enhancement of performance of existing spintronics memories such as spin-orbit torque (SOT) magnetic random access memory (MRAM).

After the discovery of FeRSCs characteristics in 2013, studies related to GeTe as FeRSCs have steadily increased (Figure 1). Research can be classified into (1) electrical measurement and analysis, (2) Rashba band verification through optical spectroscopy such as angle-resolved photoemission spectroscopy (ARPES), and (3) theoretical band calculations through density functional theory (DFT).

As can be seen in Figure 1, research trends are biased towards spectroscopy and theoretical calculations, and electrical investigation, which is important for the actual device application, accounts for less than 10 % of the total. The lack of research on the spintronics

applications of GeTe may be due to the rich theoretical value of the bulk Rashba effect of GeTe, but on the other hand, it implies that the high electrical conductivity of GeTe impedes the spintronics applications of GeTe. The high conductivity which makes FE switching difficult limits the development of spintronics applications utilizing the ferroelectric coupled Rashba properties of GeTe. Against this background, in this paper, basic research for applying GeTe to spintronics was conducted as follows.

Chapter 2 introduces the growth and structural analysis of high-quality GeTe epitaxy thin films which are grown using thermal evaporation.

In Chapter 3, we measure carrier transport using the GeTe thin film grown in Chapter 2 and analyze the basic electrical properties and spin-orbit (SO) interaction of GeTe.

Chapter 4 introduces the experimental demonstration of the largest SO torque ever by measurement of the second harmonic Hall resistance in the GeTe/NiFe bilayer.

Chapter 5 introduces the experiment about forming a [GeTe|Bi_2Te_3] superlattice to reduce the p-type carrier density of GeTe, while maintaining the GeTe's Rashba effect.

This paper, which includes a comprehensive research of prototype FeRSCs; GeTe from thin film growth to basic characterization,

application characterization, and charge density engineering, is expected to provide a lot of inspiration for the development of new spintronics devices utilizing GeTe, which is currently stagnant.

Research on FeRSCs; GeTe

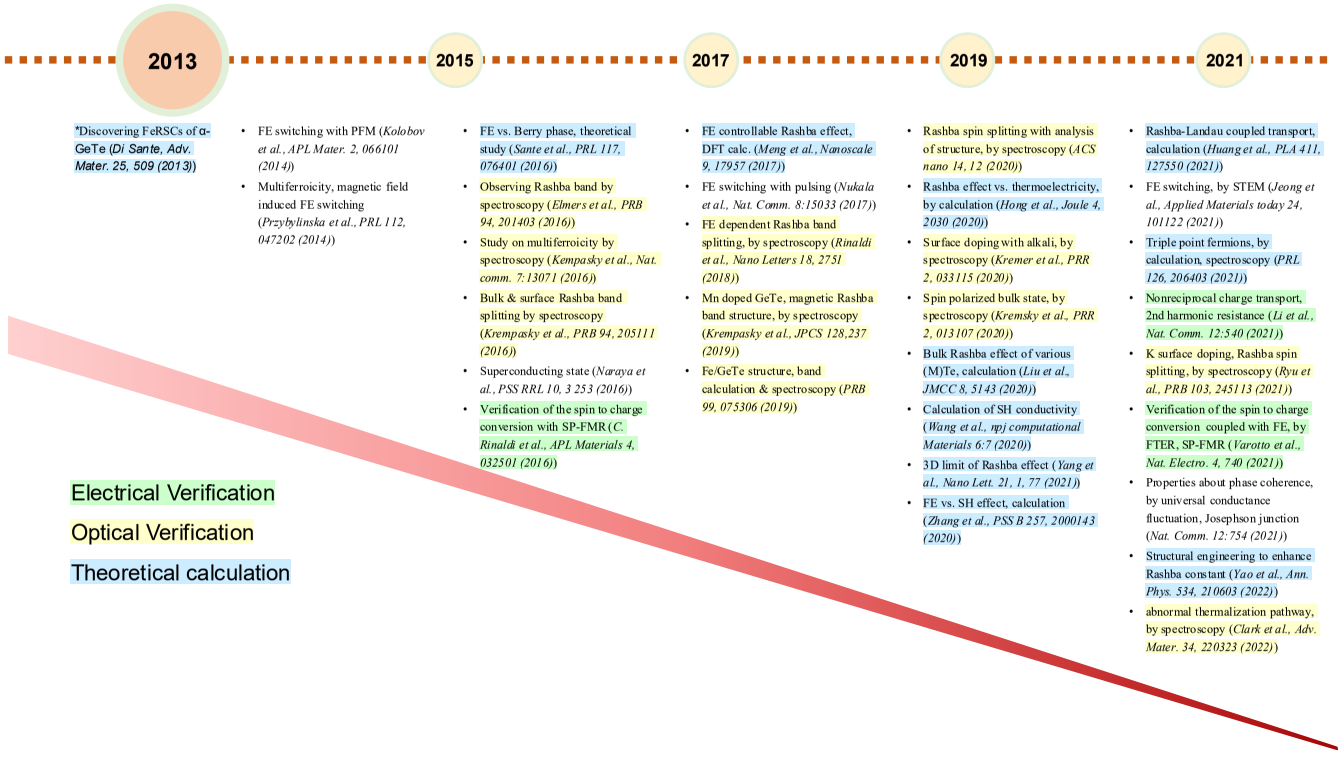

Figure 1. Research trends of GeTe as FeRSCs

1.1 Research Background

1.1.1 Spintronics

Starting with Albert Fert and Peter Grunberg's discovery of the giant magnetoresistance (GMR) effect [17,18] in 1988, it is widely known that the spin of electrons can have a significance on electronic transport beyond the origin of magnetic materials. The discovery of GMR marked the beginning of spintronics, leading to the development of hard disks and magnetic sensors, which dramatically increased the storage capacity of disks. Spintronics is a compound word of ‘spin’ and ‘electronics’ and refers to electronics that use not only the charge of electrons but also the spin as a degree of freedom of electronic devices. Unlike electronics, which use electric charges as a medium of information, Spintronics devices store and transmit information by bit formed by up spin and down spin of electric charges.

The first generation of spintronics, represented by GMR, utilizes spintronics devices driven by spin transport mechanisms. In Figure 1, a schematic diagram of the first-generation spintronics is expressed through the example of GMR. The current injected through one magnet FM1 transmits a spin whose direction is determined

according to the magnetization direction of the magnet. In general non-magnetic materials, the up-spin and down-spin of the charge are equal in amount, while the current injected through the magnet has a dominant spin direction aligned in the magnetization direction, which is called spin current. The spin current injected in this way maintains spin during spin relaxation time. Spin current exhibits a special transport properties described by the spin transport mechanism. When the direction of the spin injected into the adjacent magnet FM2 coincides with the magnetization, it is easily transmitted, otherwise high interfacial resistance occurs. This is the working principle of a GMR device consisting of a metal and two magnets surrounding it. Depending on whether the magnetization direction of the two magnets coincides or not, the resistance of GMR is determined and formed a 1bit. Unlike the fixed magnetization direction of FM1, FM2 can be switched to store the information in the GMR through an external magnetic field.

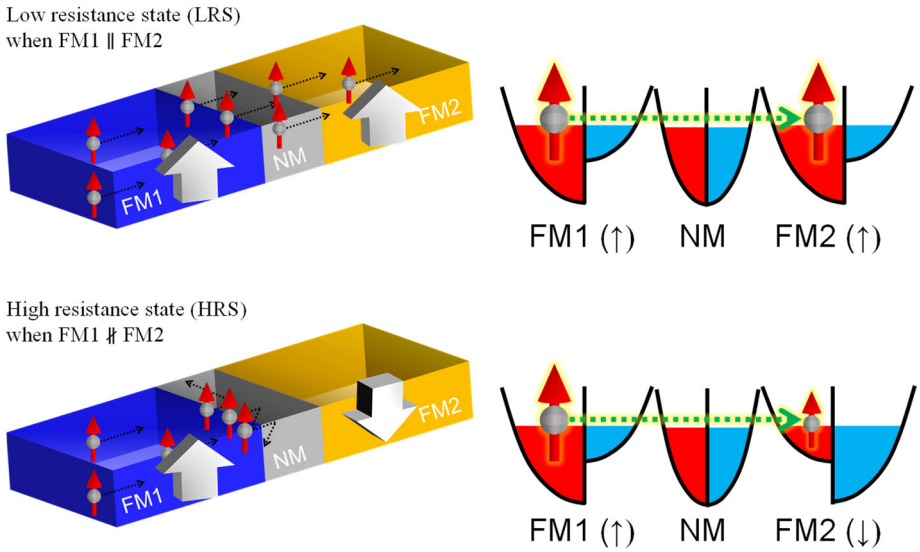

Figure 2. Schematic cartoon explaining the giant magnetoresistance (GMR).

The limitations of the first-generation spintronics come from the use of electromagnets. Since the hard disk used electromagnets for the magnetic switching, it requires a separate mechanical device to carry electromagnets to access each cell. This induced various drawbacks in durability, power efficiency, scaling, and reliability. So, there were demands for paradigm shifts to new spintronics without electromagnets.

Second-generation spintronics control spins through electrical electric fields and currents. The various 'charge to spin conversion mechanisms' such as, spin valve, spin Hall effect, and spin pumping are used for spin control through electrical stimulation [19,20]. A

typical application device is magnetic random access memory (MRAM), which is used as a unit device of a crossbar array. According to the spin injection method, MRAM is divided into two types: spin-orbit torque and spin-transfer torque (Figure 3).

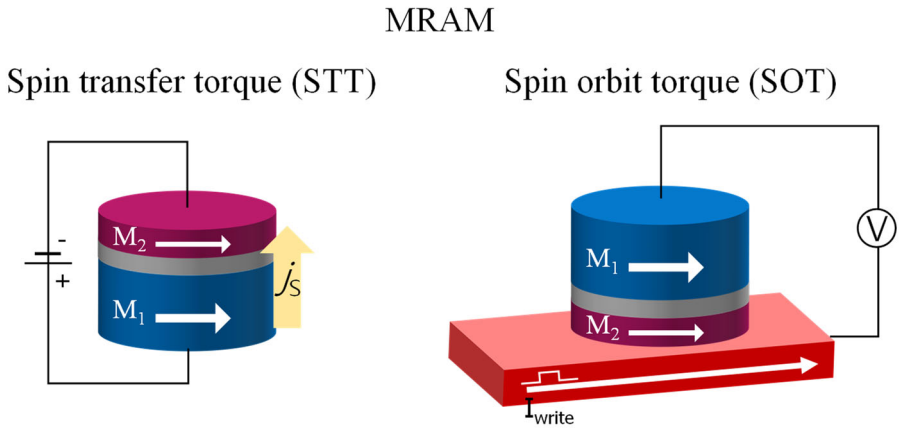

Figure 3. Schematic cartoon representing the MRAM according to STT and SOT schemes.

The STT scheme uses a spin valve mechanism for spin generation, and a spin current is injected from the fixed layer (M_1) to a free layer (M_2). The up or down spin of the injected spin current is determined according to the direction of the current ($M_2 \rightarrow M_1$ or $M_2 \rightarrow M_1$). Since the efficiency of spin injection is entirely determined by the spin polarization of the magnet and the oxide tunneling barrier, it has limited power efficiency. The SOT method utilizes a spin generation mechanism by the spin Hall effect (SHE) of the normal metal (NM)

having strong spin-orbit coupling adjacent to the free layer. There is no incubation time in the switching of the free layer in the SOT scheme, and the energy efficiency can be greatly improved according to the magnitude of the spin-Hall effect of the NM. Recently, the materials and devices capable of facilitating charge-to-spin conversion (or spin-to-charge conversion) such as voltage-induced change of magnetic anisotropy (VCMA) [21,22] have been attracting much interest.

1.1.2 Fundamental spin interactions

As mentioned in the above section, spintronics considers spin and charge transport simultaneously. As a spin of an electron has a unit magnetic moment (or Bohr magneton, m_B= 9.274 x 10^{-24} JT^{-1}), so the dynamics of spin are determined by the various magnetic interactions. This section contains conceptual explanations from basic magnetic interactions such as Zeeman, dipole-dipole, and exchange interactions to spin-orbit interactions closely related to the subject of this thesis.

Zeeman interaction

The spin of an electron is quantized into up (down) indicating clockwise rotation (counterclockwise rotation) based on the direction of an external magnetic field. Spin has angular momentum ($s = \pm 1/2\hbar$) and magnetic moment (μ=μ_B, Bohr magneton). Considering that the spin is the origin of the material's magnetism, of course, there is an interaction with an external magnetic field. What direction is stable for the spin in a magnetic field? The answer can be found in the equation for Zeeman interaction.

$$E_{Zeeman} = -\mu H_{ext}$$

When the direction of the external magnetic field and the magnetic moment coincide, the state satisfies the equilibrium condition with

negative Zeeman energy. That is, the physical meaning of the Zeeman interaction is that the spin prefers aligned with an external magnetic field. This is consistent with our intuition.

Dipole-dipole interaction

Similar to the electrical dipole-dipole interaction, there is an interaction magnetic dipole-dipole interaction. It tends to align in the same direction while acting as an external magnetic field between adjacent magnetic moments. Magnetic dipolar energy is expressed as follows.

$$E_{dipole} \sim \frac{1}{r^3}(\mu_1 \cdot \mu_2 - \frac{3}{r^2}(\mu_1 \cdot r)(\mu_2 \cdot r)$$

It is noted that the size of the dipole-dipole interaction is significantly smaller than other magnetic interactions (eg. Exchange interaction).

Exchange interaction

Ferromagnets are featured as having spontaneous and permanent magnetization, through the alignment of their internal spins in the same direction. The aforementioned dipole-dipole interaction is also a force to align adjacent spins in the same direction but is not large enough to explain ferromagnetism. To explain ferromagnetism, we need to consider the exchange interaction.

The origin of the exchange interaction, which is the strongest magnetic interaction in materials, is interestingly closely related to the Coulomb interaction, which is an electrical interaction. Exchange interaction can be explained by considering the competition of electron kinetic energy, Pauli exclusion principle, and Coulomb energy. It is pointed out that the effect is closer to an effective interaction rather than a fundamental interaction. A schematic diagram is shown in Figure 4 for an intuitive understanding of Exchange interaction.

According to the Pauli exclusion principle, pairs of electrons in one energy state have different spins. Considering that there is no probability that an electron pair with the same spin exists, the physical distance between adjacent electrons of the same spin increases, so that the Coulomb energy has an energy gain compared to when two electrons of opposite spins are located in the same state. At this time, since only one spin is located in the two positions of up and down spin, the remaining electrons that are not located go up to a higher energy state and lose kinetic energy. If the gain of Coulomb energy is greater than the loss of kinetic energy, adjacent electrons have the same spin. Exchange interaction energy is shown below:

$$E_{exchange} = -\sum Jm_i m_j$$

Where, J is an exchange coupling constant that can have both positive

and negative signs. A negative exchange interaction generates anti-ferromagnetism, in which the spins of adjacent electrons are antiparallel to each other.

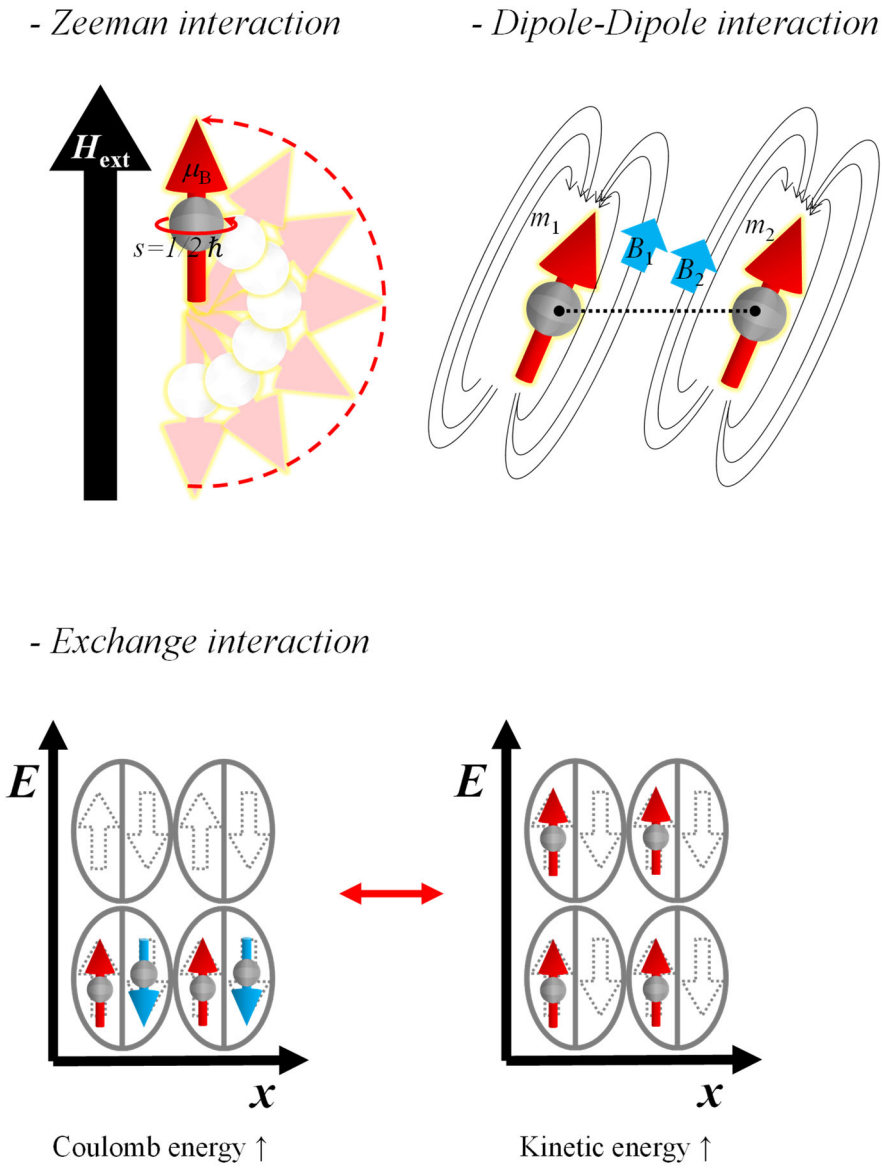

Figure 4. Schematic cartoon representing fundamental magnetic interactions

1.1.3 spin-orbit interaction (SOI)

Spin-orbit (SO) interaction is the magnetic interaction that will be discussed the most in this thesis. The SO interaction not only provides an important idea of how to control the spin of electrons with electric fields, but also hints at academic curiosity about the origins of magnetic fields and electric fields.

Before considering the general SO interaction, let us first consider the atomic spin-orbit interaction. The SO interaction refers to the interaction between the electron spin and the orbital which can be expressed by:

$$H_{so} = -\lambda \mathrm{s} \cdot \mathrm{L}$$

Here, λ is the SO interaction constant, and s and L are the spin and orbital angular momentum, respectively. It can be seen that the formula is very similar to the Zeeman energy, implying that spin and orbital act as effective magnetic fields for each other (Figure 5). For an intuitive understanding, consider Ampere's hand law, which determines the magnetic field that occurs when an electric current flows. Electrons moving in a counterclockwise circular motion around the nucleus can be thought of as a clockwise current loop. At this time, the direction of the magnetic field that penetrates the paper is determined by Ampere's hand law. At this time, it is safe to understand the Zeeman interaction of the magnetic field (induced by

orbital motion) and the electron spin as SO interaction. We introduce Zeeman energy for understanding, but point out that SO interaction and Zeeman interaction are not the same. As can be seen from the above equation, the SO interaction involves a SO interaction constant, λ.

λ depends on the electronic structure of the element and can be simplified to $\frac{Ze^2}{2m^2c^2r^3}$.

A spin-orbit interaction is an interaction between an orbital and a spin angular momentum and determines the state of the spin bound to a specific orbital. Therefore, because spin and orbital are coupled, spin-orbit interaction is sometimes referred to as spin-orbit coupling.

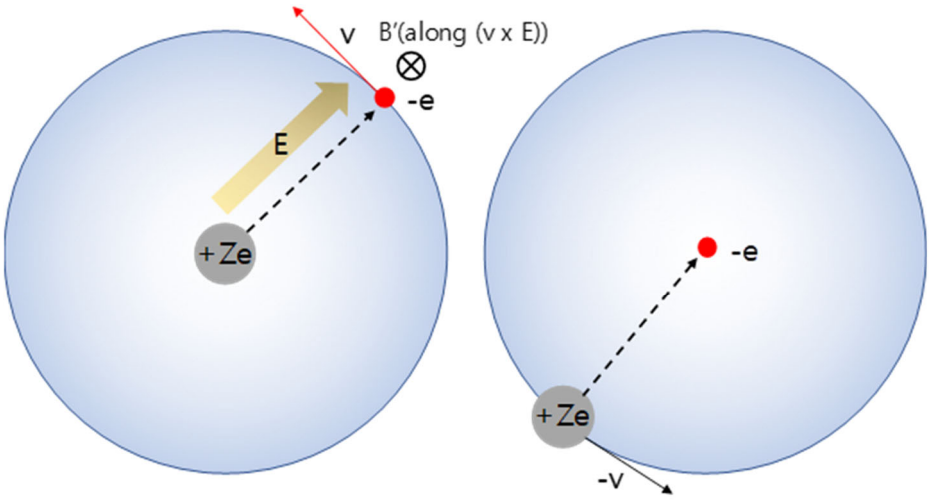

Laboratory rest frame Electron rest frame

Figure 5. Schematic diagram of the spin orbit interaction in an atom.

Let's extend the atomic SO interaction to a general situation. The SO interaction energy under the general potential $\phi(r)$, not the central force potential like an atom, is expressed as follows.

$$H_{so} = \lambda s\big(p \times \nabla\phi(r)\big)$$

where p is the momentum of the electron. Recalling the formula expressing Zeeman energy, $p \times \nabla\phi(r)$ can be thought of as a magnetic field acting on the spin of an electron.

How is the cross-product of electron momentum and the potential gradient connected to the magnetic field? This effective magnetic field can be explained from a microscopic perspective through the theory of relativity. According to the special theory of relativity, the interconversion of physical quantities occurs between the moving coordinate system and the stationary coordinate system. This transformation is called a Lorentz transformation. Figure 6 shows an example of the Lorentz transformation for the effective magnetic field received by a charge moving in the vertical direction in an electric field. A charge moving perpendicular to the electric field is equivalent to receiving a magnetic field perpendicular to both the electric field and the direction of motion. In Figure 5, Ampere's law is introduced for easy access, but this can also be generally explained

by Lorentz's transformation. An electric field in the direction of centrifugal force exists between the nucleus and orbiting electrons. Considering the circular motion direction and the centrifugal force direction, the effective magnetic field by Lorentz transformation is consistent with the analysis through Ampere's law.

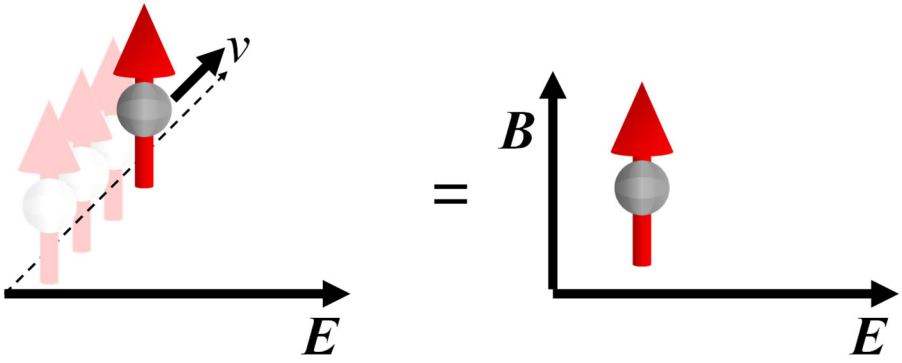

Figure 6. The effective magnetic field which a spin experience from spin-orbit interaction.

Since the potential of atomic nuclei felt by electrons in the material is very large, electrons moving between atomic nuclei undergo spin-orbit interaction. In general solid materials, the nuclear potential is mostly canceled by the periodicity of the crystal, but when the periodicity is destroyed for various reasons, the influence of spin-orbit interaction emerges. The breaking of periodicity can be derived by the extrinsic factors (refer to all defects such as impurities, point defects, and line defects, ...), and by the intrinsic factors (the surface

or interface, intrinsic non-centrosymmetric crystal,…). The intrinsic spin-orbit interaction can be strictly interpreted through the Berry phase obtained through the integration of the curvature of the electronic band.

Time and spatial inversion symmetry

From the previous sections, it was confirmed that the effective magnetic field acting on the moving electrons under the potential gradient is the essence of the SO interaction. Since this effective magnetic field is dependent on the direction of the electron momentum, the opposite effective magnetic field acts on the opposite momentum. That is, the energy of electrons due to SO interaction, ΔE, satisfies the following relationship.

$$\Delta E(k, s_{\uparrow}) = -\Delta E(k, s_{\downarrow}) \quad \text{..... (1)}$$

Also, if time-reversal symmetry is preserved, the following relationship is satisfied.

$$\Delta E(k, s_{\uparrow}) = \Delta E(-k, s_{\downarrow}) \quad \text{..... (2)}$$

If spatial inversion symmetry is preserved, $\Delta E(k, s_{\uparrow}) = -\Delta E(-k, s_{\uparrow})$ and $\Delta E(k, s_{\downarrow}) = -\Delta E(-k, s_{\downarrow})$ are satisfied. $\Delta E(k, s_{\uparrow}) = \Delta E(k, s_{\downarrow}) = -\Delta E(-k, s_{\downarrow}) = -\Delta E(-k, s_{\uparrow})$ leads to a

trivial conclusion. This is the same as the energy band in a normal spin degenerated metal. Although SO interaction exists in all atoms, it can be seen that inversion symmetry breaking is essential for SO interaction to work in a solid-state material.

In addition, considering the case where time-reversal symmetry is not preserved,

$$E(k, s_{\uparrow}) \neq E(-k, s_{\downarrow}) \quad \text{..... (3)}$$

Considering (1) and (3) simultaneously, $-E(k, s_{\downarrow}) \neq E(-k, s_{\downarrow})$ is established, so it can be seen that the spin degeneracy at k=0 is destroyed. It is pointed out that the Rashba spin-orbit interaction, discussed later, occurs in the condition that the time reversal symmetry is preserved and the inversion symmetry is broken.

Rashba spin-orbit interaction

The Rashba effect is one of the representative intrinsic spin-orbit interactions. The Rashba effect is mainly known for the SO interaction in 2d electron gas whose inversion symmetry is structurally broken at the surface or interface, but it was originally discovered for the first time in 3d materials. In 1959, Rashba report the Rashba effect in a zinc-blende structure with broken centrosymmetric. Then, in 1984, Bychkov and Rashba proposed a theory to interpret linear spin-band-splitting in a 2D system [23].

Since then, the 2D Rashba effect has been utilized for the development of spin-transistor or spin-orbit torque MRAM. The Rashba effect has led to relevant active research at the heart of spintronics history for about 30 years [24,25].

The Rashba spin-orbit interaction energy can be included in the free electron energy as follows.

$$E_R = -\alpha_R s \cdot (k \times z) + \frac{\hbar^2 k^2}{2}$$

Here, α_R is the Rashba constant, s is the spin quantum, k is the in-plane (x-y plane) momentum, z is the direction vector of the z-axis, and $\hbar$ is the reduced Planck constant. The Rashba energy term, $-\alpha_R s \cdot (k \times z)$, which has a linear dependence on the momentum, induces Rashba spin splitting (Figure 7).

There another intrinsic spin-orbit interaction caused by a periodic disruption in crystals is the Dresselhaus effect as well as the Rashba effect. The two can be distinguished according to how the spin texture is formed on the Fermi surface (Figure 8).

The 3D Rashba effect, which is the main subject of this thesis, received attention again in 2011 when K. Ishizaka [26] reported the bulk Rashba effect with a Rashba constant of 3.85 eVÅ in BiTeI. After that, in 2013, Di Sante reported a bulk Rashba effect with the Rashba constant of 4.3 eVÅ in GeTe, and interest in the 3D Rashba

effect continues to increase. The 3D Rashba effect in BiTeI and GeTe featuring the very large Rashba effect induced by a spontaneous electrical dipole in the material, that is, ferroelectric polarization. 3D Rashba semiconductors coupled with ferroelectricity have provided a lot of inspiration for the development of spintronics devices that improve functionality and energy efficiency [27-29].

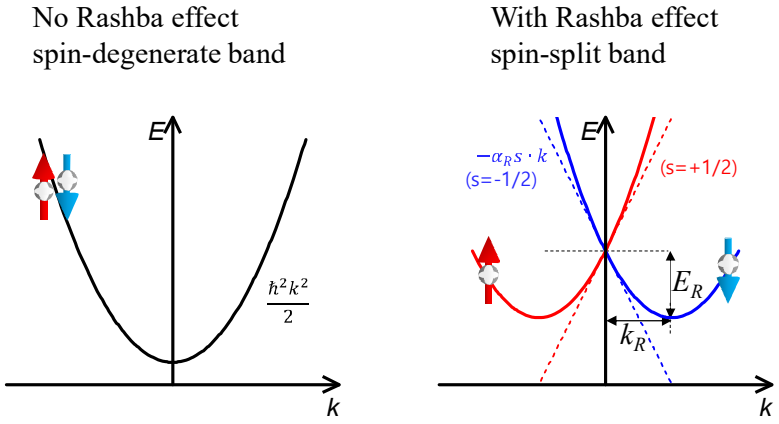

Figure 7. Schematic representation of the Rashba splitting band.

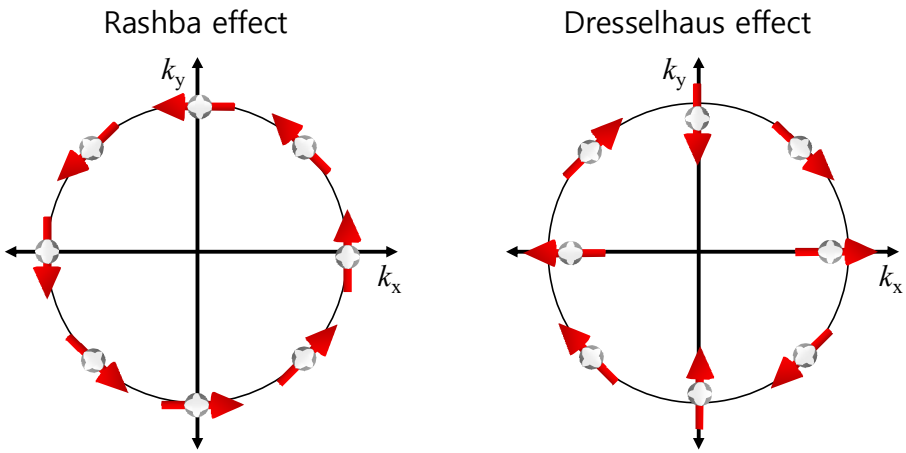

Figure 8. Fermi surfaces with the spin texture of Rashba and Dresselhaus effects.

1.1.3 Magneto-transport and Various Hall effects related to SO coupling

Hall effect

The Hall effect, first discovered by Edwin Hall in 1879, is caused by the Lorentz force (F_y) (which consequently induces Hall current, I_y) which direction is perpendicular to V_x and H_z when a charge moves under the perpendicular magnetic field (H_z). As an example of the Lorentz transformation mentioned in the spin-orbit interaction

section, we found that the momentum of the charge perpendicular to the direction of the electric field causes the effective magnetic field perpendicular to these two directions to generate the SO interaction. It is noteworthy that the Hall effect also can be explained by Lorentz transformation. The electric field in a direction perpendicular to the magnetic field can be interpreted as a Lorentz transformation into momentum in a direction perpendicular to these two directions.

Quantum Hall effect, Spin Hall effect, Anomalous Hall effect, etc. have in common that momentum is generated in the direction perpendicular to the direction of the electric field, even if the mechanisms are all different. In particular, the Hall effect caused by an external magnetic field is classified as the ordinary Hall effect.

Spin Hall effect & Anomalous Hall effect

Spin Hall effect (SHE) and Anomalous Hall effect (AHE) are Hall effects that occur without an external magnetic field. In addition, it has intrinsic commonality in that it is the Hall effect by SO interaction (usually the Hall effect is a phenomenon in which a current in the vertical direction of the induced current occurs, regardless of the mechanism). SHE and AHE generate a spin-dependent transverse current, that is, a spin current. AHE can be regarded as SHE

appearing in a ferromagnet, and since a ferromagnet has spin polarization, the spin current induced from AHE immediately generates charge current.

How does an SO interaction generate a transverse spin current? Let's understand the SHE generation process intuitively through the schematic of the mechanism of extrinsic SHE shown in the left panel of Figure 9.

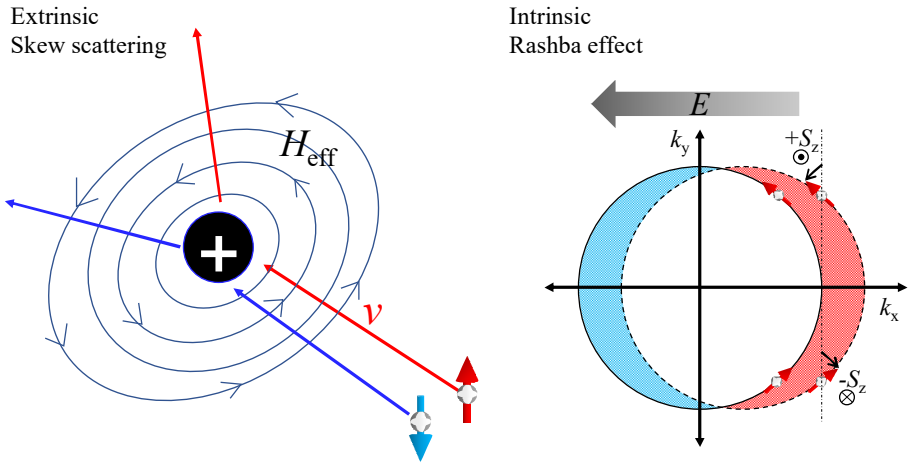

Figure 9. Intuitive explanation of the extrinsic and the intrinsic SHE

Electrons moving in the material collide with atomic nuclei and are scattered. It is emphasized that atomic nuclei here refer to atomic nuclei of point defects, not atomic nuclei in an innocent crystal (electrons in an innocent crystal do not feel the potential of atomic nuclei). Recalling the atomic SO interaction model, it can be expected that an effective magnetic field is generated around the nucleus of a positive charge (consider the electric field from the nucleus and the direction of electron movement). The directions of the effective magnetic fields on the right and left sides of the nucleus are opposite to each other, so it can be expected that the spins in opposite directions favor scattering in opposite directions. This

describes Skew scattering, a representative example of extrinsic spin scattering. Skew scattering has a very short time and length scale, so it usually does not contribute much to SHE.

Unlike extrinsic, the SHE of the intrinsic mechanism is not affected by defects and is completely determined by the electronic band structure. Let's take a look at the intrinsic SHE through the example of the Rashba system shown in the right panel of Figure 9. An electric field applied in the -x direction shifts the Fermi surface. The spin of the electron that has gained new momentum is rotated to a new spin state determined by the momentum (the Rashba field drives this spin rotation). The Rashba field induces spin precession and gives the z-axis component to the spin lying on the existing x-y plane. As a result, momentum in the y-axis direction obtained spin polarization in the z-axis direction. For the current applied to the x-axis, it leads to the current in the y-axis direction with z-axis spin polarization.

Chapter 2.

Growth and characterization of α-GeTe films

2.1 Introduction

Germanium telluride (GeTe), which refers to a compound containing Ge and Te in a 1:1 ratio, is one of the chalcogenides glass materials. Since GeTe has traditionally been studied as the applied materials for optical memory devices [30-32], phase change memory devices [33-37], and thermoelectric devices [38-40], the amorphous or polycrystalline GeTe films was most desirable. Rashba band splitting [7] in the electronic structure of α-GeTe reported by Di Sante in 2013 is behind the increased demand for single crystalline GeTe. To observe and utilize the bulk Rashba effect of α-GeTe, crystallinity as a single crystal is required, because the bulk Rashba effect resulting from ferroelectric polarization is canceled if the crystallinity is poor or does not have a consistent direction. Methods such as sputtering [41,42], pulsed laser deposition [43-45], and molecular beam epitaxy [46-48] have been tried for the epitaxy of α-GeTe, and most of the successful results adopt the MBE method. . Although the excellentness of the α-GeTe thin film grown by MBE has been sufficiently verified experimentally, its industrial applicability is not good due to low productivity and high cost.

On the other hand, thermal evaporation can be used in a lower base pressure (~10^{-8} Torr) than MBE, which requires a base pressure of 10^{-10} Torr or higher, does not require additional equipment such as reflection high-energy electron diffraction (RHEED), and has a high growth rate. In that, it has high productivity that can be used in actual industrial sites.

This chapter introduces the epitaxy method of α-GeTe through thermal evaporation, which has the advantage of high productivity compared to MBE. A systematic investigation was conducted on the growth conditions (substrate, growth temperature, growth rate, and flux ratio) that have a decisive influence on the growth of the thin film. The characteristics of the grown GeTe epitaxy thin film are verified through the structural analysis of AFM, XRD, TEM, and THz second harmonic generation.

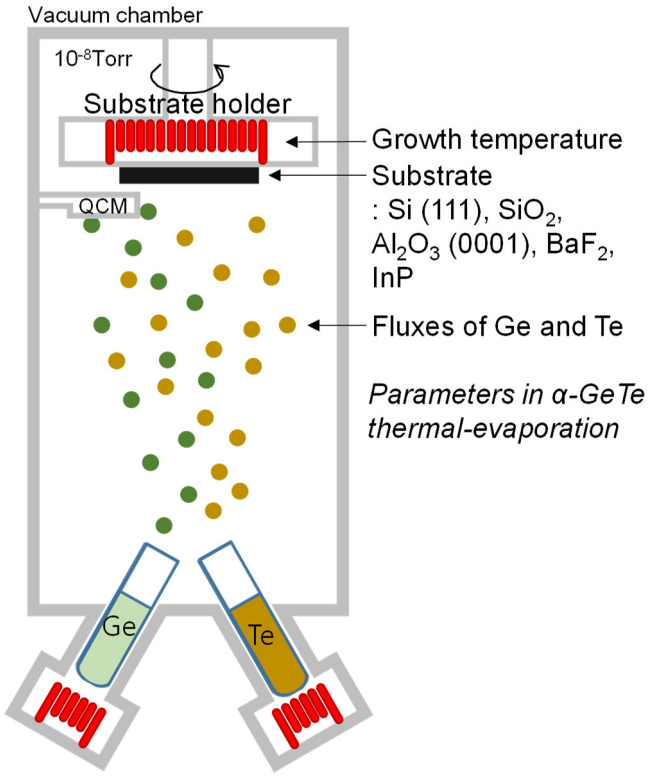

Figure 10. Schematic cartoon of the thermal evaporation system used for the epitaxy of α-GeTe thin film.

2.2 Method

Figure 9 shows a schematic diagram of the homemade thermal evaporator used for the epitaxy of α-GeTe thin films. The thermal evaporator is equipped with five Knudsen-type effusion cells, so each atomic source is vaporized independently. The distance between the substrate and the effusion cell is about 400 mm. The substrate holder was rotated off-axis for the homogeneity of the thin film during the growth process. An atomic source of Te and Ge was charged into the crucibles, and it was heated to a temperature at which the intended flux is obtained in the range of 250~320 ºC and 1400~1500 ºC, respectively (since the location of the thermocouple temperature sensor is different for each effusion cell, it is difficult to attach much meaning to). The flux of each atomic source was monitored through quartz crystal microbalance (QCM). The Ge and Te fluxes were set in the range of 0.1-0.5 Å/s and 0.5-2.5 Å/s, respectively. The GeTe thin film was grown with a deposition rate of up to 0.07 nm/s. The growth temperature was set using a Ta block heater mounted on the substrate holder. The growth temperature was accurately calibrated using a thermocouple attached to the substrate. Grown GeTe thin films in which all growth condition is systematically mapped were investigated to establish the optimum condition of the substrate, growth temperature, Te/Ge flux ratio, and growth rate. The structure of the grown GeTe thin film was analyzed by AFM, XRD, SEM, and

TEM measurements, and electrically by basic transport measurements of resistance, mobility, and carrier density.

2.3 Result and discussion

2.3.1 Substrate

Compatibility with the substrate must be considered first for epitaxial thin film. Since film is grown in the same direction as the substrate direction, it is difficult to grow crystals with the intended growth direction and good quality without considering the atomic symmetry and lattice mismatch of the substrate surface. α-GeTe of the rhombohedral crystal structure (*R3m* space group) has hexagonal symmetry with the (0001) plane (Figure 11). Also, Ge layer sandwiched by Te layers, which are shifted to one side on the same axis, form spontaneous electrical dipoles throughout the crystal (Figure 12). Considering that the Rashba effect is strongest in the momentum in the direction perpendicular to the ferroelectric polarization, the (0001) growth direction is an ideal growth direction that meets our purpose. Table 1 summarizes various candidate substrates with hexagonal symmetry. In consideration of human hazard, accessibility, electrical resistance, and process compatibility as well as the lattice matching, SiO_2, intrinsic Si (111), p-type Si (111), miscut Si(111) Al_2O_3 (0001), and InP (111) substrate were used in the experiment. The growth conditions were all the same as Te flux (r_{Te}=

2.5 Å/s), Ge flux (r_{Ge}= 0.5 Å/s), thickness=50 nm, and growth temperature (T_g= 250 ºC) except for the substrate.

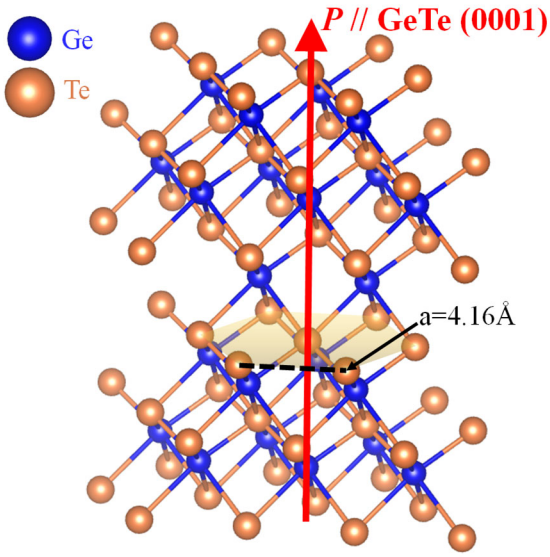

Figure 11. Crystal model of GeTe.

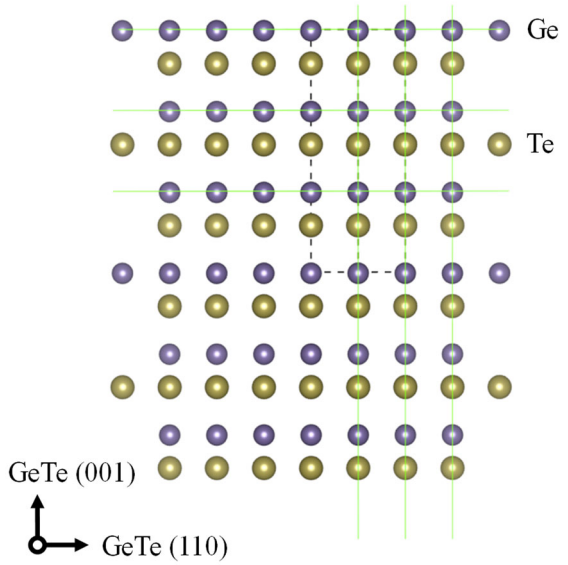

Figure 12. Crystal model of GeTe with zone axis (100).

Table 1. Summary of various substrates for the growth of GeTe

	GeTe (111)	Sb_2Te_3 (0001)	Bi_2Te_3 (0001)	Bi_2Se_3 (0001)	Al_2O_3 (0001)	Si (111)	Ge (111)	GaAs (111)	GST225 (111)
a [Å] (hexagonal lattice vector)	4.16	4.26	4.39	4.14	4.79	3.83	4.00	4.00	4.22
mismatch with GeTe [%]	-	2.55	5.47	-0.43	15.08	-7.93	-3.80	-3.91	1.61
	Mica (0001)	**ZnS (111)**	**CdS (111)**	**GST326 (111)**	**GST124 (111)**	**SrTiO3 (111)**	**BaF2 (111)**	**MgO (111)**	**InP (111)**
a [Å] (hexagonal lattice vector)	5.20	3.78	4.14	4.21	4.23	5.52	8.76	5.96	4.15
Mismatch with GeTe [%]	25.07	-9.16	-0.43	1.26	1.74	32.82	5.37	-28.37	-0.19

Surface characteristics

Figure 13 shows visual observation images of 50 nm GeTe thin films grown on SiO_2, p-type Si (111), intrinsic Si (111), and miscut Si (111). Through visual observation, the glossiness of the surface is clearly distinguished. In the case of SiO_2, over the entire area, p-Si(111) shows hazy surface properties locally. In the case of i-Si (111) and miscut Si (111), they show completely shiny surface properties over the entire area. To confirm the origin of hazy surface properties, SEM measurements were performed, and the results are shown in Figure 15. The SEM measurement includes the result of the Al_2O_3 substrate, which was impossible to measure by AFM itself due to the severe roughness of the surface. In the SEM image, it can be seen that the morphology according to the substrate is clearly distinguished. In the visual observation, except for shiny i-Si (111) and miscut Si (111), irregularly grown hundreds of nm nano-wires can be observed. In the GeTe thin film growth process, nanowires are commonly generated [49,50]. Nanowires can grow when the substrate temperature is too low or the beam flux is too high for the adatom to spread a sufficient distance over the substrate [51]. Considering that the growth conditions except for the substrate are the same, it seems that the poor conformation between SiO_2 and Al_2O_3 promotes the nanowire growth.

Because poor conformity with the substrate increases the interface energy, it favors the island growth mode rather than layer-by-layer growth, which increases the interface area, and promotes the growth of nanowires.

Another thing to note about the surface properties is that the growth properties are different depending on the doping concentration even for the same Si (111) substrate. A local hazy surface was observed in the GeTe thin film grown on the p-type Si (111) substrate (Figure 13), which is confirmed by the SEM (Figure 15) and AFM (Figure 14)) images. It is confirmed that the GeTe thin film on p-type Si (111) has poor crystal quality compared to the intrinsic substrate, such as a large number of in-plane rotational domains in addition to simple nanowire growth. The p-type Si (111) substrate was grown by the general Czochralski (CZ) method, whereas in the case of the intrinsic Si (111) substrate, a float zone (FZ) method was applied to remove defects and impurities in the Si crystal. It can be confirmed that the impurity and bonding concentration of the substrate has a decisive effect on the epitaxy thin film quality. In GeTe grown on a vicinal Si (111) substrate with a miscut angle of 3°, a clearly observed facet is prominent. Without a rotational domain, first, well-aligned surface properties in the growth direction are confirmed. The flattest and most well-aligned surface properties on InP (111) substrates with the smallest 0.19 % lattice mismatch among the investigated substrates

highlight the importance of substrate conformance in epitaxy (Figure 14).

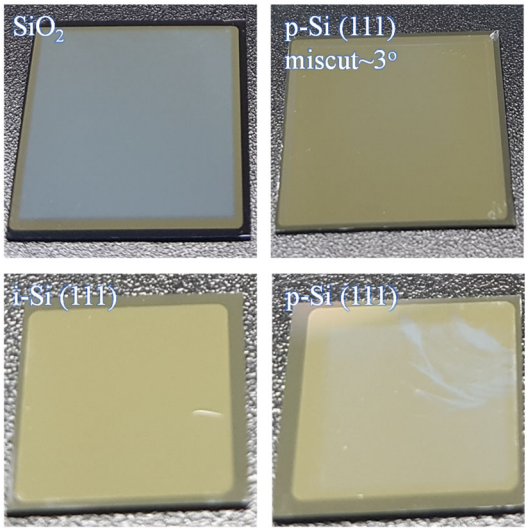

Figure 13. Photograph of grown GeTe films on SiO_2, p type Si (111), intrinsic Si (111), and miscut Si (111).

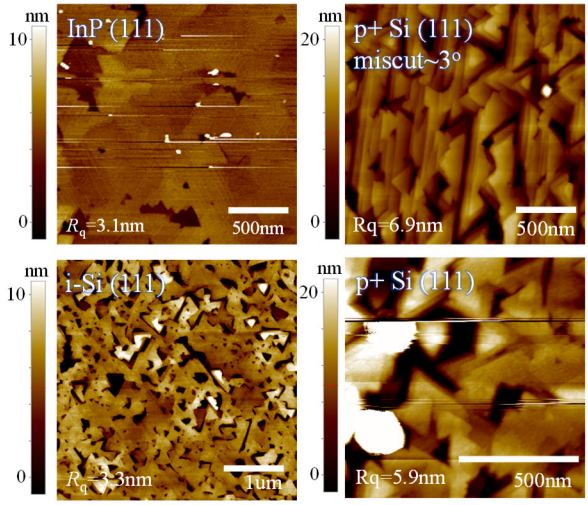

Figure 14. AFM images of grown GeTe films on InP (111), miscut

Si (111), intrinsic Si (111), p type Si (111).

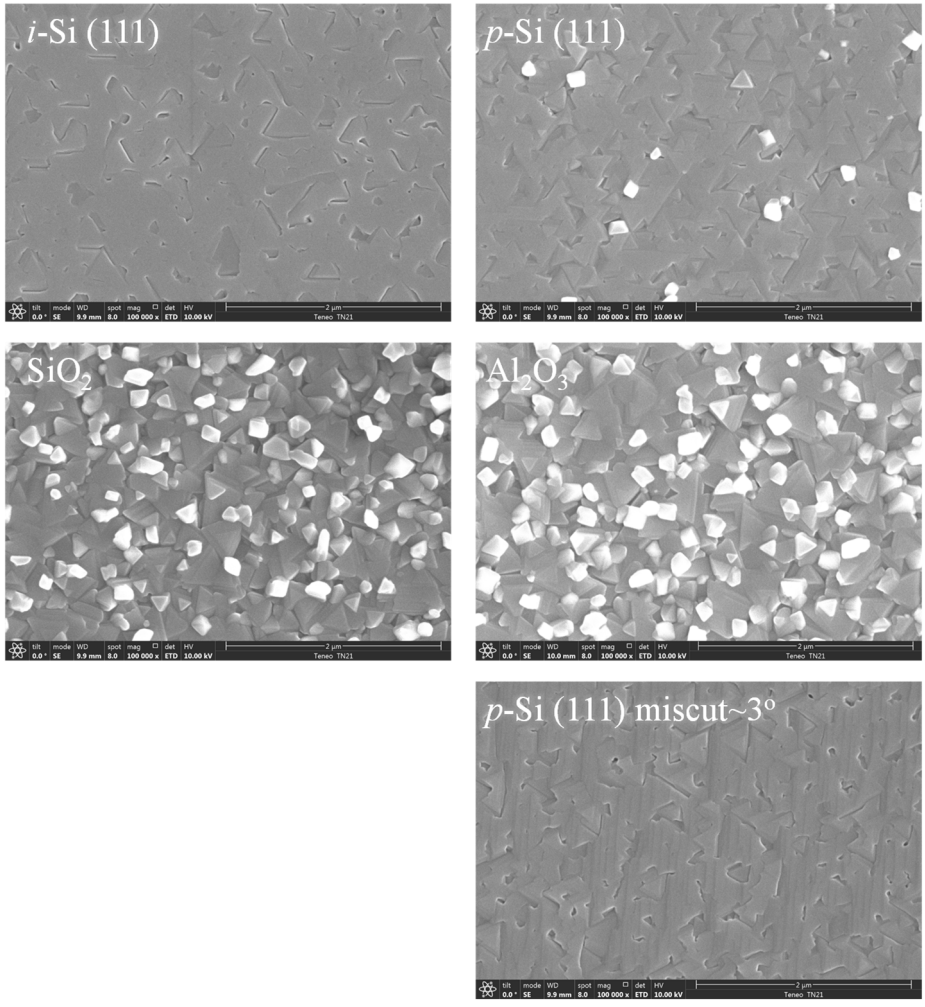

Figure 15. SEM images of grown GeTe films on intrinsic Si (111), p type Si (111), SiO_2, Al_2O_3 (0001), and miscut Si (111) substrates.

XRD analysis

XRD measurement was performed to evaluate the crystallinity of the grown GeTe thin film. Figure 16 shows the XRD theta-2theta result indicating the out-of-plane growth direction. In the SiO_2 and Al_2O_3 substrates that do not match GeTe or have very large lattice mismatch, the prepared orientation in the (0001) direction is weakly confirmed, but the XRD peak intensity of the noise level is confirmed. As only the harmonics of GeTe (0001) are observed in the XRD theta-2theta measurement results of the remaining substrates, the prepared orientation toward the c-axis is clearly confirmed. The peak intensity relative to the substrate peak is the best in the i-Si (111) and InP (111) substrates, and the XRD peaks of the p-Si (111) and miscut (111) substrates show similar relative intensities.

Figure 20 shows the XRD ω-scan (or rocking curve) result, which can estimate the gradient uniformity of the growth thin film, that is, mosaicity. Full width at half maximum (FWHM) was found to be 0.155°, 0.44°, 1.09°, and 0.126° for i-Si (111), p-Si (111), miscut Si (111), and InP (111), respectively. The excellent mosaicity in the InP (111) substrate, which is significantly lower in the p-type Si (111) substrate than in the intrinsic Si (111) substrate, is consistent with the

results expected from the surface properties. However, the FWHM of the miscut Si (111) substrate is 1.09°, which shows the worst mosaicity among the compared substrates, and it is difficult to predict from the surface characteristics results. The reason why vicinal substrates are advantageous for epitaxy growth of thin films is that relatively many steps and terraces of vicinal substrates promote nuclear growth, making it easy to achieve layer-by-layer growth. However, the Si (111) substrate has a very large lattice mismatch of about ~8 % with GeTe, and the extension of the interface region strengthens the relaxation tendency of the thin film. The GeTe thin film, which did not match with the miscut Si (111) substrate at the early stage of growth and was fully relaxed, seems to be a factor that deteriorates the gradient uniformity with the substrate. Figure 17 shows the enlarged GeTe (0003) peak region in the XRD theta-2theta result. Unlike the intrinsic Si (111) substrate, where only a single peak is clearly observed, a double peak structure is confirmed in miscut Si (111).

Figure 21 shows the results of the XRD phi scan measured to confirm the in-plane crystal symmetry. 6-fold symmetry implying a mirror twin domain is confirmed in all intrinsic Si (111), p type Si (111), and miscut Si (111) substrates. It is known that the crystal of the *R3m* space group of GeTe ideally has 3-fold symmetry, but the twin domain is formed very easily [43,52]. It is emphasized that if the

ferroelectric polarity is the same, the presence or absence of twin domains does not change the chirality of Rashba splitting. As a result of XRD phi scan, a major peak having high intensity and a minor peak having a low intensity are observed simultaneously with the major peak and a minor peak 60° apart. If the degree of twin domain is estimated from the ratio of major peak / minor peak, the degree of twin domain is the smallest in the intrinsic Si (111) substrate. The width of the XRD phi scan peak was also the smallest in intrinsic Si (111), which means the smallest degree of rotational domains.

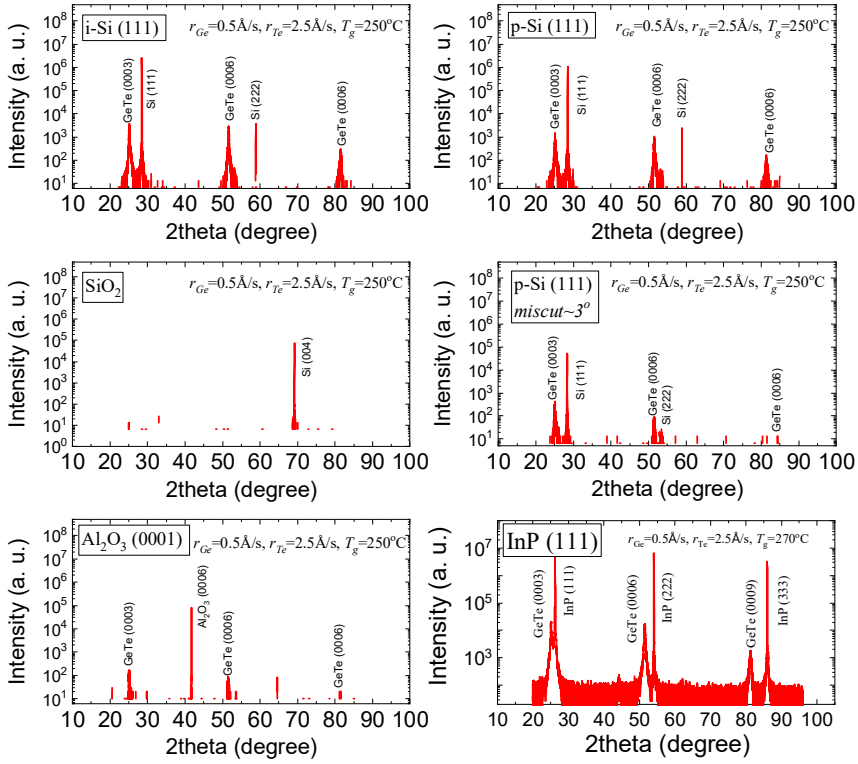

Figure 16. XRD theta-2theta scans of GeTe films grown on various substrates.

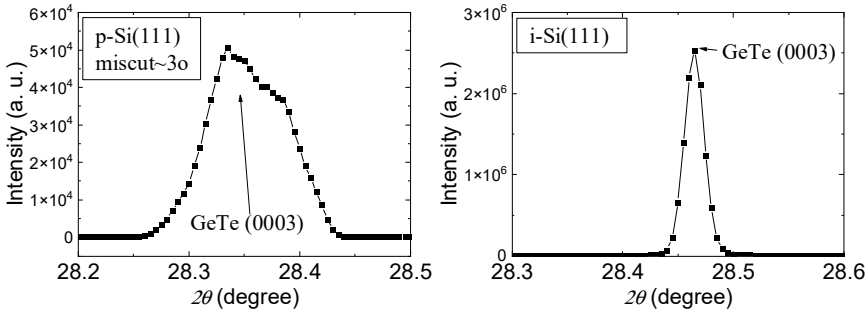

Figure 17. Magnified XRD theta-2theta scans of GeTe (0003) grown on miscut Si (111) and intrinsic Si (111) substrates.

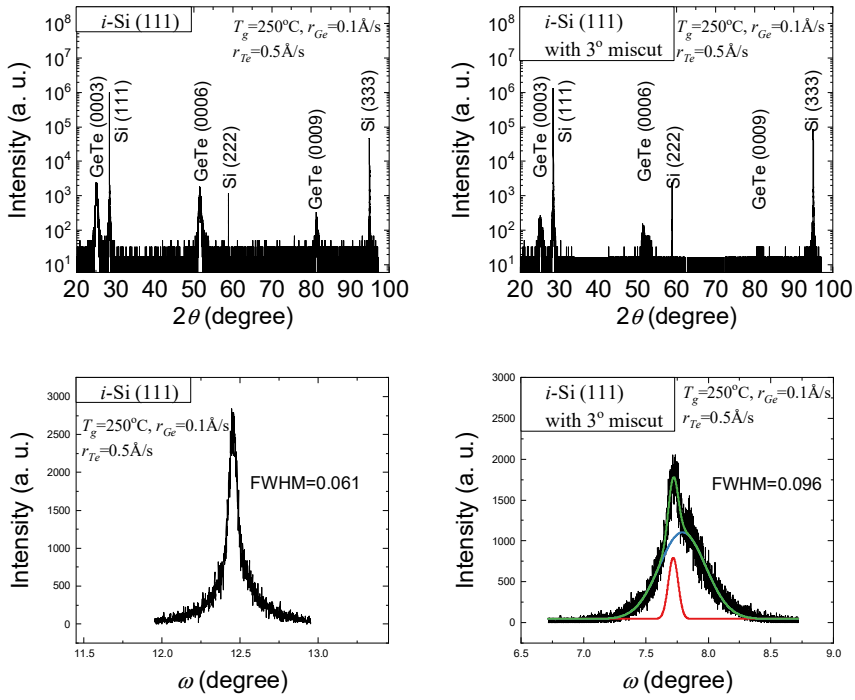

Figure 18. XRD theta-2theta- and ω- scans of GeTe films grown on Si (111) substrates with/without miscut.

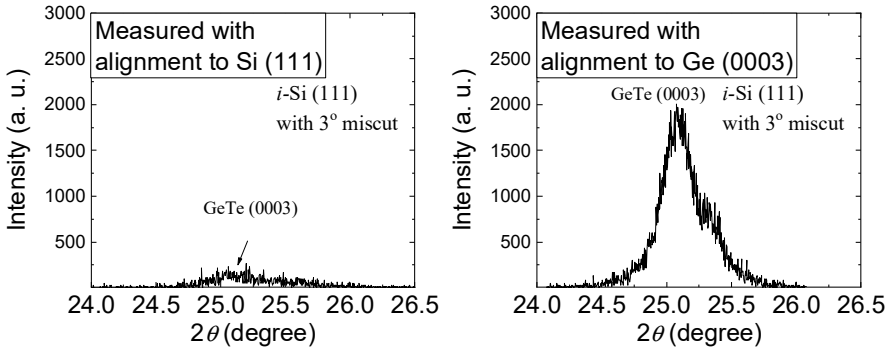

Figure 19. Magnified XRD theta-2theta scans of GeTe (0003) grown on miscut Si (111) according to the axis alignment (parallel to GeTe (000n) or Si (111)).

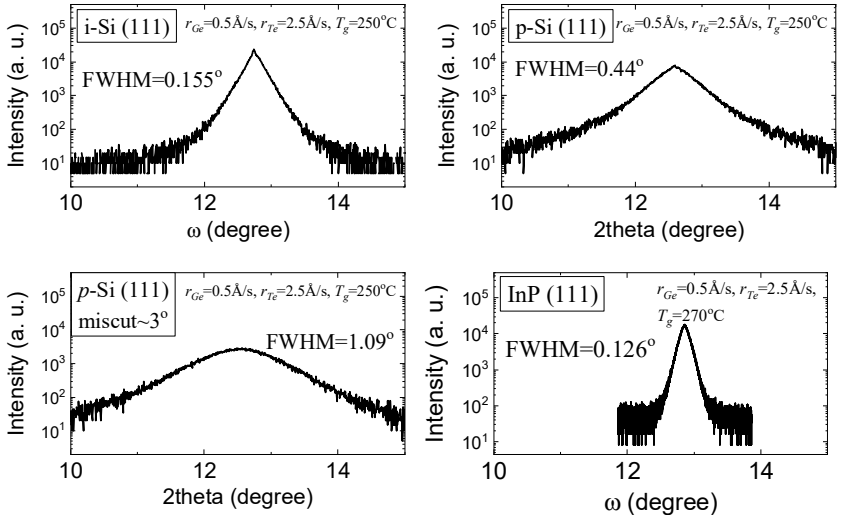

Figure 20. XRD ω scans (rocking curves) of grown GeTe films with various substrates.

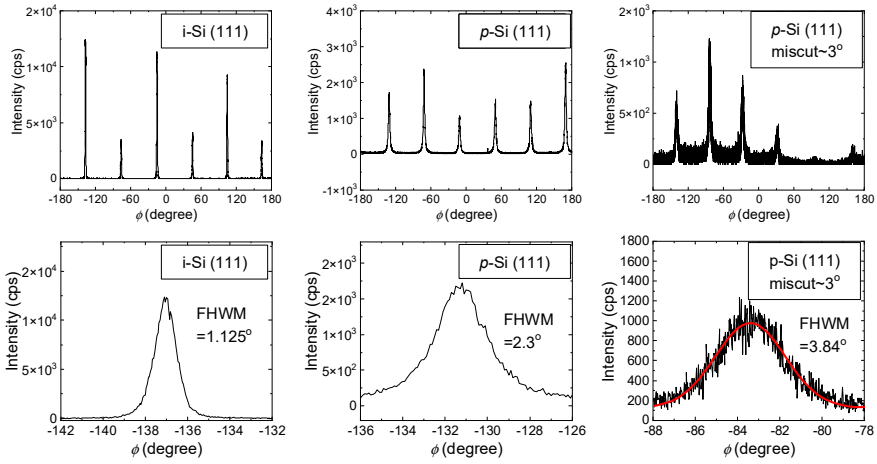

Figure 21. XRD phi-scan of GeTe grown on various substrates.

Basic transport properties

Figure 22 shows the carrier density and mobility of GeTe thin films grown on intrinsic Si (111), SiO_2, and Al_2O_3 (0001) substrates at room temperature. Carrier density and mobility were derived from Hall resistance measured under 5000 Oe magnetic field. Transport characteristics do not seem to have a large correlation with epitaxy quality. As a result of structural analysis, especially in i-Si (111), which was the best, carrier density is not low or mobility is not large. Instead, the GeTe thin film grown on the Al_2O_3 substrate, which had poor surface properties, such as the distribution of nanowires over the entire surface, showed the lowest carrier density and the highest

mobility. It can be seen that intrinsic Ge vacancy, the origin of high hole density, is almost independent of structural properties such as grain boundaries and nanowires. Due to the large lattice mismatch on the Al_2O_3 substrate, the fully relaxed GeTe film showed slightly greater mobility than the other two substrates.

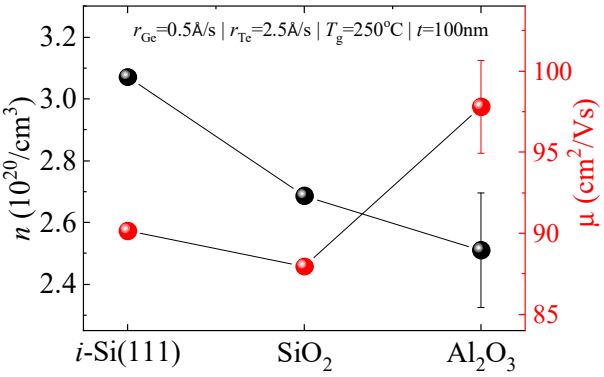

Figure 22. Carrier density and mobility of GeTe grown on various substrates at room temperature.

Comprehensive evaluation

Table 2 summarizes the characterization of 50 nm GeTe thin films grown on SiO_2, i-Si (111), p-type Si (111), miscut Si (111), Al_2O_3 (0001), and InP (111) substrates. Overall, the surface characteristics

of the intrinsic Si (111) and InP (111) substrates were excellent. The crystallinity analyzed through XRD, the intrinsic Si (111) substrate, and the InP (111) substrate were excellent. The transport properties of GeTe epi-thin films were almost independent of the substrate. In terms of thin film quality, the GeTe thin film grown on the InP substrate showed the best overall characteristics. On the other hand, it was determined that it would be advantageous to use Si substrates in a practical factor.

Considering both the practical factors of process compatibility and accessibility for the experiment, it was determined that the intrinsic Si (111) substrate would be the most suitable. Therefore, the GeTe epitaxy thin films used in the study to be introduced later were all grown on intrinsic Si (111) substrates.

Table 2. Summary of characteristics of grown GeTe thin films according to the substrates

		SiO_2	Intrinsic Si (111)	p-type Si (111)	Miscut Si (111)	Al_2O_3 (0001)	InP (111)
Surface Characteristics	Luster	bad	very good	not bad	very good	bad	very good
	Continuity	bad	good	good	good	bad	very good
	Flatness (RMS rough.)	bad	very good (3.1nm)	good (5.9nm)	not bad (6.9nm)	bad	very good (3.3nm)
	Nanowire	much	No	a little	No	much	No
XRD	Theta-2theta (Prep. Orient.)	No	Yes	Yes	Yes	Yes	Yes
	Rocking curve (FWHM)	-	0.155	0.44	1.09	-	0.126
	Phi-scan (FHWM)	-	6-folded (1.125)	6-folded (2.3)	6-folded (3.84)	-	-
Basic Transport	Carrier density [$10^{20}/cm^3$]	2.7	3.1	-	-	2.5	-
	Mobility [cm^2/Vs]	88	90	-	-	98	-
Practical Factors	Human Hazard	No	No	No	No	No	No
	Accessibility	Very good	Very good	Very good	good	Very good	not bad
	Electrical Resistivity	Insulating	Insulating	metallic	metallic	Insulating	Insulating
	Process Compatibility	Very good	Very good	Very good	not bad	bad	bad

2.3.2 Flux ratio

GeTe thin films were grown through co-evaporation of Ge and Te atomic sources. An Investigation was conducted to find the condition in which the 1:1 stoichiometry of GeTe and to find an appropriate Ge and Te flux ratio for the intended thin film quality. The respective Ge and Te fluxes were monitored through quartz crystal microbalance (QCM). Ge flux was fixed at 0.5 Å/s, and the thin film quality of the grown GeTe was compared to Te flux (1.3 Å/s, 1.5 Å/s, 2.0 Å/s, and 2.5 Å/s). The remaining conditions were the same with T_g=250 °C, intrinsic Si (111) substrate, and thickness= 100 nm.

First, the composition of GeTe thin films according to Te flux was investigated through wavelength-dispersive spectroscopy (WDS) (Figure 23). As the Te flux increases from 1.3 to 2.5 Å/s, it can be confirmed that the proportion of Ge and Te increases monotically (Figure 23). Considering that the thickness of the GeTe thin film is fixed at 100 nm, this tendency is estimated to be related to the density change of the grown GeTe thin film. As the Te flux increased, the density of the GeTe thin film seemed to increase. This is consistent with the surface analysis results, which will be discussed later. It was confirmed that the Te: Ge atomic ratio of the grown GeTe thin film was between 1.15 and 1.18, almost independent of the Te fluxes.

Although the GeTe phase with Ge:Te= 1: 1 ratio was clearly verified in the structural analysis results to be discussed below, measurement error, Ge vacancy, and Te segregation on the surface were the causes of up to ~20 % error in the WDS quantitative analysis. From the Te flux dependence of carrier density (Figure 30), the Te rich composition confirmed from the WDS results while excluding Ge vacancy as a cause, is presumed to be mainly due to measurement error and surface Te segregation. It was confirmed that GeTe that satisfies stoichiometry was grown even with a minimum of 2.6 times to a maximum of 5 times more Te. Since the vapor pressure of Te is much higher than that of Ge, excess Te that exceeds the stoichiometry diffuses out on the substrate (Figure 24).

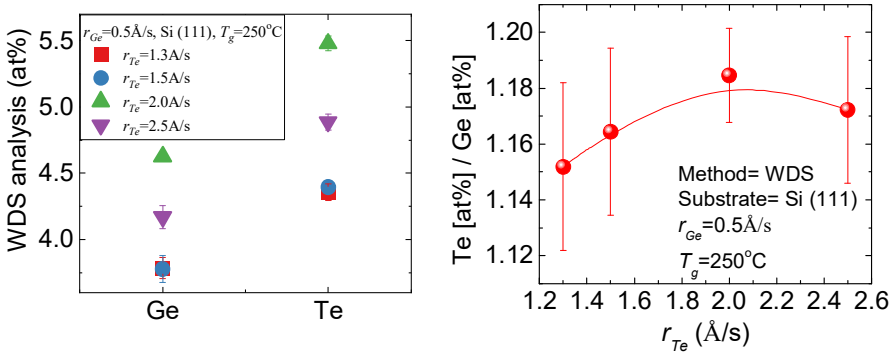

Figure 23. Quantitative analysis of the composition of GeTe thin films by WDS according to Te flux.

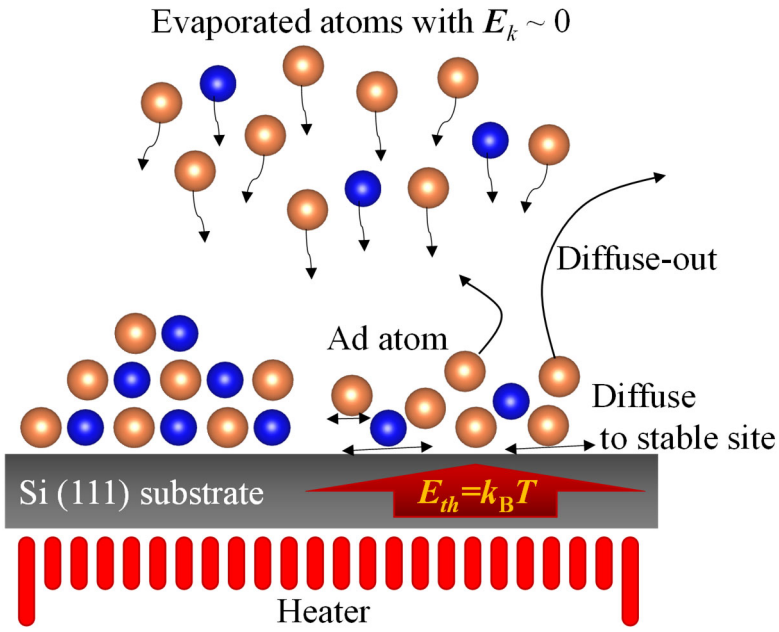

Figure 24. Schematic cartoon representing the growth mechanism of GeTe thin film.

Surface characteristics

Figure 25 and Figure 26 show AFM and SEM surface images of GeTe thin films grown according to Te flux. In addition, the SEM image observing the cross-section is shown in Figure 27. At r_{Te}= 1.3 Å/s, it was excluded from the AFM measurement because it was impossible to measure due to the large surface roughness. Many nanowires were confirmed the GeTe thin film of r_{Te}= 1.3Å/s which were also confirmed the GeTe films grown on poorly matched SiO_2

and Al_2O_3 (0001) substrates. The increase in the portions of Ge and Te according to the increase in r_{Te} seems to be related to the density increase (which is consisted with the WDS quantitative analysis (Figure 23)) that can be evidenced from the change in continuity.

In order to understand the relationship between the increase in Te flux and the increase in conformality of the grown GeTe thin films, let us consider the process from the initial attachment of ad atoms to the substrate and the growth of the thin film. As depicted in Figure 24, the ad atom absorbs thermal energy from the substrate after it is attached to the substrate. The absorbed thermal energy is converted into kinetic energy of the ad atom, and a part of the ad atom is diffused out and used to be removed, and some of the ad atom is used to form a stable crystal by diffusing the ad atom to the stable site. The frictional force acting between the ad atoms additionally consumes this kinetic energy. If the friction between the ad atoms is large, the local limited growth, that is, the growth of the island growth mode, occurs as it does not travel a sufficient diffusion distance and settles on the meta stable site. The relationship between the increase in Te flux and the friction force between ad atoms can be estimated by considering two things. The first is the atomic bond energy. The bond energies of Te-Te, Ge-Te, and Ge-Ge are 138, 149, and 157 kJ/mol, respectively, and the bond energy decreases when Te is involved.

The second is the concentration of Ge atoms among ad atoms. Most of the ad Te atoms are diffused out and re-evaporated before bonding. The remaining ad atoms rub and diffuse with the surrounding ad atoms, and as the Ge concentration increases, the density of the ad atoms causing friction increases.

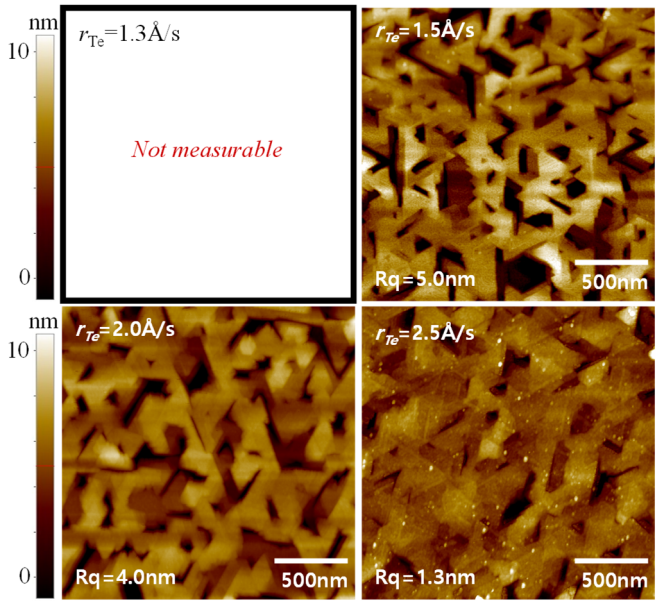

Figure 25. AFM topography of GeTe films grown under conditions of various Te fluxes.

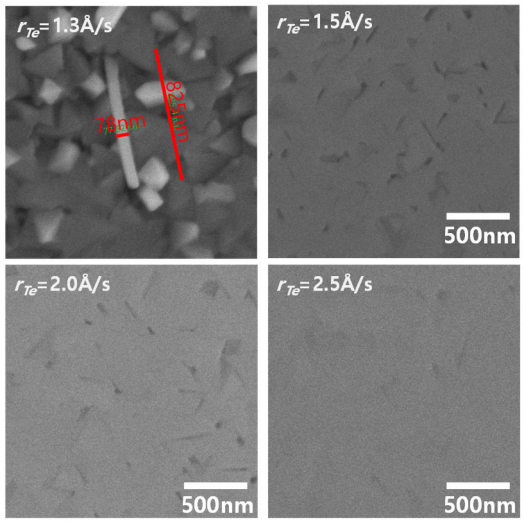

Figure 26. SEM surface inspection images of GeTe films grown under conditions of various Te fluxes.

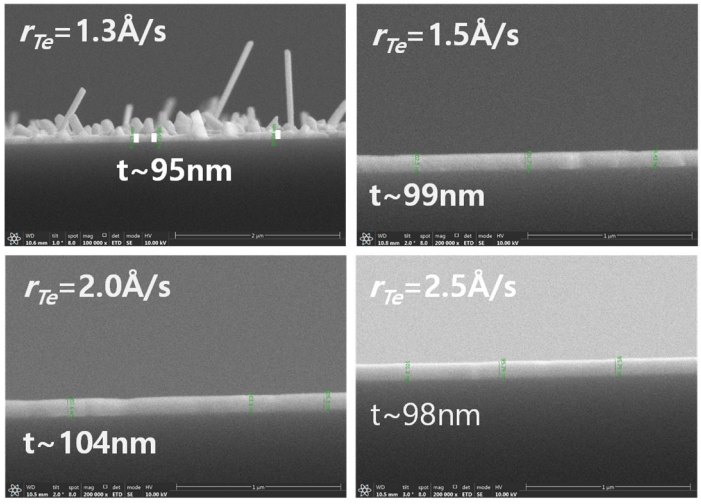

Figure 27. SEM cross-section inspection images of GeTe films

grown under conditions of various Te fluxes.

XRD analysis

Figure 28 shows the XRD theta-2theta and ω-rocking curves of GeTe thin films grown according to Te flux. The position of the reference XRD characteristic peak for the powder GeTe was indicated by a dotted line. The position of the reference peak for GeTe (0003) reflection is 2theta = 25.26°, which is slightly larger than the 25.028° observed in the thin film. These peak positions of the reference and the grown GeTe films can be converted to 3.55 and 3.52 Å, respectively. GeTe thin film has a more reduced c-axis lattice compared to the bulk GeTe crystal. The lattice mismatch between the Si and the GeTe is -8 % along the in-plane. The c-lattice reduction observed from XRD cannot be explained by the strain effect due to lattice mismatch with the substrate. Instead, one scenario that can explain this can be considered by considering the ferroelectric depolarization field. Since the thin film structure has the geometry that the depolarization field can be the largest, it can have a small ferroelectric polarization compared to the bulk. Since the ferroelectric polarization in GeTe results from asymmetric displacement in the (0001) direction, a decrease in polarization leads to a decrease in displacement leading to a decrease in the lattice constant. Except for the case of r_{Te} = 1.3 Å/s, where very rough

surface properties were confirmed, all clearly show the c-axis prepared orientation. It is difficult to ascertain a significant difference in the ω-rocking curve results between r_{Te}= 1.5 – 2.5 Å/s samples. Although there was a clear difference in surface properties as the Te flux changed, it was difficult to confirm the difference in crystallinity in the XRD results. Figure 29 shows the XRD phi-scan result of the GeTe thin film under the condition of r_{Te}= 2.5Å/s. Other peaks cannot be identified except for GeTe (104) reflections at 60° intervals indicating 6-folded symmetry. It can be seen that there is no other rotational domain in-plane except for the mirror twin domain.

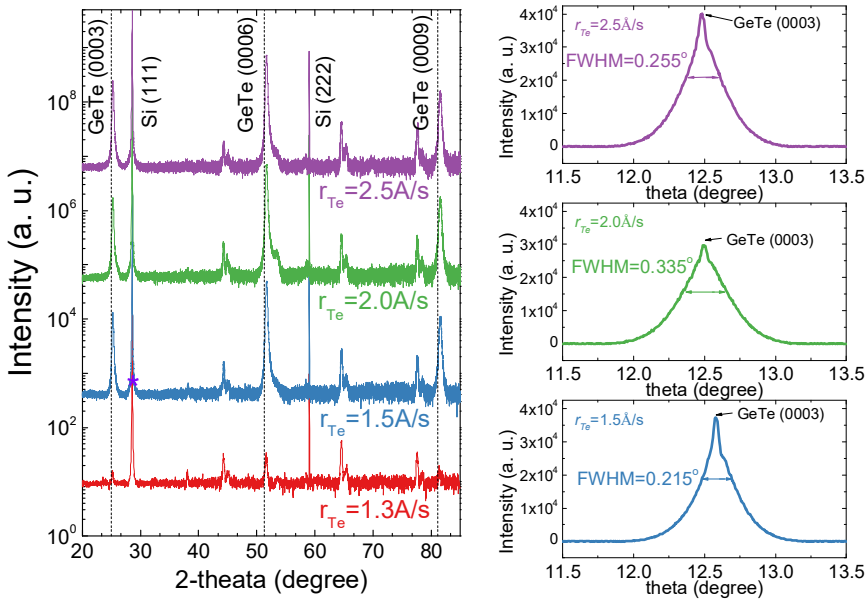

Figure 28. XRD theta-2theta and ω scans of GeTe films grown under conditions of various Te fluxes.

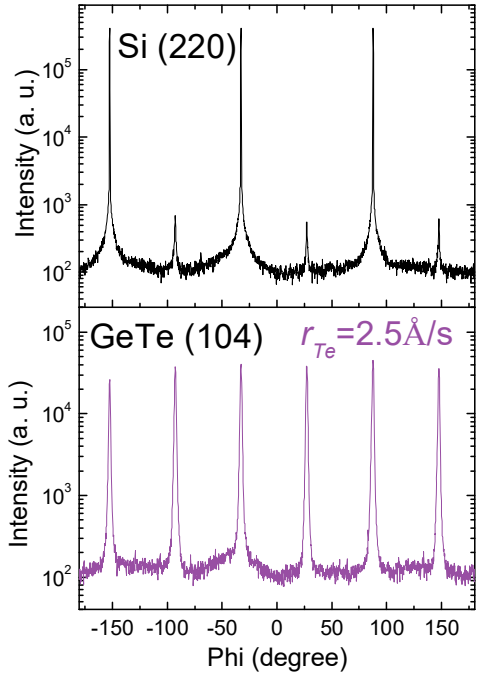

Figure 29. XRD phi scans of GeTe film and Si substrate.

Transport characteristics

Figure 30 shows the resistivity, carrier density, and mobility of GeTe thin film according to Te flux. As the Te flux increases, the resistivity and the carrier density decrease, while the mobility increases. As confirmed by surface characterization, the increase in Te flux aid to grow continuous GeTe thin film. The morphology of the GeTe thin film close to a single grain at r_{Te} = 2.5 Å/s is expected

to sufficiently suppress defect formation and scattering at the grain boundary.

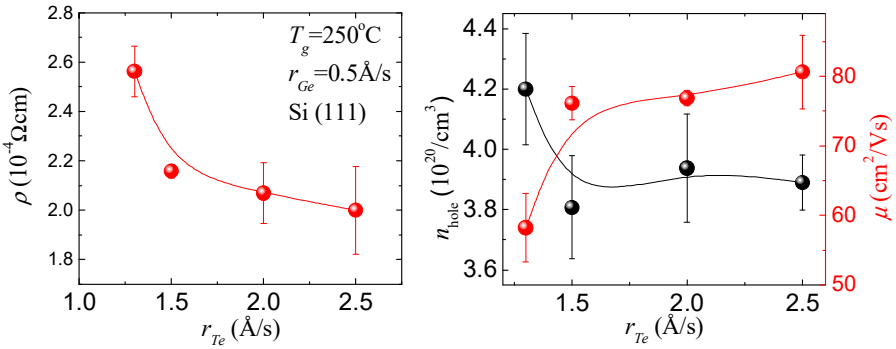

Figure 30. Transport properties of GeTe thin films grown under conditions of various Te fluxes.

Comprehensive evaluation

Table 3 summarizes the investigation for the Te/Ge flux ratio dependence on the characteristics of grown GeTe thin films. The Te/Ge flux ratio conspicuously affects the surface characteristics. As Te flux increased, the flatness and continuity of the grown thin film were improved. It might be due to the effect of reducing friction between ad atoms as Te flux increased. Except for the GeTe thin film under the condition of 1.3 Å/s, which is the smallest Te flux, no significant difference in XRD measurement was observed. It was confirmed that there is a relatively wide permissible window of Te/Ge

flux ratio for the growth of prepared oriented GeTe thin. In the transport properties, the mobility and the carrier density were limited by the grain boundaries. The condition of $r_{Te} / r_{Ge} = 5$, which had excellent surface characteristics and transport properties, was then applied to GeTe growth.

Table 3. Summary of investigation on GeTe growth with various Te/Ge ratio

r_{Ge}=0.5Å/s T_g=250°C Si (111)		r_{Te}=1.3Å/s	r_{Te}=1.5Å/s	r_{Te}=2.0Å/s	r_{Te}=2.5Å/s
XRD	Theta-2theta	c-axis aligned, low intensity	c-axis aligned	c-axis aligned	c-axis aligned
	Phi scan	-	-	-	3-folded with twin domains
Quantitative WDS (Te/Ge)		1.15	1.16	1.18	1.17
Surface morphology		random oriented crystal, nanowires	well oriented facet	well oriented facet	well oriented facet
Roughness (AFM)		bad	5nm	4nm	1.5nm
Carrier transport	n [10^{20}/cm^3]	4.2	3.8	3.9	3.9
	μ [cm^2/Vs]	58	76	77	80

2.3.3 Growth temperature

As mentioned in Section 2.3.2, the kinetic energy of ad atoms is obtained from the thermal energy of the substrate temperature. At low substrate temperature, good quality crystals cannot be grown because ad atoms move within limited diffusion distance. In addition, if the substrate temperature is too high, most of the ad atoms are re-evaporated, so that a thin film may not be formed or the growth rate may be very low. Therefore, with the aim of finding the optimal growth temperature, the characteristics of GeTe thin films grown under the conditions of growth temperature, T_g= 230, 250, and 270 ºC were investigated. For the remaining growth conditions of r_{Ge}=0.5 Å/s, r_{Te}=2.5 Å/s, Si (111) substrate, and, thickness=100nm were fixed.

Surface characteristics

Figure 31 shows AFM topography images of GeTe thin films grown at T_g= 250 and 270 ºC (excluding the data of T_g= 230 ºC, which could not be measured due to too poor surface roughness). Well-aligned triangular facets found in both GeTe thin films grown at growth temperatures of 250 and 270 ºC suggest that the growth orientation was well defined. It is noteworthy that the RMS roughness of the GeTe thin film at T_g= 270 ºC is 2.2 nm, which is slightly larger than that of the 1.7 nm GeTe thin film at T_g= 250 ºC.

This is a different result from the investigation of Te flux dependence, which confirmed that the surface continuity of the grown GeTe film increases as the adatom mobility increases. This can be properly explained by thermal equilibrium rather than by kinetics. A large strain occurring at the interface between GeTe/ Si (111) substrates with 8 % mismatch satisfies thermal equilibrium through lattice relaxing. It is expected that the relatively high growth temperature of 270 ºC would facilitate thermal equilibrium and promote strain relaxation. The full relaxation of the grown GeTe films at T_g = 270 ºC is expected to deteriorate the continuity of the thin film while forming a number of crators identified in the AFM topography of Figure 31.

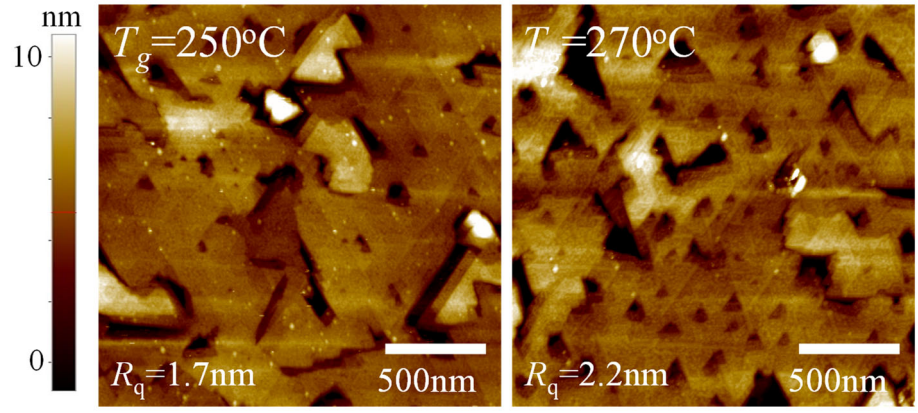

Figure 31. AFM topography of GeTe thin films with the growth temperature of 250 and 270 ºC

XRD analysis

Figure 32 and Figure 33 show the XRD theta-2theta and phi-scan, respectively. Regardless of the growth temperatures, XRD theta-2theta results only show GeTe (0001) and Si (111) reflections. It implies that the GeTe films has clear prepared orientation along the c-axis. The XRD intensity which is measured in identical experimental conditions can be used as indicator showing relative crystallinity. It was clearly confirmed that the intensity of GeTe (000n) increased with the increase of the growth temperature. In addition, the FWHM of the rocking curve was 0.324, 0.112, and 0.124° at T_g = 230, 250, and 270 °C, respectively. It shows that the GeTe thin film grown at the T_g = 250 °C has better mosaicity than at T_g = 270°C.. This proves once again that the lattice relaxation is promoted in the T_g = 270 °C sample. Figure 33 shows the XRD phi-scan results of T_g = 250 and 270 °C. Both thin films show 6-folded symmetry and no traces of rotational domains other than mirror twin domains are confirmed. However, in the phi-scan result at 270 °C, the difference in intensity between the major and twin peaks is conspicuous, suggesting that the twin domain is relatively suppressed compared to

the T_g = 250 ºC GeTe thin film.

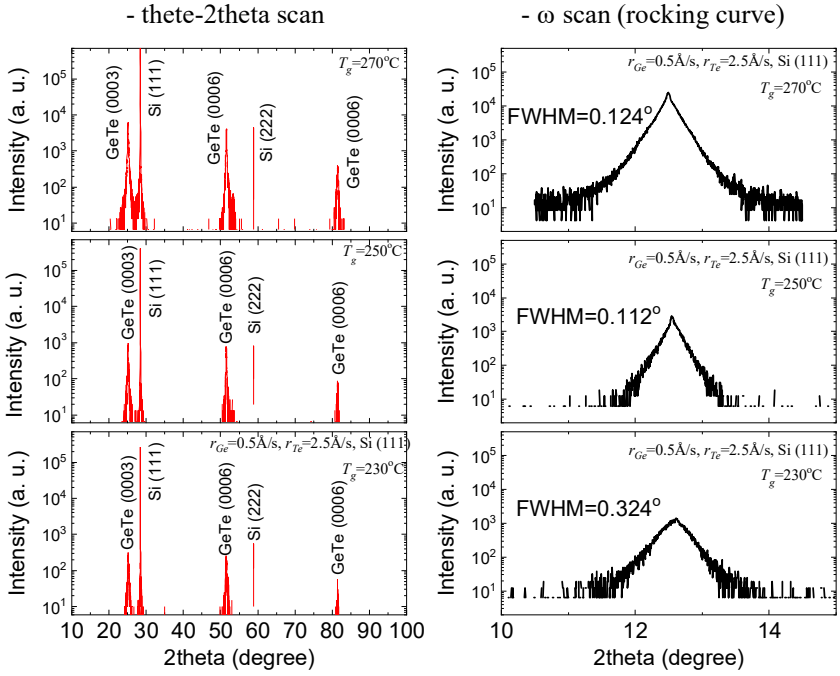

Figure 32. XRD theta-2theta- and ω-scan of GeTe thin films with the growth temperature of 230, 250 and 270 ºC.

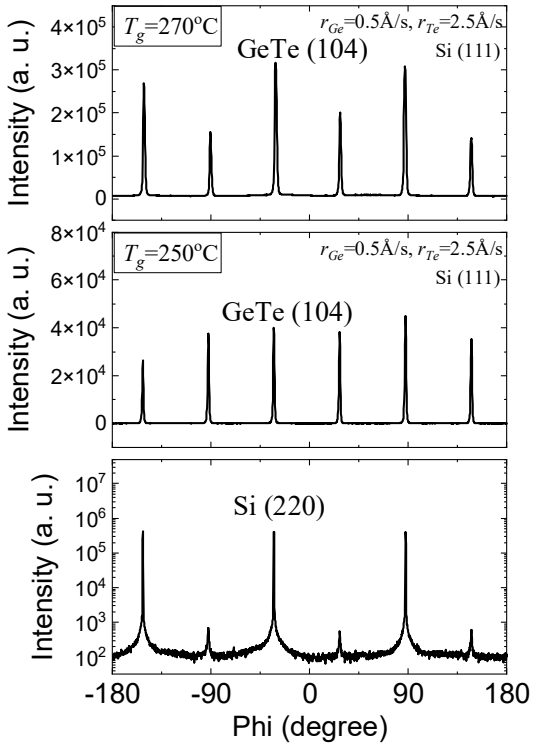

Figure 33. XRD phi-scan of GeTe thin films with the growth temperature of 250 and 270 °C.

Basic transport properties

Figure 34 shows the basic transport results of GeTe thin films as a function of growth temperature according to various Te fluxes. Red squares, blue circles, and green triangles indicate r_{Te} = 1.5, 2.0, and 2.5 Å/s (r_{Ge} = 0.5 Å/s), respectively. Carrier density (n) shows the dependence of being decreased and saturated as the T_g increases,

while as the Te flux increases, n decreases. Since both effects of the increment of Te flux and T_g improve the mobility of the ad atom, the carrier density reduction can be understood as the effect of the improvement of crystallinity. Mobility increased significantly as the T_g increased from 230 to 250 ºC, and did not change or decreased slightly as the T_g increased from 250 to 270 ºC. It seems to be an effect of deterioration of continuity confirmed by surface characterization. Resistivity increase with increasing growth temperature in all r_{Te}.

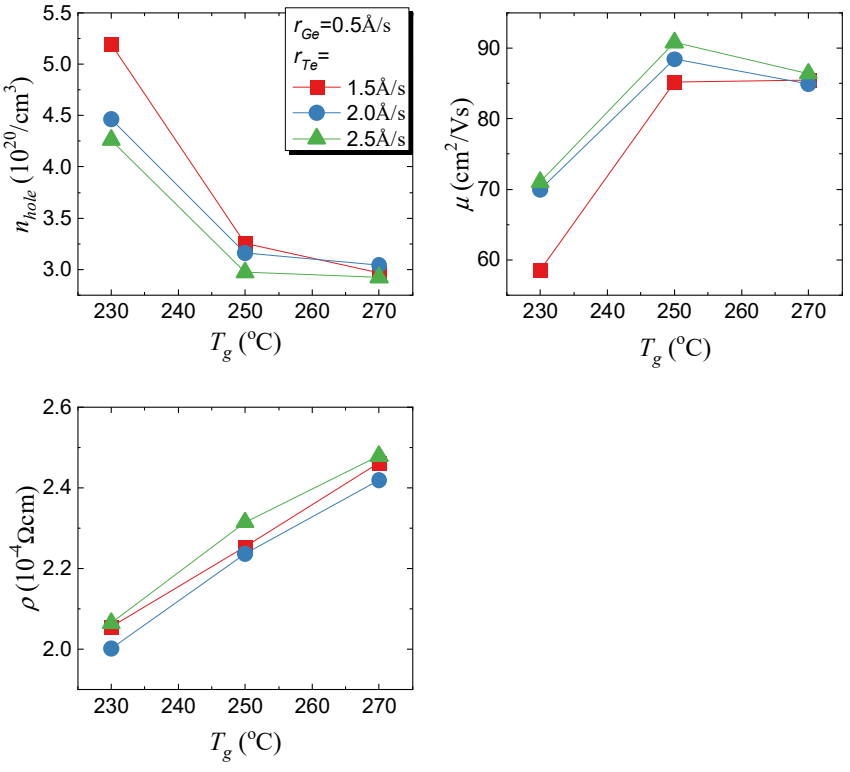

Figure 34. Basic transport properties of GeTe thin films with the growth temperature of 230, 250 and 270 ºC according to various Te fluxes.

Comprehensive evaluation

It was confirmed that the growth temperature of 250 ºC suitable for flat and continuous surface and 270 ºC for obtaining excellent crystal properties is the optimal condition for forming a GeTe thin film. Growth temperature motivate similar effect on the growth process with r_{Te} in that it improved the mobility of the ad atom, but it was different in that it promotes the relaxation of the epitaxy thin film.

Chapter 3.

Transport properties of α-GeTe thin film

3.1 Introduction

Recently, materials with strong spin-orbit coupling (SOC) have attracted much attention because they not only continuously unveil the unexplored phases of materials related to the exotic physics [53-57] but also provide routes to realize novel spintronic devices featuring ultralow power consumption [58-61] and topological quantum computing devices [62,63]. Several materials have been reported to have anomalously strong SOC compared to the conventional semiconductors and heavy metals and are being deployed for the development of the aforementioned devices [64-70]. In this regard, α-GeTe is fascinating because it possesses the ferroelectricity as well as strong SOC, implying the electrically tunable spin-momentum locking, a property very useful for the design of a lot of novel devices [67]. These kinds of materials are classified as the ferroelectric-Rashba semiconductor (FeRSC) [71,72]. GeTe is known to have the ferroelectric Curie temperature of ~670 K [73,74] and has been recently reported to remain ferroelectric down to the size of ~ 5 nm [75]. In addition, from a spin- and angle-resolved photoemission spectroscopy (SARPES) study,

GeTe was reported to have the record-high Rashba constant (α_R) of ~ 4.2×10^{-10} eVm [76].

Despite these promising properties in spintronic applications, however, the magnetic and magnetotransport properties of GeTe are not much explored, which is the main question to be addressed in this work. We have investigated the magnetoresistance (MR) of epitaxial GeTe thin films with varying thickness to find the evidence of the strong SOC that survives at temperature as high as 250 K. Furthermore, for the first time, we have found that GeTe becomes paramagnetic below ~20 K. We present the results showing that the interplay between the paramagnetism and the strong SOC in GeTe renders a variety of magnetotransport behaviors from negative magnetoresistance (MR) to strong SOC-dominated MR depending on the temperature and the thickness of GeTe.

3.2 Experimental method

Epitaxial α-GeTe thin films have been grown on Si (111) substrate by thermal evaporation of single elemental sources of Ge and Te. Just before loading into the growth chamber, the substrate was carefully prepared via three steps of cleaning: (1) in piranha solution (H_2O_2:H_2SO_4=1:3) for 10 minutes, (2) in SC-1 solution (NH_3:H_2O_2:H_2O=1:4:20) for 10 minutes, and (3) in diluted HF solution for a few minutes to remove the native oxide. After loading the substrate, the growth chamber was evacuated below 5×10^{-8} Torr and the substrate was quickly heated and held at 270 ºC for one hour. The flux of Ge and Te gas were separately controlled by using a thickness monitor and optimized with respect to the composition, crystallinity, and surface morphology. After such optimized flux of Ge and Te gas were stabilized, the growth started with the substrate temperature at 270 ºC and the thickness of GeTe was controlled by deposition time with the average deposition rate of 0.44 Å/s.

The structural characteristics of the grown GeTe films were investigated by using an X-ray diffractometer (XRD), an atomic-force microscope (AFM), and transmission electron microscope (TEM). The composition of GeTe films was analyzed by using Auger Electron Spectroscopy (AES). The ferroelectric and magnetic properties were examined by using a Piezo-Force Microscope (PFM) and a Vibrating Sample Magnetometer (VSM), respectively. And the

magnetotransport property of GeTe thin films were investigated by using a dc-current source (Model 2612A, Keithely Inc.), a nanovoltmeter (Model 2182A, Keithley Inc.), and a commercial cryogen-free cryostat (CMag-Vari.9, Cryomagnetics Inc.).

3.3 Result and discussion

3.3.1 Structural characterization

Figure 39 show the scanning electron microscope (SEM) image and the AFM image of the surface of a 50 nm-thick GeTe film, respectively, clearly indicating that the triangular crystalline grains are merged with lots of holes between those grains. Some holes are found to be as deep as ~ 10 nm, ~25 % of the film thickness, as shown in the line profile in right panel of Figure 39, which might be detrimental to the carrier transport in GeTe films. Nevertheless, the root-mean-square (rms) roughness is found to be ~1.3 nm implying the overall film surface is relatively flat as can be seen in right panel of Figure 39 on a film grain.

Figure 40 shows the X-ray diffraction (XRD) ω-2θ scan of a GeTe film, indicating that the film is oriented with its hexagonal (000h) axis normal to the substrate. In right panel of Figure 40, the full width at half maximum (FWHM) of the (0003) GeTe reflection is estimated to be ~0.075^{o} indicating that the crystalline quality of the film is good.

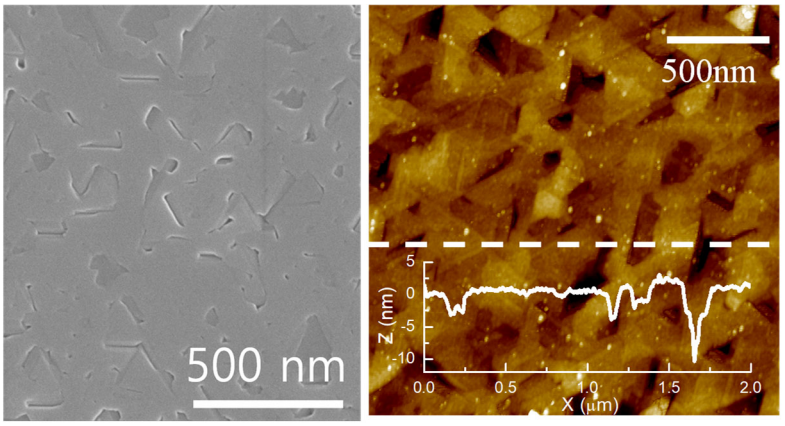

Figure 35. Surface properties of grown GeTe film with the thickness of 50nm.

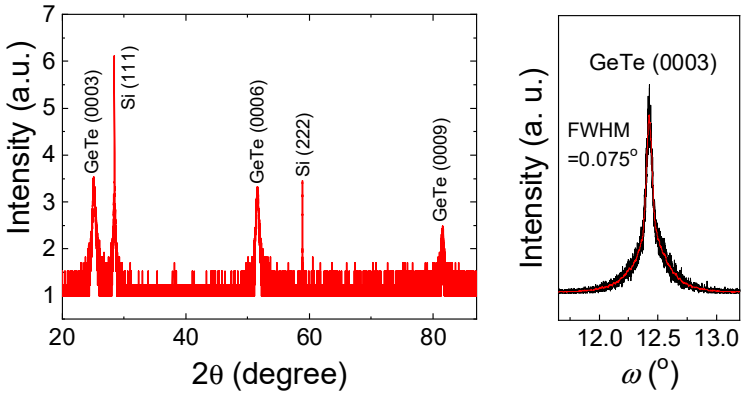

Figure 36. XRD theta-2theta scan of grown GeTe film with the thickness of 50 nm.

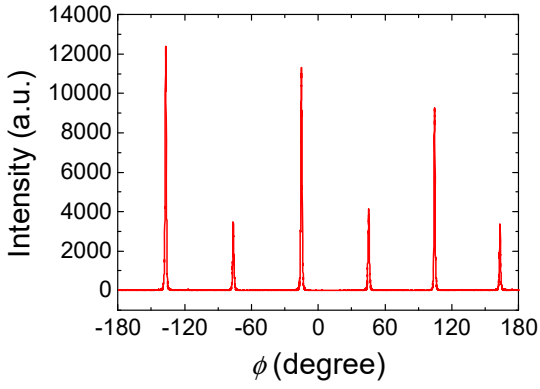

Figure 37. XRD phi-scan of grown GeTe film with the thickness of 50 nm.

And in Figure 41, the XRD ϕ-scan of the GeTe film shows that the GeTe film has three-fold rotational symmetry mixed with a small amount of twinned grains, consistent with the structure of α-GeTe. The XRD reciprocal lattice map of the GeTe film shown in Figure 42 indicates that the film is fully relaxed from the substrate or free of stress. This might be associated with the possible formation of a buffer layer between Si substrate and GeTe film, which will be shown in the later part. This is the reason why epitaxial GeTe film can be grown on Si substrate despite the large lattice mismatching (~8 %) between Si (111) and GeTe (0001) surface.

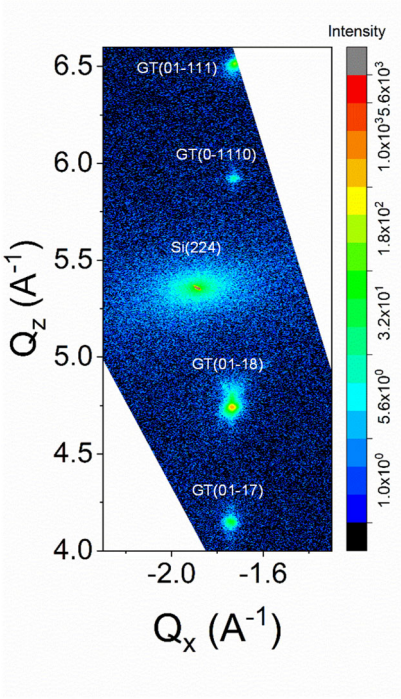

Figure 38. XRD reciprocal space map (RSM) of grown GeTe film with the thickness of 50 nm.

The atomic-resolution microstructure of the epitaxial GeTe film grown on Si (111) is presented in Figure 43(a). A buffer layer with a thickness of ~ 1 nm is found at the interface between Si substrate and GeTe film, consistent with the above result from the XRD reciprocal lattice map. Figure 43(b) shows a selected-area electron diffraction (SAED) pattern of a region in Figure 43(a) (Si+GeTe), which indicates that GeTe film is highly crystalline with *R*3m structure [77] mixed with a little amount of twin grains as indicated by a yellow

arrow in Figure 43(b). Figure 43(c) shows a Fast Fourier Transform (FFT)-filtered atomic-resolution image, which clearly shows Te (brighter balls) and Ge (dimmer balls). Note that Ge atoms are not positioned at the center between adjacent Te atoms, but rather shifted to the right. It implies the uncompensated polarization, consistent with the known ferroelectric nature of α-GeTe [75,78]. For a quantitative analysis, a line profile is also displayed along a red-dashed line in Figure 43(c), which is composed of two kinds of peaks. From the peak positions, the Te(left)-Ge(right) distance and Ge(left)-Te(right) distance are estimated to be 2.08 Å and 1.51 Å, respectively. These values are very close to the known values of 2.14 Å and 1.49 Å [79,80] as shown in Figure 43(d). The ferroelectric nature of GeTe films is also confirmed from a Piezoresponse Force Microscopy (PFM) study (Figure 44), where regions with different spontaneous polarization are distinguishably observed.

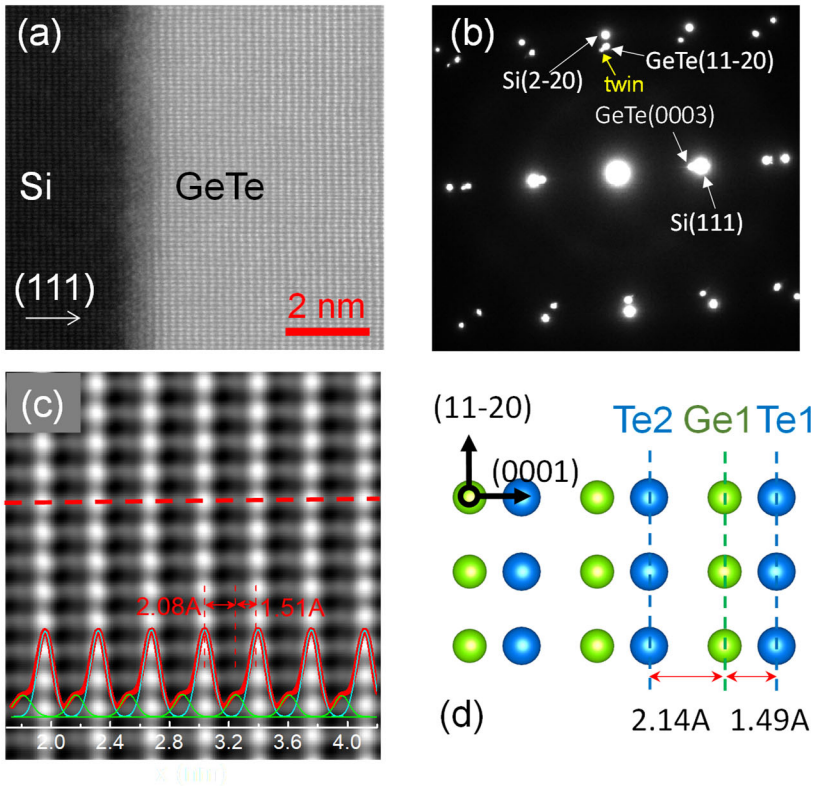

Figure 39. Scanning transmission electron microscopy (STEM) results of GeTe film. (a) STEM image of the GeTe/Si interface. (b) Fast Fourier transformation (FFT) of (a). (c) Inverse FFT filtered STEM images of GeTe films. (d) GeTe crystal model representing the non-centrosymmetry.

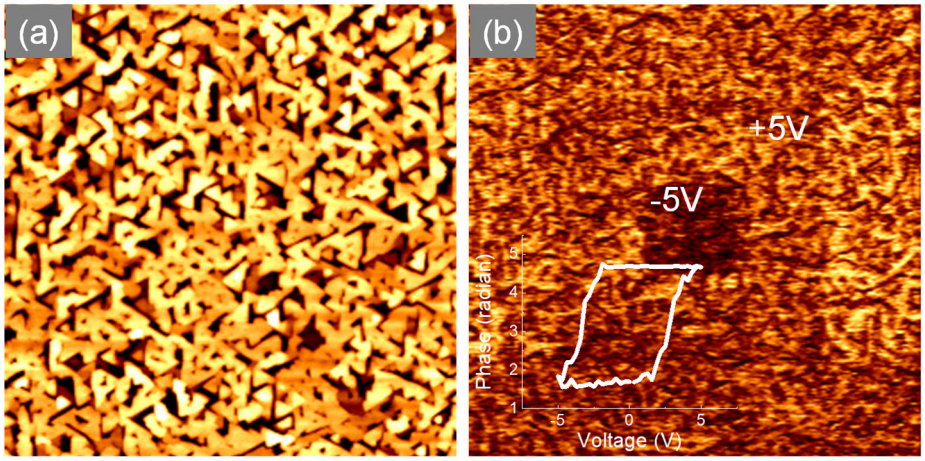

Figure 40. Piezo-force microscopy of GeTe film. (a) AFM topography. (b) PFM phase of GeTe film, the phase hysteresis loop is contained as inset.

3.3.2 Magneto-transport properties

We now present evidence of the strong spin-orbit coupling (SOC) in our GeTe thin films as a FeRSC. To characterize SOC in GeTe films, magneto-transport property is investigated because the strong SOC is known to manifest itself as a sharp dip structure around H=0 in the magnetoresistance (MR) vs. H curve due to the effect of the weak antilocalization (WAL) [81-84], where H is the external magnetic field applied perpendicular to the film plane. Figure 45 shows MR vs. H curve of a 50 nm-thick GeTe film at various temperatures. The overall feature seems to follow the Kohler's rule (MR~kH^2, where k is a constant) [85] with a curvature depending on

temperature (T), consistent with the feature of the ordinary MR (OMR) induced by the Lorentz force. However, a magnification of the low field region (inset in Figure 45) reveals a few intriguing features. First, note that a sharp dip structure around H=0 is observed, evidence of the WAL, and that it gets more salient as T increases up to 100 K. Such a temperature dependence is intriguing in that the WAL is a quantum interference phenomenon, vulnerable to thermal fluctuations. Indeed, in most of the materials with strong SOC, for example, topological insulators and a few oxide materials [86-91], the effect of the WAL has been observed to decay as T increases. The second intriguing feature is found in the complex H-dependence of MR at 1.8 K, which appears convex upward in -0.7 T < H < 0.7 T in contrast to the convex-downward shape in $|H|$ > 0.7 T. As a result, MR at 1.8 K has negative values in -0.8 T < H < 0.8 T.

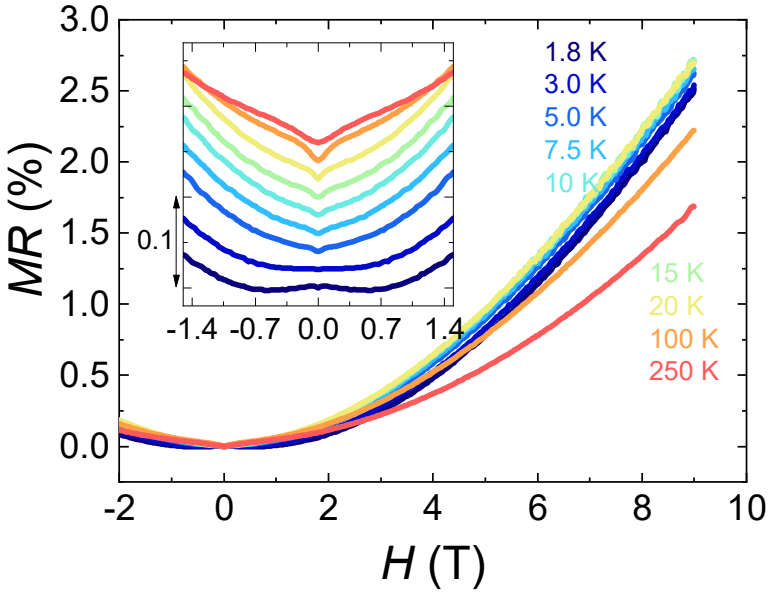

Figure 41. Magneto-resistance (*MR*) as a function of magnetic field (*H*) of 50 nm GeTe thin film at various temperature.

To get some clues about these intriguing phenomena, the same characterization has been performed for GeTe films with various thicknesses ranging from 5 nm to 100 nm. As can be seen in Figure 46 and Figure 47, the MR vs. *H* curves show a few intriguing systematic changes with the thickness of GeTe film (t_{GeTe}). First, at low temperature, the tendency to the negative MR is enhanced as t_{GeTe} decreases. It is shown by the increase in the value of *H* (H_{min}) at the minimum MR, indicated by the red triangle in Figure 47, to the higher field as t_{GeTe} decreases. As a result, the MR(*H*) curve does not show

an upturn up to 9 T for a 5 nm-thick sample at 1.8 K. Second, at elevated temperature, the dip structure around H=0 is enhanced as t_{GeTe} increases, clearly showing the effect of the WAL up to 250 K for a 100 nm-thick GeTe film (Figure 47).

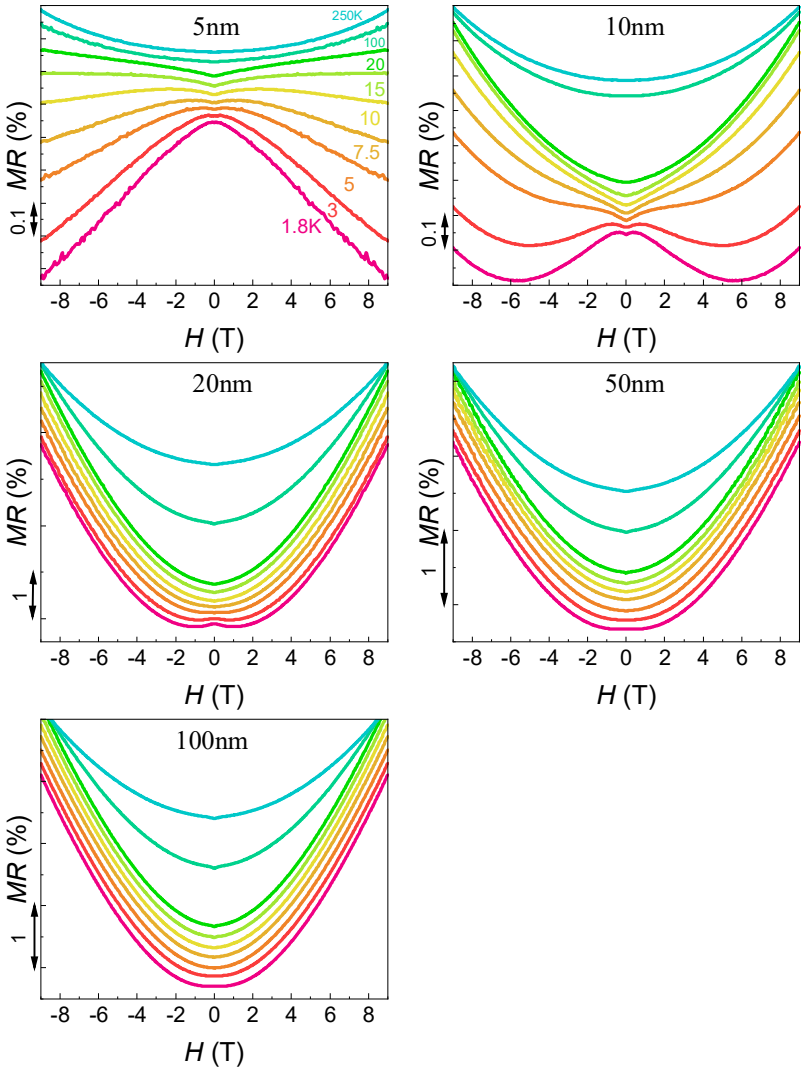

Figure 42. *MR* as a function of *H* of 5, 10, 20, 50, and 100 nm GeTe thin film at various temperature in range of -9 T < *H* < +9 T.

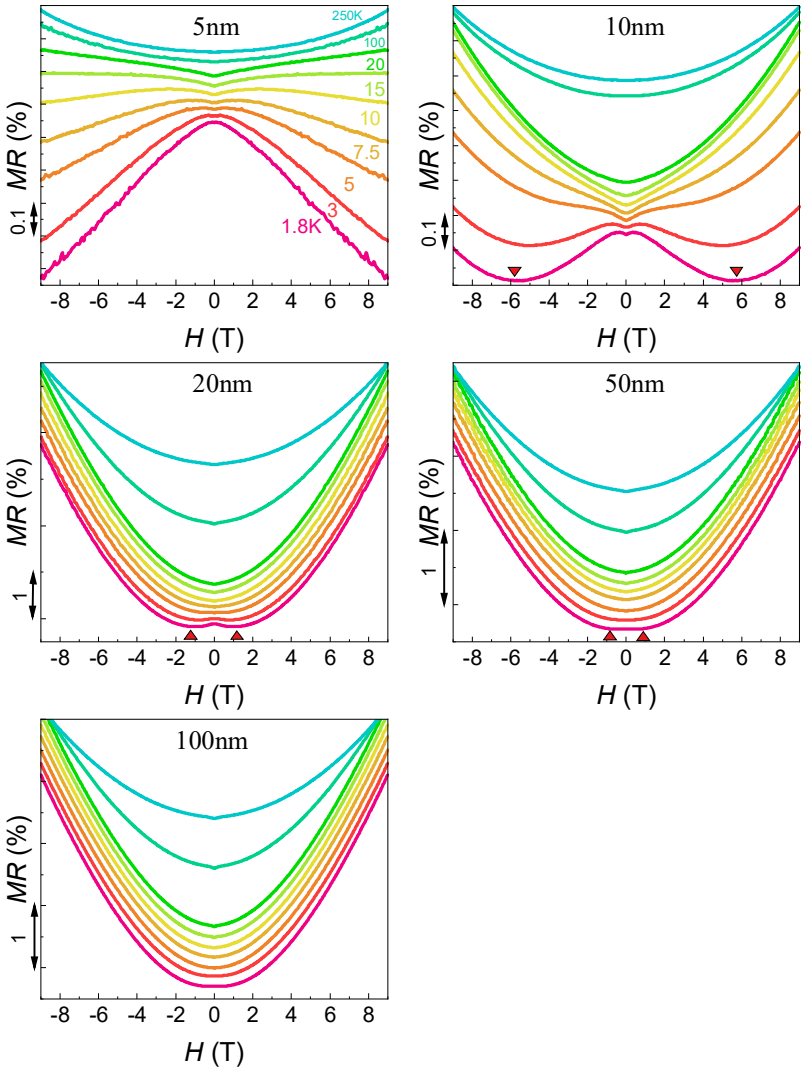

Figure 43. *MR* as a function of *H* of 5, 10, 20, 50, and 100 nm GeTe thin film at various temperature in range of -2 T < *H* < +2 T.

To clarify the origin of the negative MR, we have examined the

magnetic property of GeTe films to find that GeTe films show paramagnetism at low temperature (Figure 47).

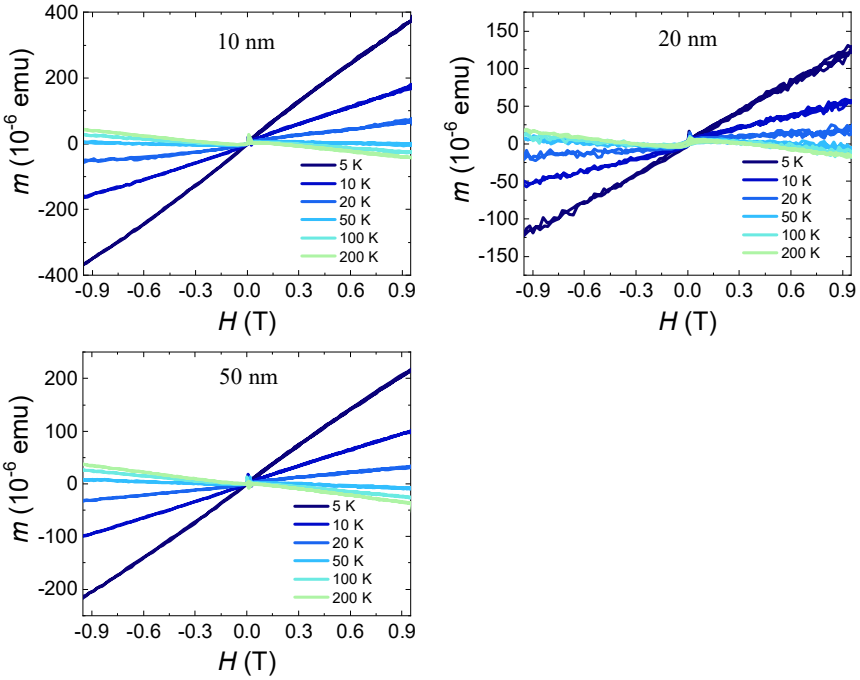

Figure 44. Magnetic moment (*m*) as a function of magnetic field (*H*) of 10, 20, and 50 nm GeTe films at the temperature range of 5 - 200 K.

To the best of our knowledge, the magnetic property of GeTe is unknown and the paramagnetism in GeTe is first observed in this work. The anisotropic *MR* is described by $MR_{AMR} \sim C(M/M_S)^2$ for paramagnetic or ferromagnetic materials [92-94], where *C*, *M*, and M_S are a material-specific negative constant, the magnetization, and

the saturation magnetization, respectively. Therefore, the negative MR shown in Figure 46 and Figure 47 is naturally associated with the paramagnetic property of GeTe. In addition, considering that the demagnetization factor is proportional to $1/t_{GeTe}$ when H is applied perpendicular to the film plane (the situation of the MR measurement), the dependence of H_{min} on t_{GeTe} shown in Figure 46 and Figure 47 is naturally explained. Therefore, the complex behavior of MR(H) curve of GeTe films is attributed to the interplay of three contributions: (1) OMR, (2) AMR, and (3) WAL.

Based on these findings, we have performed a quantitative analysis on the MR(H) curves in order to characterize the SOC in GeTe. It is known that the carrier transport in GeTe is of three-dimensional (3D) character with the Fermi energy (E_F) residing inside the valence band due to defects like Ge vacancies [95,96]. In addition, from the dependence of MR(H) curve on the angle between H and the film plane (Figure 49), we confirmed the 3D character of the transport.

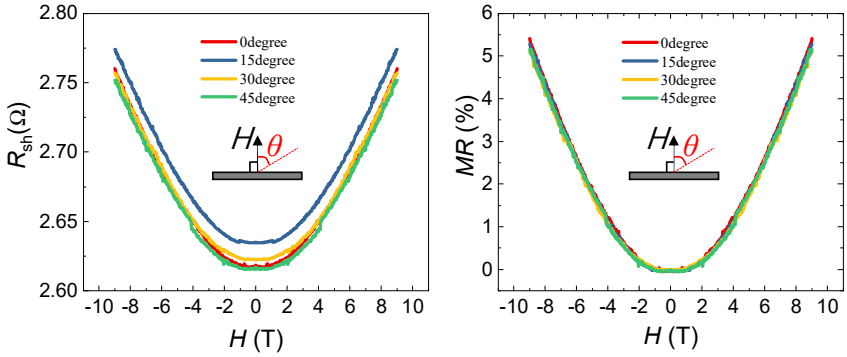

Figure 45. Angle dependence of *MR*(*H*) of GeTe 50 nm film at *T*=1.8 K.

The quantum correction to MR by WAL in 3D is described by Fukuyama-Hoshino (F-H) model [83,84,97] expressed by the following equations (1) and (2).

$$\frac{\Delta\rho_{WAL}(B)}{\rho(0)^2} = \frac{e^2}{2\pi^2 h}\sqrt{\frac{2\pi eB}{h}}\left[\frac{1}{2}f_3\left(\frac{B}{B_\varphi}\right) - \frac{3}{2}f_3\left(\frac{B}{B_2}\right)\right] \quad \ldots (1)$$

$$f_3(y) = \sum_{n=0}^{\infty}\left[2\left(n+1+\frac{1}{y}\right)^{\frac{1}{2}} - 2\left(n+\frac{1}{y}\right)^{\frac{1}{2}} - \left(n+\frac{1}{2}+\frac{1}{y}\right)^{-\frac{1}{2}}\right] \quad \ldots (2)$$

In Eq. (1), *e* and *h* are the charge of an electron and Planck's constant, respectively. And, $B_\varphi = B_i + 2B_S$ and $B_2 = B_i + \frac{2}{3}B_S + \frac{4}{3}B_{SO}$, where B_x (*x*=*i*, *S*, and *SO*) represents the characteristic magnetic field strength for the inelastic, spin-flip, and spin-orbit scattering, respectively.

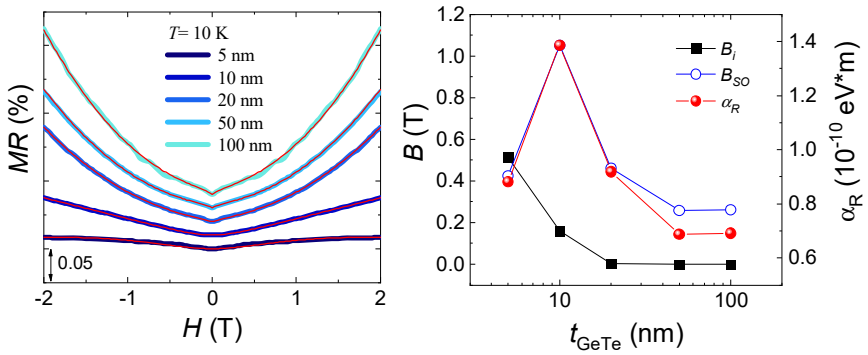

Figure 46. *MR*(*H*) fitting with FH model. (left panel) *MR*(*H*) and the fitted curves (red lines). (right panel) The extracted fitting parameters (B_i and B_{so}) and the calculated Rashba constant, α_R as the function of the GeTe thickness.

In Figure 50, MR(*H*) curves at 10 K for GeTe films with varying thickness are replotted along with their respective fitting curves (red lines) given by the following equation (Eq. (3)) [86,98,99].

$$\boldsymbol{MR(B) = C'\sqrt{B}\left[\frac{1}{2}f_3\left(\frac{B}{B_\varphi}\right) - \frac{3}{2}f_3\left(\frac{B}{B_2}\right)\right] + C\left(\frac{M(B)}{M_S}\right)^2 + kB^2}$$

…(3)

In Eq. (3), *C'*, B_ϕ, B_2, *C*, and *k* are constants depending on the material and each term represents the contribution from WAL, PMR, and OMR in order, where the last is assumed to follow the Kohler's rule with *k* being a positive constant [85]. It is shown in Figure 50 that

MR(H) curves of all the investigated GeTe films are well described by Eq. (3) supporting the suggested model. Assuming B_S=0 due to the absence of magnetic impurity in GeTe films, B_i and B_{SO} have been estimated from the fitting and presented as a function of t_{GeTe} in right panel of Figure 50. As t_{GeTe} increases, it is found that B_i decreases and saturate to nearly zero above t_{GeTe}=20 nm, which is naturally explained by the reduction of the surface to volume ratio because the surface and the interface act as sources of inelastic scattering.

Figure 50 also shows the Rashba constant (α_R) of GeTe thin films, which is obtained from the relation $B_{SO} = \frac{\alpha_R^2 m^{*2}}{e\hbar^3}$ assuming the D'Yakonov-Perel (D-P) mechanism as the dominant spin relaxation mechanism [83,98]. Here, m^* (~0.022 m_e) [67,100] and $\hbar$ are the effective mass of electron in GeTe and the reduced Planck's constant (=$h/2\pi$), respectively. In our knowledge, this is the first time to characterize α_R of GeTe thin films by the magnetrotransport measurement, which provides direct information for the application of GeTe in electronic and spintronic devices. The obtained α_R (=(0.8~1.4) $\times 10^{-10}$ eV·m) is smaller than 4.2×10^{-10} eV·m obtained from a spin- and angle-resolved photoemission (SARPES) study of GeTe thin films [76], which is thought to be due to the difference in the measured quantities (band structure for the SARPES vs. electrical resistivity for the magneto-transport) and the imperfections in

procedures for obtaining the value of α_R, for example, the assumption of the spin relaxation by D-P mechanism. Nevertheless, the obtained α_R of GeTe films is still high enough to raise the possibility of utilizing the effect of strong SOC in devices at elevated temperature, evidenced by the signature of WAL at 250 K shown in Figure 46 for thick ($t_{GeTe} \geq 50$ nm) GeTe films.

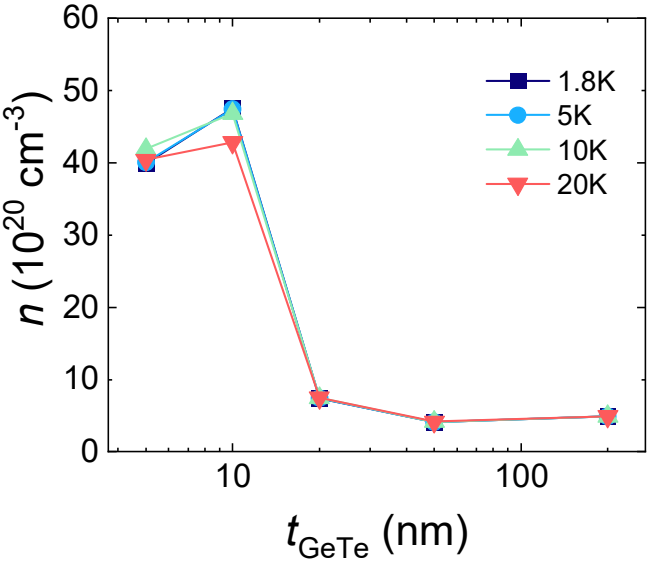

Figure 47. The carrier density of GeTe as the function of thickness.

It is worth to note that α_R (or B_{SO}) of GeTe thin films shows a non-monotonic dependence on t_{GeTe} with its maximum at t_{GeTe}=10 nm. Interestingly, we have found that the carrier density (n) of GeTe thin films shows a similar t_{GeTe}-dependence (Figure 51) implying a close

relation between n and α_R. It can be attributed to the change in depolarization field with the change in n depending on t_{GeTe}. In detail, the larger free carrier density leads to the stronger internal screening of polarization in the thinner GeTe films, reducing depolarization effects. This effect results in the increase in the electrical polarization concomitant with the increase in α_R. This explanation is supported from a previous study using an atomic pair distribution (PDF) study, which reported the stronger stabilization of the linearly ordered polar state in GeTe with larger n compared to the more insulating $BaTiO_3$ [75]. In addition, in the thin film limit in this work (t_{GeTe}=5 nm), the large decrease in α_R is associated with the change in the direction of the polarization. In a previous scanning tunneling microscope (STM) study on SnTe thin films [101] which has a structure similar to GeTe, it was shown that the ferroelectric polarization turns in-plane for atomically thin films. Similarly, we conjecture that the ferroelectric polarization of a 5 nm-thick GeTe film is significantly canted from the out-of-plane direction, resulting in the significant reduction in α_R.

3.4 Conclusion

In summary, we have investigated the magneto-transport property of epitaxial GeTe thin films, which is known to possess simultaneously ferroelectricity and strong SOC. Ferroelectricity in our GeTe films are manifested by the broken centrosymmetry and the switching of the polarization observed by HRTEM and PFM, respectively. And strong SOC in our GeTe films are characterized by the effect of WAL on MR from the magnetotransport measurements. Furthermore, we have found that GeTe becomes paramagnetic below 20 K, leading to a complex behavior of the MR(H) curve of GeTe thin films. Nonetheless, the effect of WAL is observed to survive at elevated temperature up to 250 K. This apparently indicates that GeTe is a promising material for the application in spintronic devices operating at room temperature, whose operation principle is based on (inverse) spin-Hall effect (ISHE and SHE) and spin-orbit torque (SOT).

Chapter 4.

Spin-orbit torque (SOT) in α-GeTe/BiFe bilayer

4.1 Introduction

Rashba spin-orbit coupling (RSOC) is a crucial element for spin-based information devices. Control of spin precession concomitant with the modulation of RSOC by electric field has been theoretically suggested and experimentally demonstrated using a two-dimensional quantum well [25,102-106]. In addition to the gate-controlled spin precession, the RSOC also contributes to spin-orbit torques (SOTs) in a normal metal (NM)/ferromagnet (FM) bilayer, the basic structure for SOT-active devices, where the inversion symmetry breaking at the NM/FM interface gives rise to a RSOC [25,107-111]. As the SOT serves as a writing scheme for energy-efficient spintronic devices [112-114], enhancing the RSOC effect in NM/FM bilayers is an important task for practical applications.

Most studies of the RSOC have focused on interfacial effects in two-dimensional systems or bilayers. Considering spin transport, it is expected that the RSOC effect becomes stronger when the RSOC is present in a bulk of the system, not limited to an interface. Recent

studies have revealed that several polar crystals such as BiTeCl [115], BiTeI [26], and GeTe [7] have strong bulk RSOC, where the bulk inversion asymmetry is related to the ferroelectricity. These materials are classified as the ferroelectric-Rashba semiconductors [8,116]. Among these materials, α-GeTe is remarkable in that it has the relatively high ferroelectric Curie temperature of ~670 K [117] and its ferroelectricity survives at the thickness of ~5 nm [118]. In addition, a spin- and angle-resolved photoemission spectroscopy (SARPES) study reported that GeTe has a large Rashba constant of $\sim 4.2\times10^{-10}$ eV·m [12].

The SOT strength in NM/FM bilayers is related to the spin Hall conductivity of spin-orbit channel, NM layer. The aforementioned attractive features of GeTe has led to recent density functional theory calculations of the spin Hall conductivity of GeTe and its controllability through the modulation of electric polarization [119,120]. Even considering various values of electric polarizations, however, these theoretical studies predicted that the spin Hall effect (or spin Hall angle) of bulk Rashba GeTe at the Fermi level is not superior to that of Pt, a widely used spin-orbit channel for SOT devices. This result was attributed to the fact that the SOC effect of GeTe was mainly observed in the valence bands (Te 5p-orbitals) below the Fermi level, due to Ge vacancies.

Despite the above prediction, it is worthwhile to experimentally investigate the SOT in GeTe/FM bilayers because those theories [119,120] considered only bulk GeTe. In GeTe/FM bilayers, there is an additional inversion asymmetry at the GeTe/FM interface. Recent studies for NM/FM bilayers with centrosymmetric NM materials suggested that the NM/FM interface can substantially contribute to the SOT [109-111]. In this respect, an important question has remained unexplored: what happens to the SOT of NM/FM bilayers where the NM layer is a bulk Rashba material. In this work, we address this question by investigating the SOTs in GeTe/$Ni_{81}Fe_{19}$ bilayers using the second harmonic Hall voltage measurement [121], from which we extract the magnitudes of SOTs.

4.2 Experimental method

4.2.1 Material growth and characterization

α-GeTe thin films have been grown on Si (111) substrate by thermal evaporation of single elemental sources of Ge and Te. Just before loading into the growth chamber, the substrate was carefully prepared via three steps of cleaning: (1) in piranha solution (H_2O_2:H_2SO_4 = 1:3) for 10 minutes, (2) in SC-1 solution (NH_3:H_2O_2:H_2O = 1:4:20) for 10 minutes, and (3) in diluted HF solution for a few minutes to remove the native oxide. After loading the substrate, the growth chamber was evacuated below 5×10^{-8} Torr and the substrate was quickly heated and held at 270 ºC for one hour. The flux of Ge and Te gas were separately controlled by using a thickness monitor and optimized with respect to the composition, crystallinity, and surface morphology. After such optimized flux of Ge and Te gas were stabilized, the growth started with the substrate temperature at 270 ºC and the thickness of GeTe was controlled by deposition time with the average deposition rate of 0.44 $Å s^{-1}$. The structural characteristics of the grown GeTe films were investigated by using an X-ray diffractometer (ATX-G, Rigaku), an atomic-force microscope (AFM, XE-70, Park systems), and transmission electron microscope (TEM, TitanTM 80-300, FEI). The composition of GeTe films was analyzed by using Auger Electron Spectroscopy (AES,

PHI-700, ULVAC-PHI).

4.2.2 Device fabrication

The device consists of GeTe/Ni81Fe19/MgO/Ta multilayer, where MgO (2 nm)/Ta (2 nm) layer is deposited for protecting the ferromagnet layer. After the grown GeTe films were performed an ion-milling process, the ferromagnetic layer and the capping layers were deposited by the DC magnetron sputtering without a vacuum breaking (see Supplementary Fig. S10 for FM characteristic). The transport channels were patterned by photolithography and Ar ion milling. Then, contact electrodes made of Ti (5 nm)/Au (100 nm) were formed by photolithography and lift-off. The lateral dimension of the channel was 100 μm × 6 μm.

4.2.2 Harmonic Measurement

All measurements were performed in a physical property measurement system (PPMS) at room temperature. The Hall voltage was measured with supplying the AC current from the Keithley 6221 and simultaneously monitoring the first and second harmonic Hall voltages by SR850 and SR860 lock-in amplifier, respectively. All harmonic transport measurements are performed at room temperature with an alternating current with a frequency of 17 Hz.

4.3 Result and Discussion

4.3.1 Harmonic Hall measurements

An in-plane charge current flowing through a SOC channel induces a perpendicular spin current, which exerts a SOT on the nearby ferromagnet. In this experiment, we extract the magnitude of SOT in a GeTe(130 nm)/NiFe(20 nm) structure via harmonic Hall measurements (see Methods). We investigate a field-like torque ($\mathbf{T}_{FL} \propto \mathbf{m} \times \mathbf{y}$) and a damping-like torque [$\mathbf{T}_{DL} \propto \mathbf{m} \times (\mathbf{y} \times \mathbf{m})$], where $\mathbf{m}$ and $\mathbf{y}$ are unit vectors along the magnetization and perpendicular to both directions of charge-current flow (x) and spin-current flow (z), respectively. For an in-plane magnetization, the field-like and damping-like torques correspond to the in-plane (B_{FL}) and out-of-plane (B_{DL}) effective spin-orbit fields, respectively, as shown in Figure 52. We note that according to our coordinate system and geometry, a current-induced Oersted field is in the $-y$ direction for a positive current [see Figure 52]. The sign of the current-induced Oersted field is also confirmed by a harmonic Hall measurement for a Cu/NiFe bilayer where the Cu layer creates a negligible SOT (Figure 53).

The right panel of Figure 52 shows the optical microscopy image and the measurement geometry of the Hall bar structure. An external in-plane magnetic field B_{ext} (= 25 mT – 4 T) is applied with varying the

azimuthal angle (φ) between B_{ext} and the AC current I. Because of the easy-plane anisotropy of NiFe layer, the magnetization is aligned along B_{ext}.

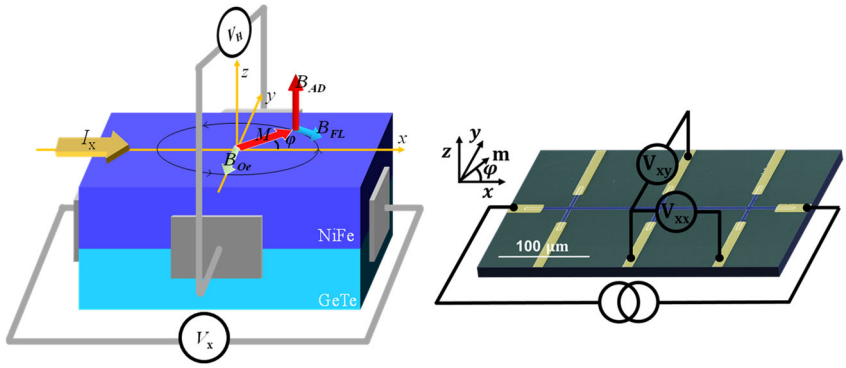

Figure 48. Schematic cartoon representing the harmonic Hall measurement and the optical microscope image of the device

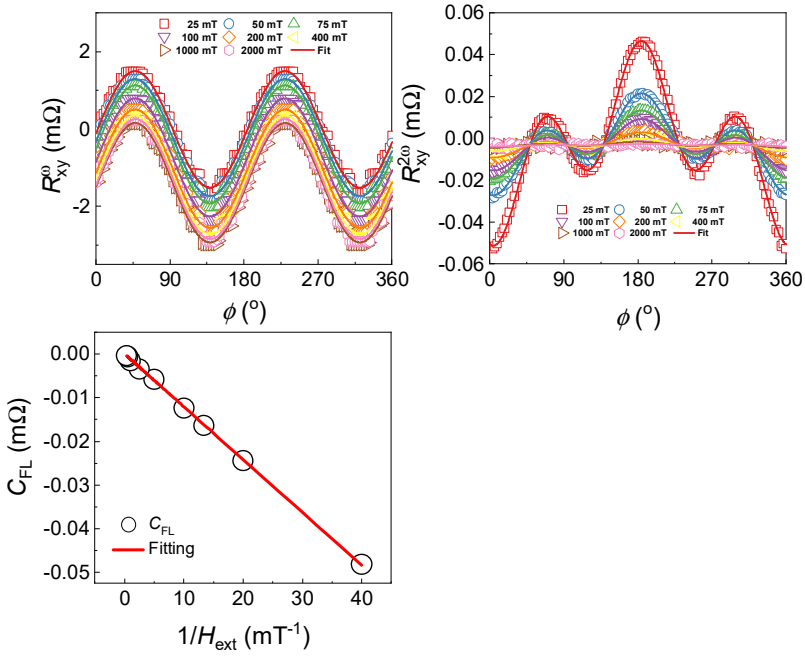

Figure 49. Control experiment result for determination of the sign of current induced Oersted field using Cu (20 nm) / NiFe (10 nm) bilayer.

In this field geometry for the in-plane magnetization, the first (R_{xy}^{ω}) and second $(R_{xy}^{2\omega})$ harmonic Hall resistances are expressed as [121,122]

$$R_{xy}^{\omega} = R_{PHE} \sin 2\varphi \quad \text{---------- (1)}$$

$$R_{xy}^{2\omega} = 2R_{PHE} \frac{B_{FL} + B_{Oe}}{B_{ext}} \cos 2\varphi \cos \varphi + \left(R_{AHE} \frac{B_{DL}}{B_{eff}} + AI_0 \alpha \nabla T + NI_0 \alpha B_{ext} \nabla T \right) \cos \varphi$$

$$= C_{FL} \cos 2\varphi \cos \varphi + C_{DL} \cos \varphi \text{ --------- (2)}$$

where R_{PHE} is the planar Hall resistance, R_{AHE} is the anomalous Hall resistance, B_{eff} is the sum of B_{ext} and the effective out-of-plane demagnetizing field B_d, A is the coefficient of the thermomagnetic effects including the anomalous Nernst effect and the spin Seebeck effect, I_0 is the amplitude of AC current, α is the geometrical factor, ∇T is the vertical temperature gradient, N is the ordinary Nernst coefficient, and B_{Oe} is the current-induced Oersted field. The vertical temperature gradient may originate from the current-induced Joule heating and the asymmetric heat flow between the layers. We note that in comparison to Ref. [121], the ordinary Nernst term, which is linear in B_{ext}, is included in Eq. (2) because this term is found to be large in our GeTe/NiFe structure as we show below. A recent experiment [122] reported that the ordinary Nernst term is also large in a Bi-Sb/Co heterostructure.

Figure 54 shows the measured first and second harmonic Hall resistances, respectively. The first harmonic Hall resistance R_{xy}^{ω} follows the angular dependence of $\sin 2\varphi$ as expected from the planar Hall effect [Eq. (1)]. On the other hand, the second harmonic Hall resistance $R_{xy}^{2\omega}$ shows the angular dependences of $\cos \varphi$ and $\cos 2\varphi \cos \varphi$, consistent with Eq. (2), which will be analyzed in detail in the next section.

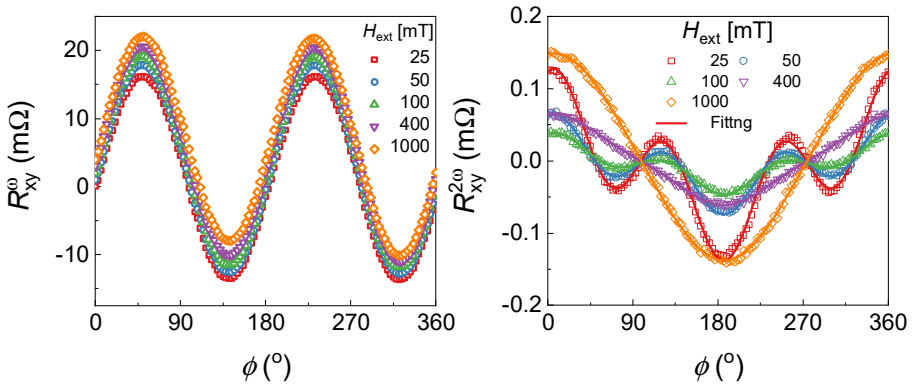

Figure 50. The first harmonic and the second harmonic Hall resistance as the function of ϕ of 130 nm GeTe / 20 nm NiFe bilayer.

4.3.2 Field-like torque of GeTe/NiFe structure

The field-like toque is described by the in-plane effective spin-orbit field (B_{FL}) inherently separated from thermal contributions as shown in the second harmonic Hall resistance ($R_{xy}^{2\omega}$) of Eq. (2). Thus, this term can be directly extracted from the first term of Eq. (2). Figure 55 shows the amplitude of $\cos 2\varphi \cos \varphi$ term, C_{FL}, in GeTe(130 nm)/NiFe(20 nm) bilayer. The C_{FL} is inversely proportional to the external field B_{ext}, consistent with Eq. (2). From the first harmonic results of Figure 54 and Eq. (1), we find that R_{PHE} is 14.95 mΩ. From the channel dimension of Hall bar structure and

resistivities (ρ_{GeTe} = 176.7 μΩ·cm, ρ_{NiFe} = 41.7 μΩ ·cm) and Ampere's law [123], we estimate the current-induced Oersted field (B_{Oe}/J) of −8.1 mT/(10^7 Acm^{-2}), where J is the current density flowing through the GeTe layer. Combining these values with $C_{FL} = 2R_{PHE}(B_{FL} + B_{Oe})/B_{ext}$, we find a field-like toque (B_{FL}/J) of +12.0 mT/(10^7 Acm^{-2}), which is larger in magnitude than B_{Oe}/J, and, more importantly, its sign is opposite to B_{Oe}/J. This sign difference unambiguously demonstrates that a spin-orbit-originated field-like torque is present in GeTe/NiFe bilayers. The field-like torque is found to be linear in the AC current [Figure 56; see Figure 57 for detailed harmonic curves], validating the estimation of B_{FL}/J. We also confirm that $\cos 2\varphi \cos \varphi$ term is absent in a GeTe/Cu structure (Figure 58), evidencing that B_{FL} is not an artifact originating from GeTe itself.

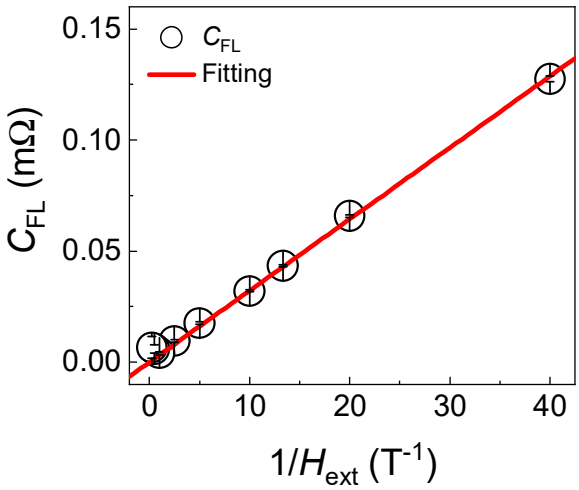

Figure 51. C_{FL} as the function of 1 / H_{ext}, which is extracted from the data fitting of the second harmonic Hall resistance in Figure

54.

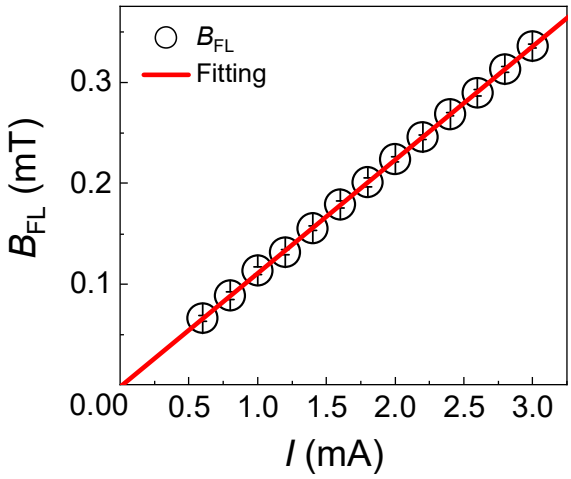

Figure 52. Current (*I*) dependence of the extracted field like spin-orbit torque (B_{FL}).

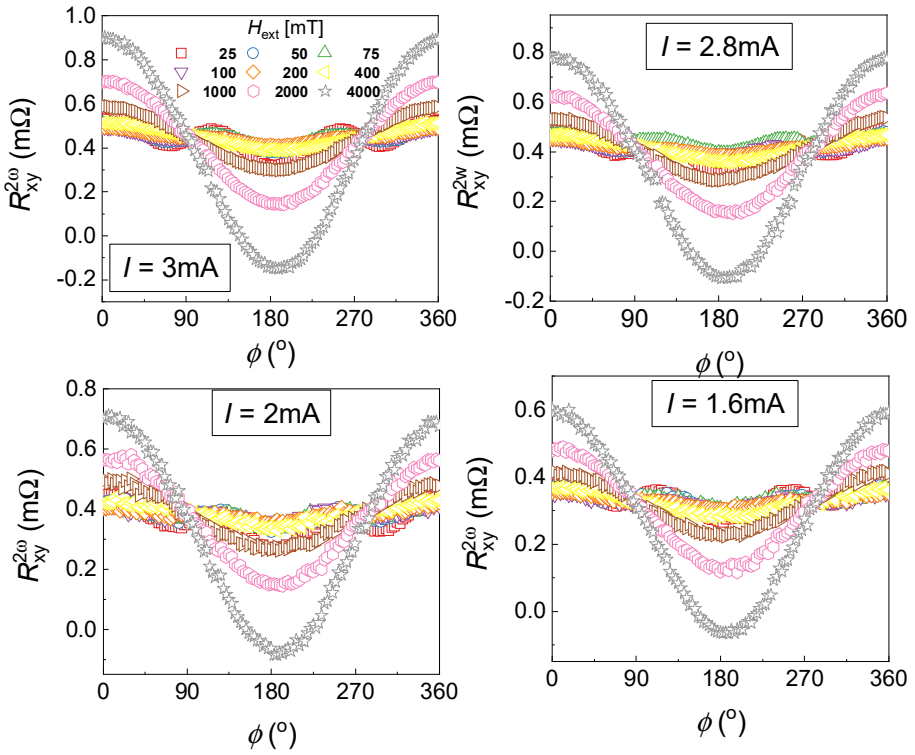

Figure 53. Second harmonic Hall resistance as a function of ϕ with the various bias current (I).

Assuming that the bulk SOC of GeTe is the only source of spin current, one can analyze the magnitude of B_{FL}/J based on the spin drift-diffusion model with the quantum mechanical boundary condition [108]. This model predicts that B_{FL}/J increases and then saturates when the NM thickness exceeds its spin diffusion length. It also predicts that B_{FL}/J is inversely proportional to the FM thickness as reported in a recent experiment [124].

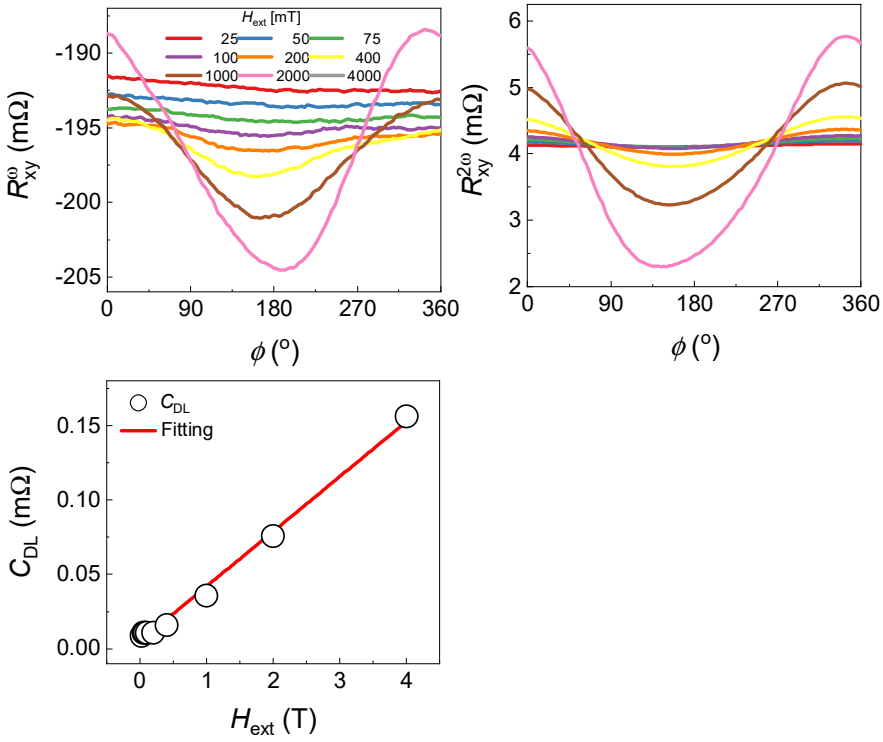

Figure 54. Control experiment of the harmonic measurement using GeTe/Cu structure.

To check whether or not this diffusion model applies to our study, we carry out harmonic Hall measurements for GeTe/NiFe bilayers with varying GeTe thickness and NiFe thickness [Figure 59]. For the GeTe-thickness dependence, B_{FL}/J shows a slightly nonlinear dependence on the GeTe thickness but does not exhibit a clear saturation behavior. One possible explanation is that the spin diffusion length of GeTe is comparable to or larger than the largest

tested GeTe thickness (170 nm). This explanation is however unlikely because the spin diffusion length of most spin-orbit channels is of nanometer scale [125]. Moreover, for the NiFe-thickness dependence [Figure 59], we find that B_{FL}/J is almost constant even with a threefold change in the NiFe thickness. This behavior is inconsistent with the prediction of the spin drift-diffusion model. Therefore, these results, in particular, the NiFe-thickness dependence, suggest that the bulk SOC of GeTe is not the only source of spin current.

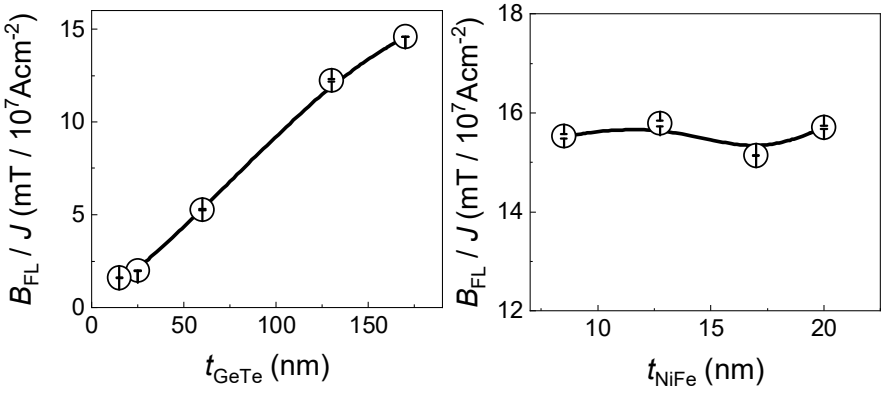

Figure 55. The GeTe and NiFe thickness dependence of the field-like spin-orbit torque.

We check several possibilities for the unconventional thickness dependence of field-like torque. We first check whether or not a thick magnetic dead layer is formed at the GeTe/NiFe interface. We find that the magnetic dead layer is only 0.36 nm thick [Figure 60] so we

exclude this possibility for the unconventional NiFe-thickness dependence of field-like torque. As recent studies have reported that the oxidation affects SOT significantly [126-128], we also check whether or not an oxide layer is formed at the GeTe/NiFe interface with Auger spectroscopy but find no noticeable signs of oxidation (Figure 61).

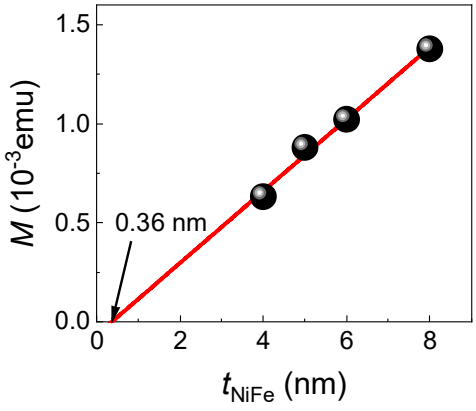

Figure 56. Magnetization as a function of NiFe thickness to identify the thickness of the magnetic dead layer.

Yet another possibility is the interface SOC at the GeTe/NiFe interface. The spin drift-diffusion model is obtained by integrating the Boltzmann equation so that the Boltzmann equation is better suited to describe in-plane transport [108]. Boltzmann transport calculation [108] for the interfacial SOC shows that the scaled field-like torque [= (field-like torque)×(FM thickness)] increases and then

saturates with increasing the FM thickness. In other words, it predicts that the field-like torque is not scaled with 1/(FM thickness) but more or less constant in some ranges of the FM thickness. Our observation [Figure 59] is qualitatively consistent with this prediction considering the interface SOC. Therefore, we attribute the unconventional NiFe-thickness dependence of field-like torque to the interface effect, which may be enhanced due to the bulk Rashba SOC of GeTe.

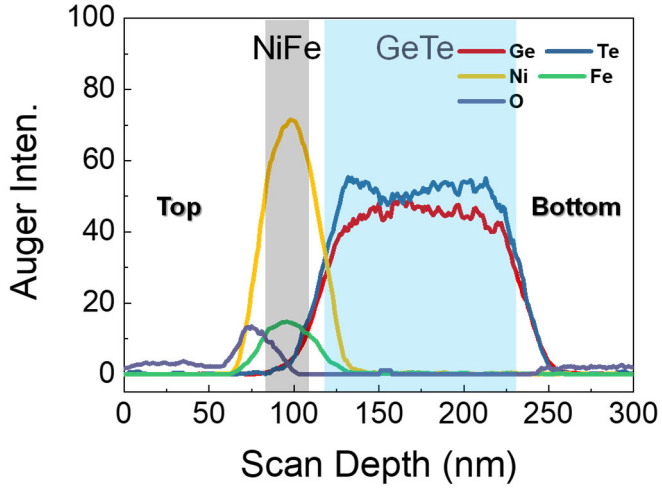

Figure 57. Qualitative compositional analysis with the Auger spectroscopy of GeTe / NiFe bilayer.

4.3.3 Damping-like torque of GeTe/NiFe structure

Based on the second harmonic Hall resistance ($R_{xy}^{2\omega}$), we attempt to extract the magnitude of damping-like torque in GeTe/NiFe

bilayers. The damping-like torque is expressed as the out-of-plane effective spin-orbit field (B_{DL}), which can be extracted from the amplitude of $\cos\varphi$ term in Eq. (2). However, several thermomagnetic effects [121,122] such the ordinary Nernst effect, the anomalous Nernst effect, and the spin-Seebeck effect are also present in the second harmonic signals. The damping-like term amplitude $C_{DL} = R_{AHE}\frac{B_{DL}}{B_{ext}+B_d} + AI_0\alpha \bigtriangledown T + NI_0\alpha B_{ext} \bigtriangledown T$ includes three terms that depend on B_{ext} in different ways. From the independent experiments, we find R_{AHE} of 3.41 mΩ and B_d of 1T (Figure 62). As shown in Figure 63, C_{DL} fits well to Eq. (2). However, the third term of C_{DL}, $NI_0\alpha B_{ext} \bigtriangledown T$, which is linear in B_{ext}, dominates other two terms [see the right panel of Figure 63]. Even though the first ($R_{AHE}B_{DL}/B_{eff}$) and second ($AI_0\alpha \bigtriangledown T$) terms have different dependences on B_{ext}, the combined magnitude of these terms is too small to reliably separate. As a result, we are unable to estimate the damping-like torque of GeTe/NiFe bilayer, which is believed to be much smaller than the field-like torque.

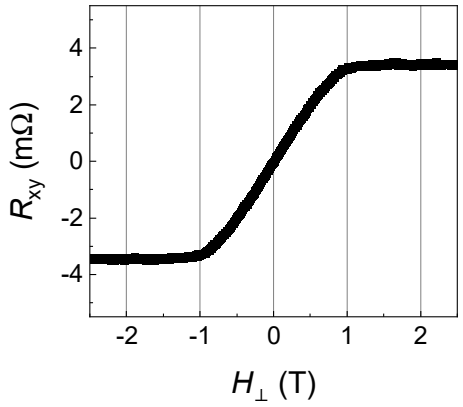

Figure 58. Anomalous Hall measurement with the out-of-plane magnetic field of $Ni_{81}Fe_{19}$.

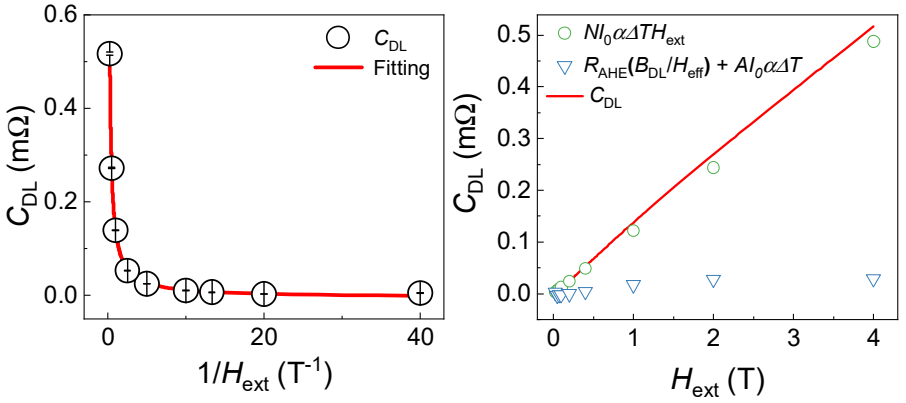

Figure 59. C_{DL} which is extracted from the data fitting of the second harmonic Hall resistance in Figure 54.

4.4 Discussion

As the only field-like torque is reliably estimated from measurements, we focus on the field-like torque and its possible utilization. An interesting observation in our work is that the field-like torque is weakly dependent on the FM thickness, which is in stark contrast to a typical inverse proportionality of SOT magnitude to the FM thickness. It suggests that the bulk SOC of GeTe is not the only source of spin current in GeTe/NiFe bilayers. Rather, the spin current is noticeably attributed to the interfacial SOC at the GeTe/NiFe interface. The large field-like torque indicates a large interfacial SOC effect. The bulk Rashba effect of GeTe itself may have a role in the large interfacial SOC effect, which demands further theoretical studies.

Another interesting observation is that the field-like torque is large even for a thick FM layer. Considering the FM thickness, the field-like torque of GeTe/NiFe bilayer in this study is noticeably large. This large field-like torque for a thick FM layer suggests that GeTe/FM bilayers can be used for scalable in-plane SOT magnetic random access memories (MRAMs). Even though SOT can switch in-plane magnetization [113,129], in-plane MRAMs suffer from inferior scalability to perpendicular MRAMs. The thermal energy barrier Δ of in-plane MRAM is given by $K_s V/k_B T$ where K_s is

the shape anisotropy, V is the FM-layer volume, and k_BT is the thermal energy at room temperature. Fig. 3(F) shows a contour map of the calculated Δ as the function of the in-plane length L and the thickness t of the FM layer, assuming the in-plane aspect ratio of 2 and the saturation magnetization of 800 emu cm^{-3}. It clearly shows that $\Delta > 50$ for 10-year retention cannot be reached for a thin FM layer. One has to increase the FM thickness to meet the criteria of $\Delta > 50$. When the SOT is inversely proportional to the FM thickness, however, it costs an increased write current, resulting in high power consumption. In this respect, the large field-like torque of GeTe/NiFe bilayers for a thick NiFe layer and its weak dependence on the NiFe thickness are attractive for scalable in-plane MRAMs.

Finally, we have checked the possibility of electrically controlling the SOT of GeTe/NiFe bilayers. This is one of our original motivations for this study because GeTe is a well-known ferroelectric material and is expected to exhibit gate-controlled electric polarization and subsequent Rashba effect modulation in a nonvolatile manner. However, we find no noticeable modulation of the field-like torque by gating (Figure 64) due to the relatively high conductivity of GeTe and/or the inefficiency of back-gating. Therefore, we need to engineer the material itself or develop an alternative method for the electrical control of polarization, which is beyond the scope of this work.

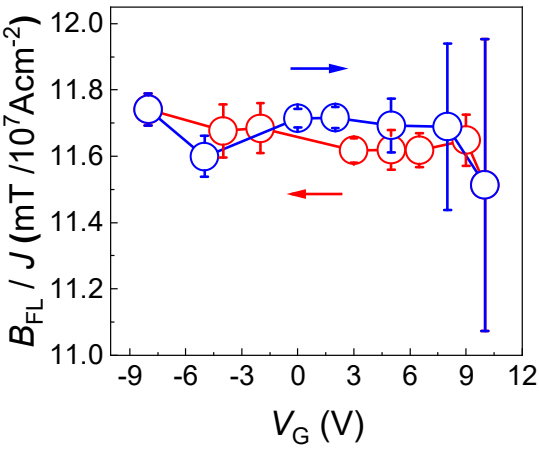

Figure 60. Gate field dependence of the field-like spin-orbit torque of GeTe / NiFe bilayer.

Chapter 5.

Magnetotransport properties of the $[Bi_2Te_3|GeTe]$ superlattices

5.1 Introduction

The second-generation spintronics [18,19,130-133], which features the electrical control of the spin of charge through the spin-orbit (SO) coupling, enables energy-efficient spintronics devices [22,134,135]. Ferroelectric Rashba semiconductors (FeRSCs) [1,7,8,26,136,137] are the materials that exhibit the bulk Rashba effect induced by spontaneous electric polarization and strong SO coupling. FeRSCs are promising second-generation spintronics materials in that the Rashba effect can be controlled through ferroelectric polarization [119,138-140]. The prototype of FeRSCs; GeTe (GT) [10-12,141] with the largest Rashba constant ($\alpha_R \sim 4.3$ eV*Å) has attracted much interest not only as a platform for the theoretical study of bulk Rashba effect but also in applications such as SO torque magnetic random access memory [142] (SOT-MRAM) and novel non-volatile spintronic memory [143].

The huge bulk Rashba effect in GT was theoretically proposed by Sante et al. in 2013 [7]. The following studies have successfully

verified the ferroelectricity coupled Rashba effect of GT by the study of spectroscopy or electrical measurements [9,11,12,46,139,141,142]. Nevertheless, the spintronics development using GT is slow in progress due to the high p-type carrier density of GeTe around 10^{20}-10^{21} /cm^3 screening the external electric field. These p-type carriers are known to originate from Ge vacancy [4,144,145], which is energetically stable in GT having a rhombohedral structure below 670 K. GT's high conductivity makes ferroelectric switching difficult or significantly lowers power efficiency [47,138,146,147], as well as weakens the Rashba effect in real carrier transport [120]. Therefore, an approach to efficiently engineer the carrier density of GT is demanding.

To this end, we have investigated a superlattice (SL) composed of GT and Bi_2Te_3 (BT). Note that SL has advantages: there is no limitation of solubility, so the window for the allowable composition is not limited, and the structural properties of the constituents can be maintained. BT which is one of the components of SLs is an n-type semiconductor and has the same rhombohedral crystal structure (space group of BT=$R\bar{3}m$) as GT (space group of GT=$R3m$) and shares Te [148,149]. In addition, BT, a typical 3D topological insulator, has a large SO interaction [150] which is an essential ingredient for spintronics applications.

In this study, we investigate the transport properties of 25 [BT|GT] SLs designed to systematically study the dependence of the SL parameters such as the period, composition, and repetition. The superlattice parameters for maximally reducing the carrier density have been found, and recovery of the Rashba constant according to carrier density reduction was confirmed from the weak antilocalization analysis [97,151-153]. The results of this study, which effectively suppressed the p-type carrier of GT through SL of GT and BT, suggest an effective strategy for improving the ferroelectric switching efficiency of GeTe and recovering the Rashba effect, which will lead to the development of spintronics devices utilizing GT.

5.2 Experimental method

5.2.1 Film growth and characterization

[BT|GT] SLs were grown with 50nm thickness by thermal evaporation of atomic sources (Bi, Ge, and Te) on an intrinsic Si (111) substrate at the growth temperature of 250 ºC. Before loading into the process chamber, Si (111) was cleaned in the following order: Piranha cleaning, SC1 cleaning, and removal of natural SiOx in diluted HF solution. Loaded into the process chamber which has a base pressure of ~10^{-8} Torr, the substrate was preheated to 150 ºC for 1 hr to remove residual water on the surface and heated to the growth temperature of 250 ºC. The buffer layer of 2 nm GT was deposited on Si (111) for reducing the lattice mismatch with BT (surface image of Si (111) / buffer GT is shown in Figure S1). The fluxes of Bi, Ge, and Te were controlled by the quartz crystal microbalance (QCM) thickness monitor. The fluxes were set as 0.1, 0.4, and 2.0 Å/s for Bi, Ge, and Te respectively during the growth. By controlling the shutters with the time interval of 5 sec, BT and GT were alternately grown. The grown SL films were characterized using XRD (Empyrean, Malvern Panalytical), AFM (XE-70, Park systems), and TEM (TitanTM 80-300, FEI) analysis.

5.2.2 Carrier transport measurement

The [BT|GT] SLs films were cut into the 5x5 mm^2 square and electrical contacts were made at four edges of the samples with indium. The samples were loaded into a commercial cryogen-free cryostat (Cmag Vari.9, Cryomagnetics Inc.) and measured in the temperature range of 1.8~250 K and the magnetic field range of -9 ~ 9 T. The longitudinal and the Hall resistances were measured using the conventional Van der Pauw method. In the measurement, an SMU (2612A, Keithley Inc.) as a current source and a nano-voltmeter (2182, Keithley Inc.) as a voltage meter were used.

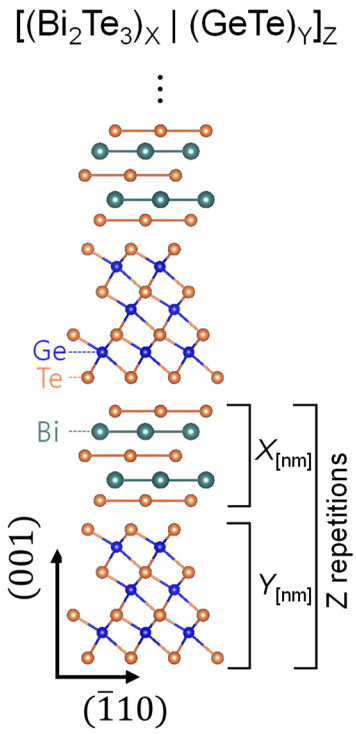

Figure 61. Schematic cartoon representing the structure of [BT|GT] SLs

5.3 Result and Discussion

5.3.1 Structural characterization of [BT|GT] SLs

SL films that have the unit layer of [BT_X | GT_Y] (X and Y are 1,2,3,4, and 6 nm) repeated to have a total thickness of ~50 nm were grown by thermal evaporation (See *Experimental method* section for details in the growth process). Thus, 25 [BT|GT] SLs were prepared

for the systematic study of the carrier transport depending on the superlattice parameters according to compositions (or the ratio between BT and GT), periods (the thickness of the unit layer), and repetitions of the unit layers.

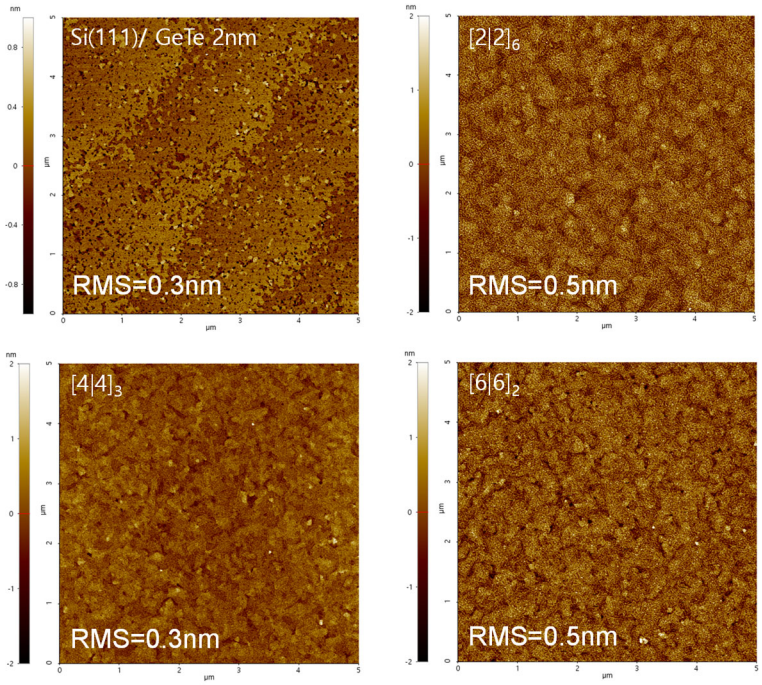

Figure 62. AFM topography for the inspection of surface properties

The flat and continuous surface properties are verified by the AFM (Figure 66). They guarantee no artifact signal which can be induced by the rough surface during the transport measurement. The cross-section of SLs inspected by scanning transmission electron

microscopy (STEM) of the symmetric SLs (X=Y=1,2,3,4, and 6), and an asymmetric SL (X=2 and Y=6) are shown in Figure 67.

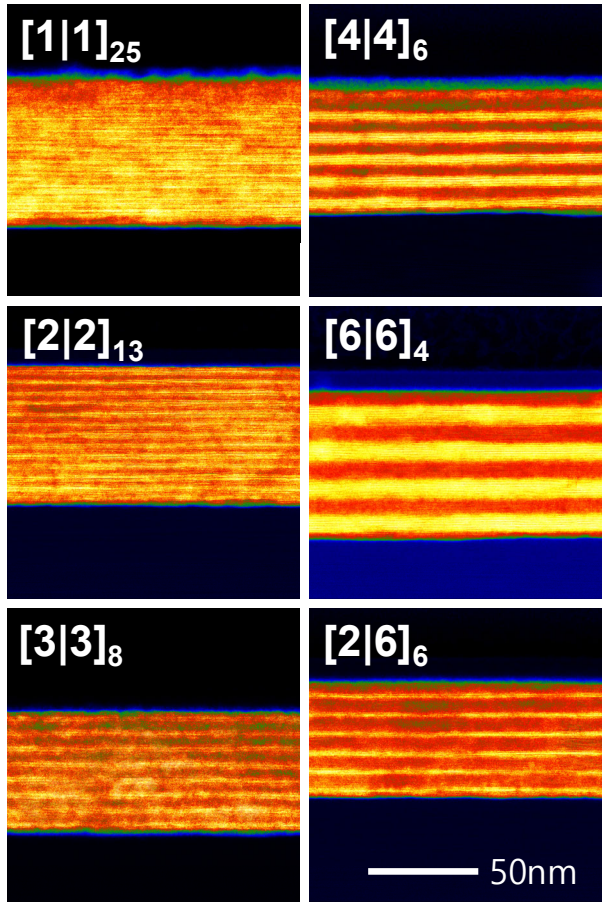

Figure 63. STEM X-section image of [BT|GT] SLs

Even with the smallest period ($[1|1]_{25}$), SLs show exactly separated unit layers satisfying the intended period and number of repetitions. The SLs having a small period ($X= Y \leq 3$) show blurred interfaces

implying phase mixing (or alloying) between BT and GT domains. However, $[4|4]_6$ and $[6|6]_4$ show sharp interfaces because the alloying is limited to ~1 nm. That will be discussed again below. The out-of-plane (OOP) crystallinity of the same SLs used for STEM measurements is investigated by XRD theta-2theta measurements (Figure 68).

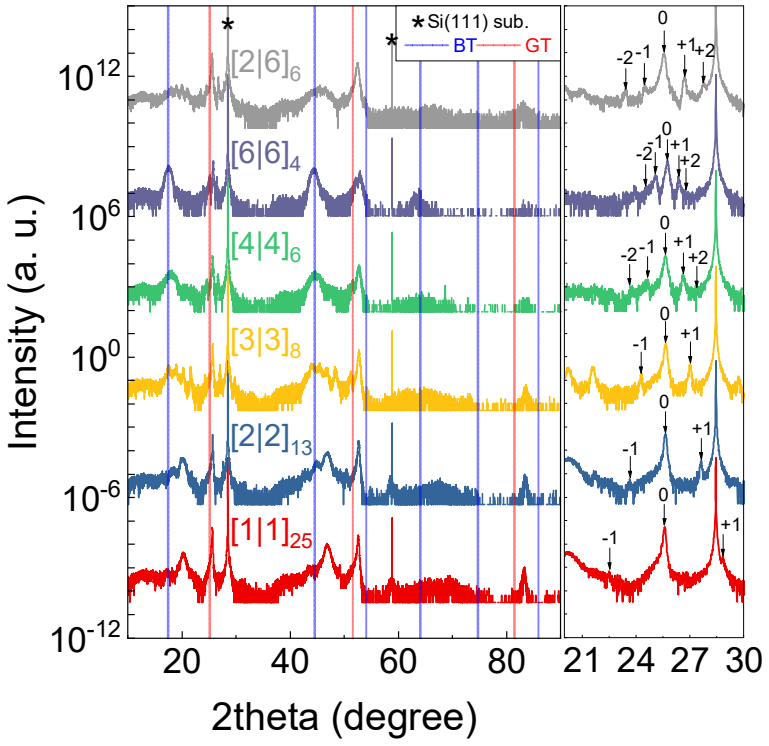

Figure 64. XRD theta-2theta scan of [BT|GT] SLs.

The (000n) peak positions picked from the bulk GT and BT are indicated with XRD 2theta data of SLs by red and blue vertical lines, respectively. It is 2theta= 25.106, 51.558, and 81.43 ° for the GT (0003), (0006), and, (0009) planes, respectively. And, it is 2theta= 17.37, 44.51, 54.035, 64.05, 74.66, and 85.86 ° for the BT (0006), (00015), (00018), (00021), (00024), and (00027) planes, respectively. A clear c-axis prepared orientation of the GT has been confirmed in all measured SLs, although the XRD characteristic peak of BT is only confirmed at X = Y ≥ 3. The satellite peaks conspicuous around GT (0003) account for the SL XRD peaks.

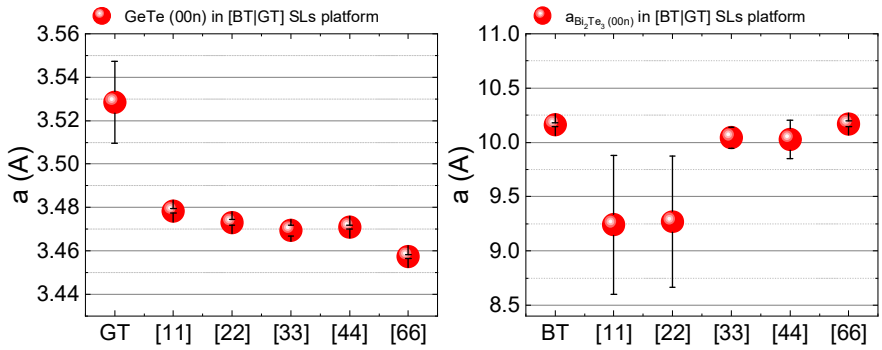

Figure 65. The lattice constant of GT (0003) and BT (0003) extracted from XRD peak positions of Figure 68.

Figure 69 shows the lattice constants converted from the peak positions of GT (000n) and BT (000n) as a function of the period. The lattice constant along the c-axis of the GT is gradually decreased

as the period increases. The decrease in the c-lattice of GT is due to the strain effect from the lattice mismatch of ~5 % between GT and BT, and GT can experience compressive strain along the c-axis due to the tensile stress of the ab plane. This strain effect is also confirmed by the XRD reciprocal space mapping and high-magnified STEM images (Figure 70-72). In the case of BT which has a 2D structure the strain effect is hardly confirmed, but in [1|1] and [2|2] samples having small periods show a large shift of BT(000n) reflections. It is associated with the presence of the mixed phase in the BT/GT interface, and it is also confirmed in high-magnified STEM images (Figure 71). Note that the clear separation between the GT and BT phase in SLs with a period longer than [3|3] is confirmed. It together with the observed strain effect consistently indicates that the phase mixing is limited within ~1 nm interface rather than diffusion into the bulk.

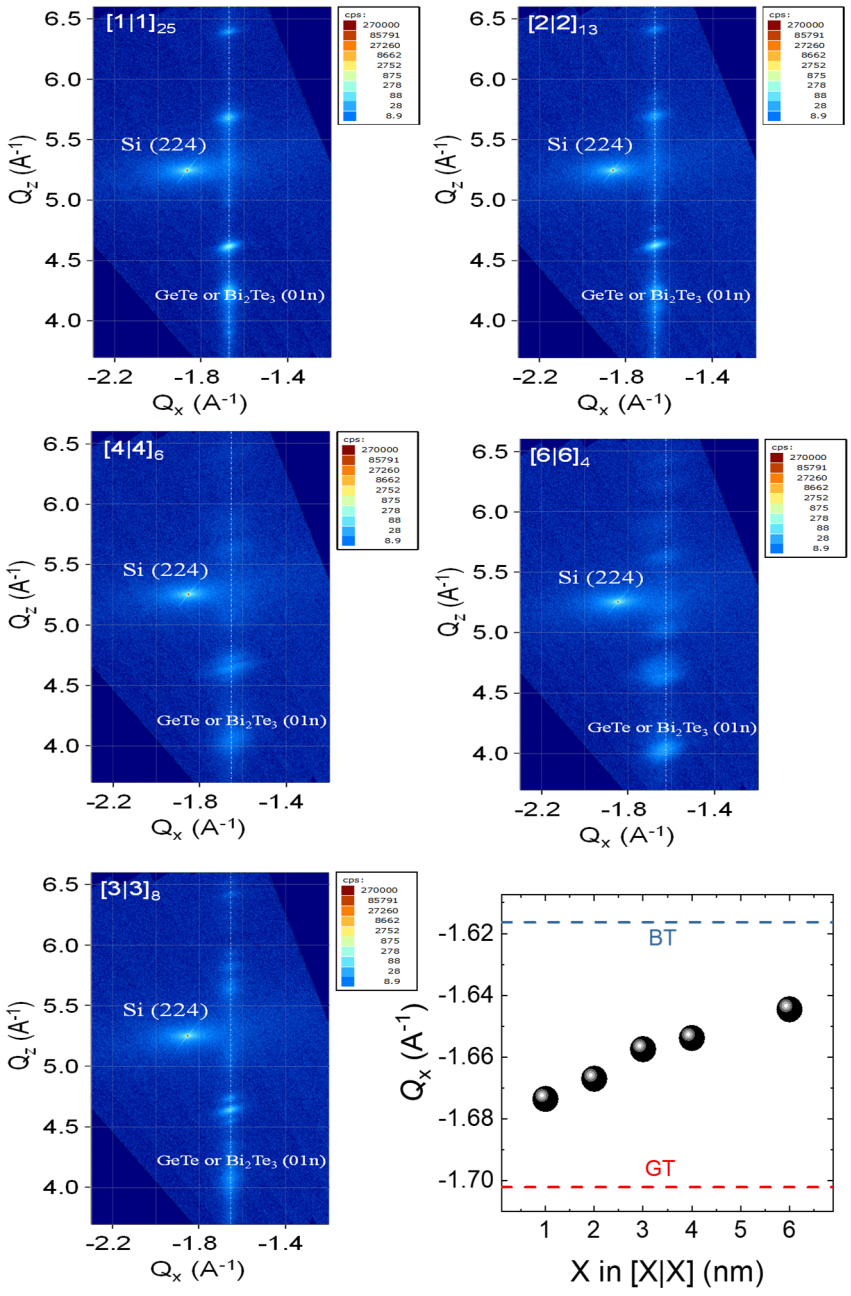

Figure 66. XRD reciprocal space map of [BT|GT] SLs.

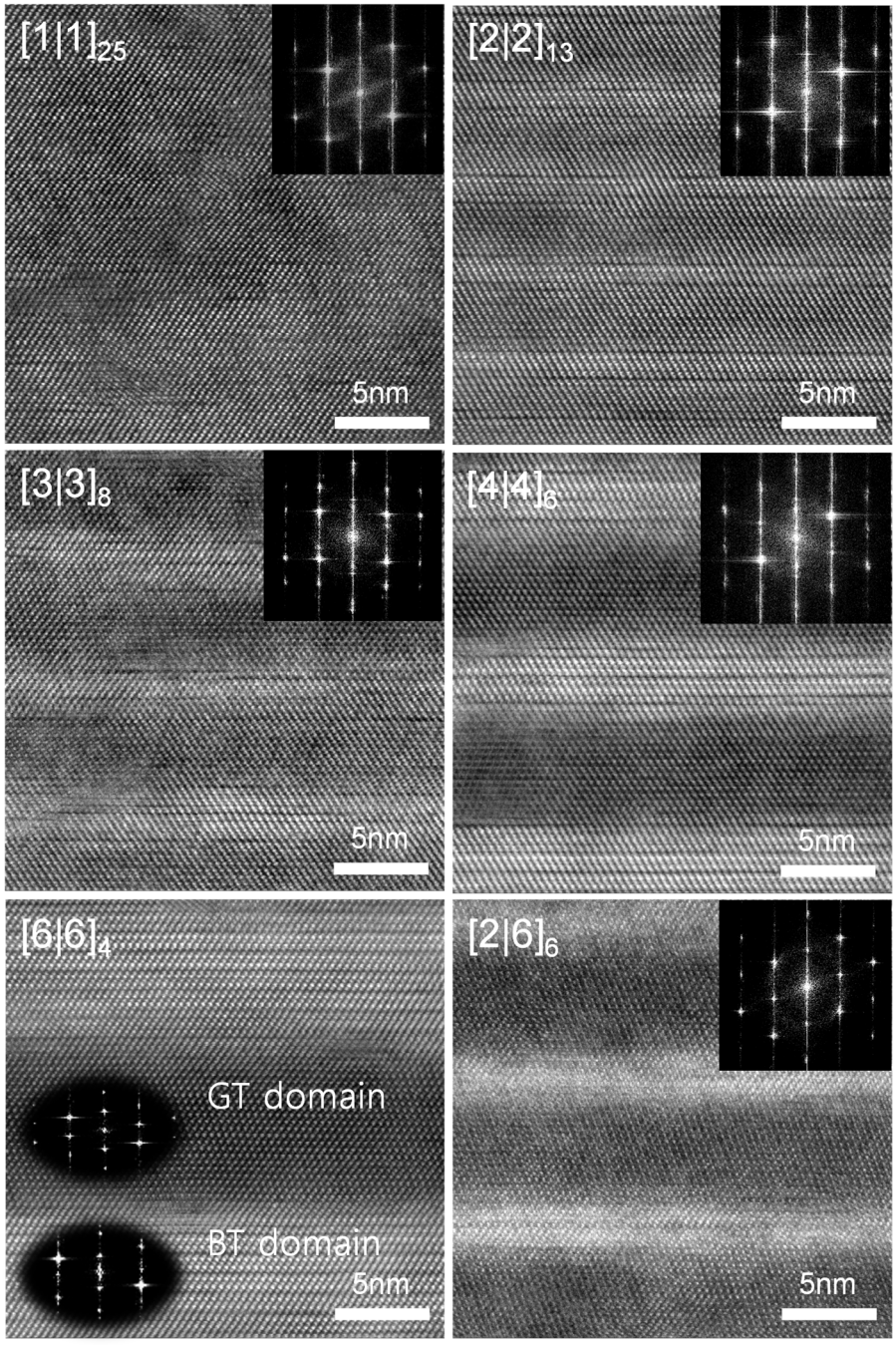
[1|1]25
5nm
[2|2]13
5nm
[3|3]8
5nm
[4|4]6
5nm
[6|6]4
GT domain
BT domain
5nm
[2|6]6
5nm

Figure 67. STEM cross-section images of [BT|GT] SLs.

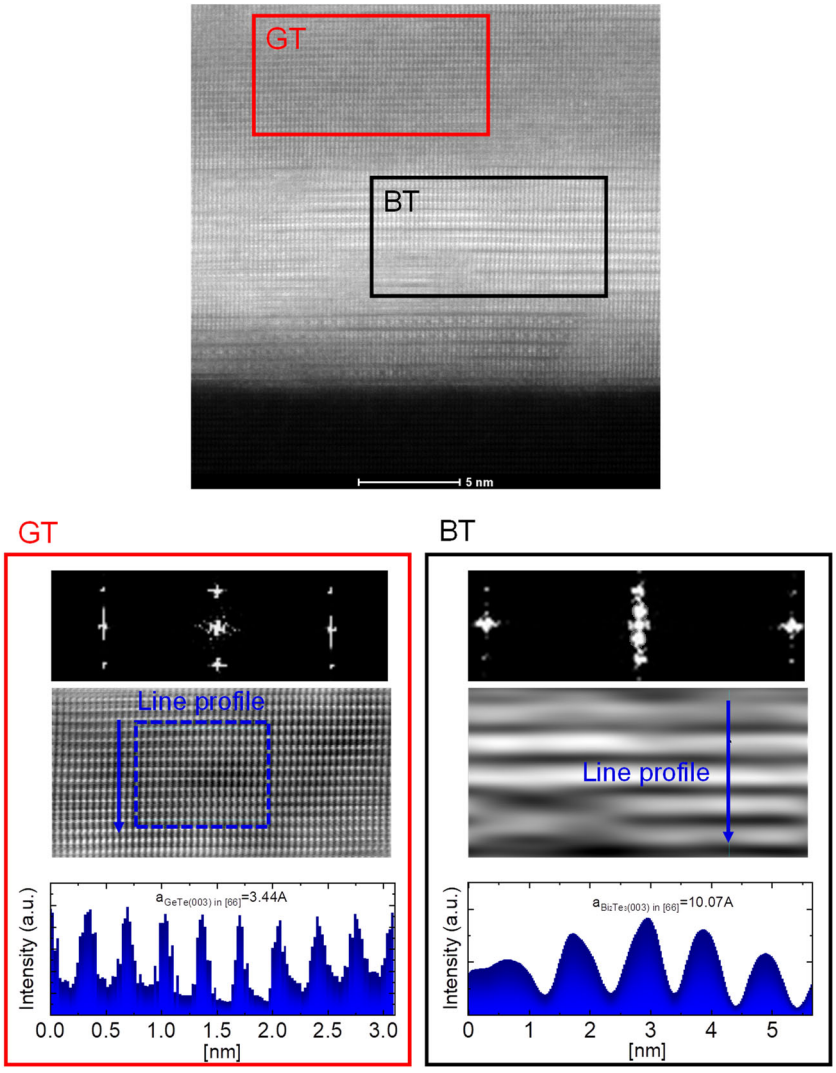

Figure 68. Lattice constant analysis of [4|4] SL through the STEM image.

5.3.2 Transport properties of [BT|GT] SLs

The carrier transport properties of [X|Y] (X, Y=1,2,3,4, and 6) have been investigated by measuring the longitudinal and Hall resistance at various temperatures and magnetic fields (Figure 73-75). Figure 76 summarizes resistivity, carrier density, and mobility according to the thickness of GT and BT in the unit layer as color maps. As the thickness of BT increases, the carrier density decreases to the minimum of 5.7×10^{19} / cm^3 (equivalent to ~1/8 of GT single film, ~1/3 of BT single film) in the [2|6] (Figure 76). The maximum carrier compensation is acquired in the case of BT/GT ~ 3. It is related that GT single film (4.36×10^{20} / cm^3) has ~3 times larger carrier density compared to BT single film (1.49×10^{20} / cm^3). The changes in carrier type from the hole (p) to the electron (n) are observed when GT=1nm and BT/GT $\geq$ 3 ([1|3], [1|4], and [1|6]). It is associated with that the free electrons in the BT domain (n_{BT} x thickness of BT) overtake the free holes in the GT domain (n_{GT} x thickness of GT).

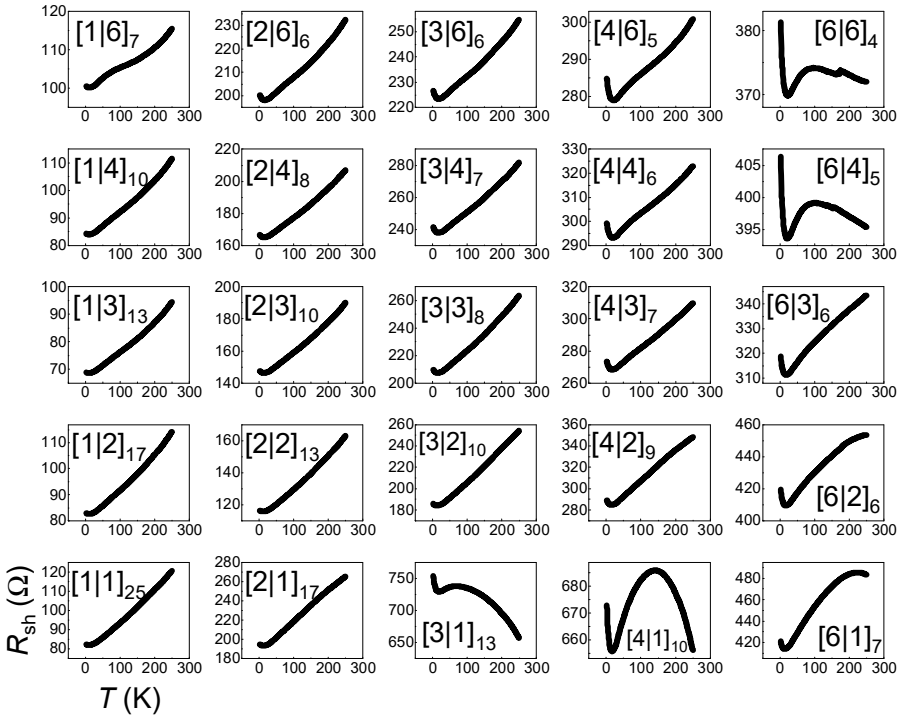

Figure 69. The sheet resistance (R_{sh}) as a function of the temperature of [BT|GT] SLs.

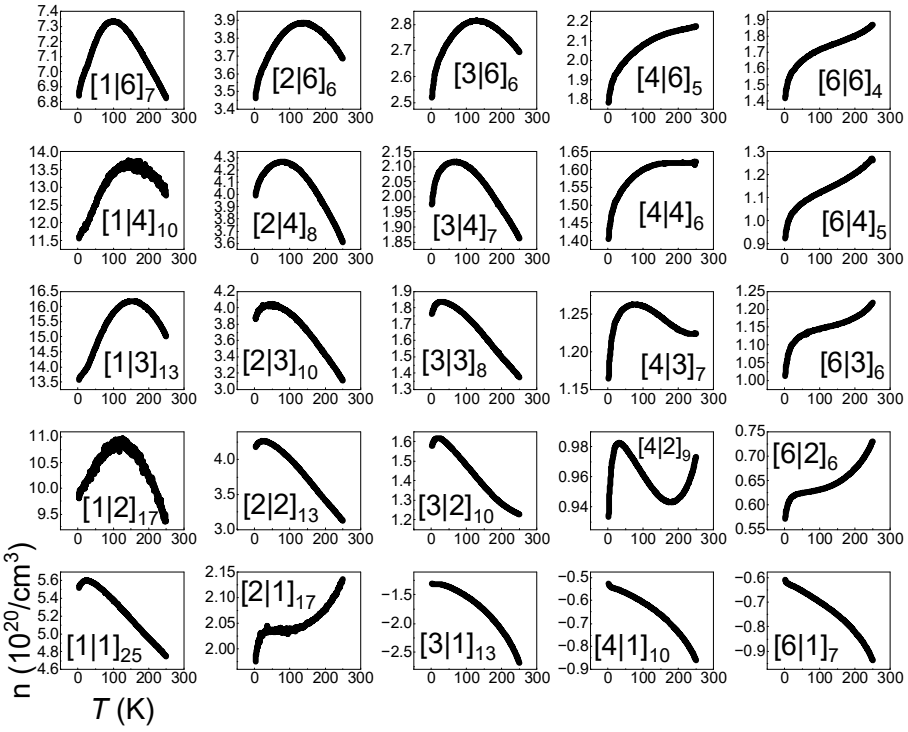

Figure 70. The carrier density (*n*) as a function of the temperature of [BT|GT] SLs.

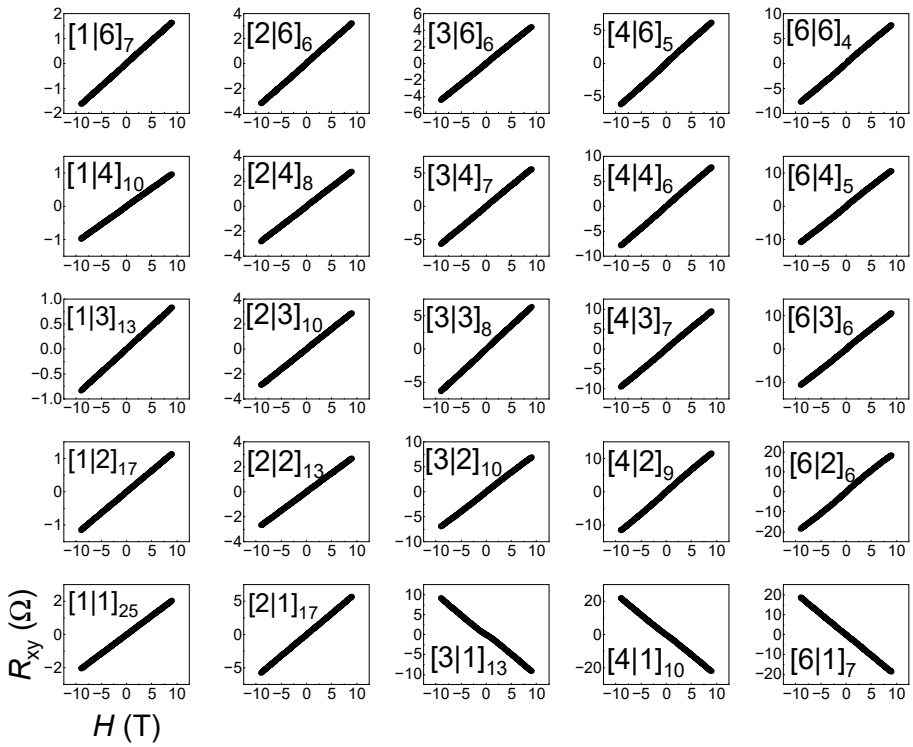

Figure 71. Hall resistance (R_{xy}) vs. the external magnetic field (H) of 25 [BT|GT] SLs.

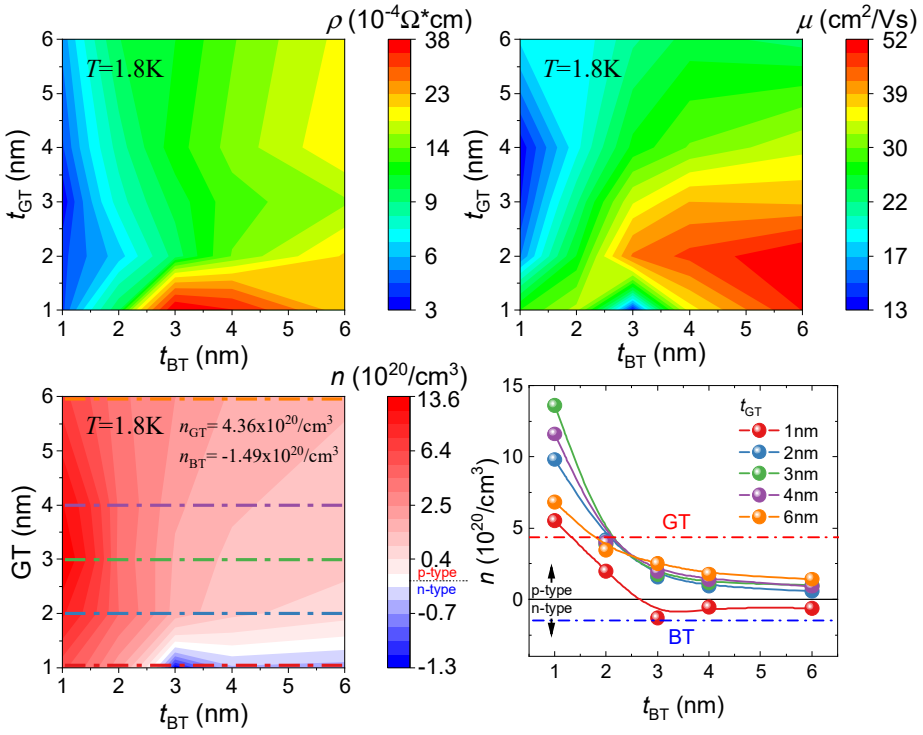

Figure 72. Summary of the basic transport properties of [BT|GT] SLs.

Carrier mobility is the smallest in the upper left and largest in the lower right of the color map, that is, it tends to increase as the fraction of GT is lower (Figure 76). Considering that a single GT film (213 cm^2/Vs) has more than 5 times larger carrier mobility than BT (38.5 cm^2/Vs), carrier transport in [BT|GT] SLs cannot be explained by considering the parallel channels of GT and BT domains. The transport in [BT|GT] SLs cannot be explained by the sum of independent transports in BT and GT channels, and it can be

presumed that a coherent transport channel is formed in the entire SL. This scenario considering a single transport channel in [BT|GT] SLs has been also confirmed from the Hall measurement result showing a linear dependence on the magnetic field, which exhibits single-channel characteristics (Figure 75). Therefore, [BT|GT] SLs have a 3D transport property in that the charge moves freely in the thickness direction, and the mobility is limited by the BT layer with smaller mobility.

Next, the dependence of SL parameters on the transport characteristics of [BT|GT] SLs is discussed. Figure 77(a) shows the dependence of the carrier density on the BT fraction (BT/GT) according to the various fixed periods. It is confirmed that the BT/GT and carrier density show an inverse relationship in all periods. As discussed above, since GT has three times larger carrier density compared to BT, it indicates that a three times larger volume of BT is required for 1:1 compensation doping. As expected, the minimum p-type carrier density is observed in BT/GT ~ 3, and the n-type characteristic is observed when $3 \leq BT / GT$. It can be seen that the maximum compensation effect exists in the regime of $2 < BT / GT < 3$. Figure 77(b) shows the dependence of carrier density on repetition times (z) according to various fixed BT / GT. z represents the number of BT/GT interfaces, and if the compensation doping relies on alloying at the interface, n would be inversely proportional to z.

However, n is proportional to z (Figure 77(b)), and it indicates that at least the compensation effect found in our [BT|GT] SLs is independent of alloying at the interface. For the various fixed BT / GT, the function of carrier density according to the SL period is shown in Figure 77(c). As the SL period increases, the carrier compensation effect is strengthened. And the negative slope of $|n|$ vs. period becomes steeper as the fixed BT / GT increase. As discussed in the z-dependence of carrier density, the compensation doping is not accounted for alloying at the interface, that is, it can not be explained by the substitution of defect sites. It would rather be explained by the charge transfer between the GT and BT domains in the unit layers. Due to the work function difference between GT and BT (GT ~ 4.8 eV, BT ~ 4.5 eV) [138,154], they transfer their major carrier to each other, and a depletion region without mobile charge is formed at the interface. In a period than the depletion length, charge transfer does not come to the equilibrium state. The depletion lengths calculated from the carrier densities of BT and GT are ~2 nm and 0.7 nm, respectively, and the charge transfer would be limited by the thinner BT layer. Indeed, it can be confirmed that as the thickness of BT approaches 2 nm, the effect of compensation doping saturates (inset of Figure 77(c)).

The dependence of carrier mobility on SL parameters is also shown in Figure 77(d)-(e). As the fraction of BT increases carrier mobility

tends to increase (Figure 77(d)). As mentioned in the previous discussion, it is associated with the increase of mobility of the BT domain since carrier mobility in the entire thin film is limited by BT.

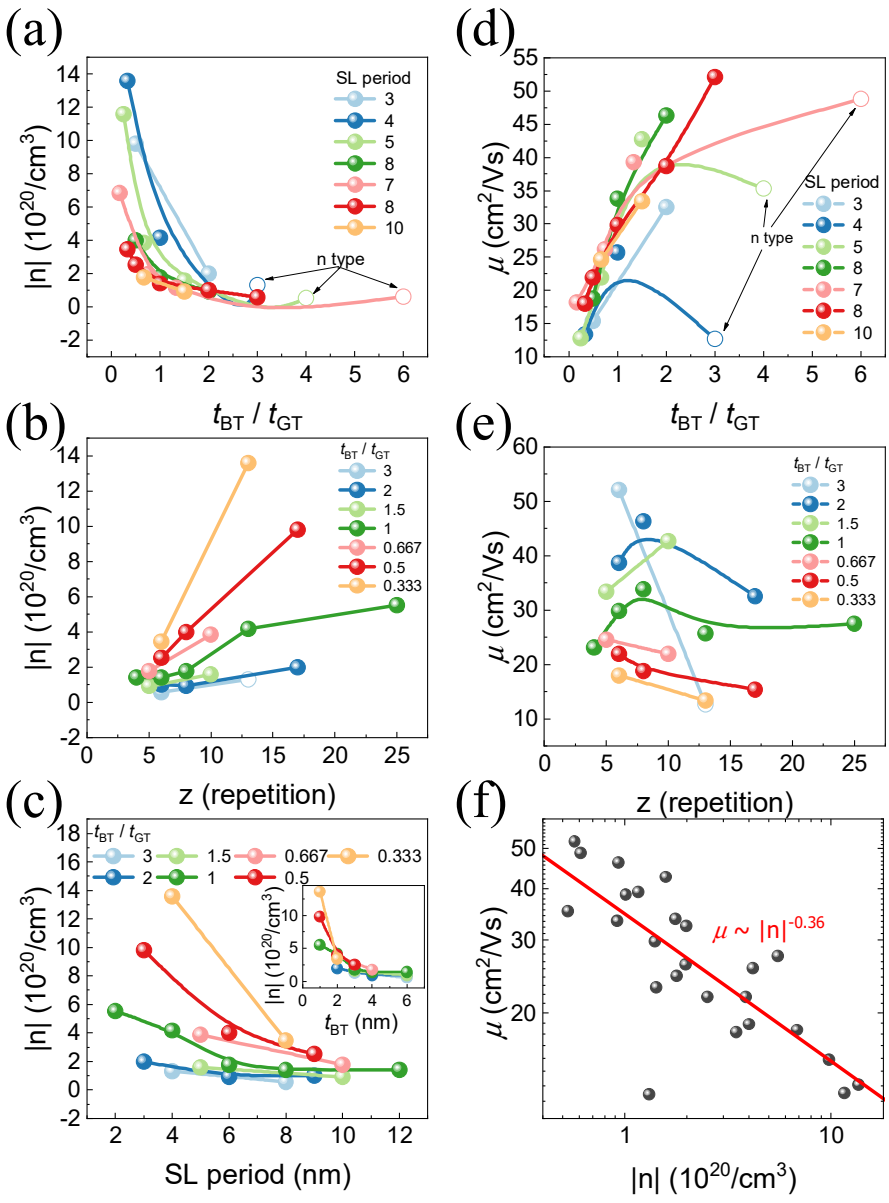

Figure 73. SL parameter dependence of the carrier density (*n*)

and mobility (μ)

5.3.3 Recovery of the Rashba constant of GT in [BT|GT] SLs

For the analysis of Rashba spin-orbit coupling in [BT|GT] SLs, the magnetoresistance (*MR*) as a function of a magnetic field (*H*) has been measured at 1.8K (Figure 78). The *MR*(*H*) curves show a cusp near *H*=0 as well as the classical parabolic MR in the high field regime. The cusp in *MR*(*H*) is the hallmark of weak anti-localization (WAL). WAL or weak antilocalization (WL) in which the cusp evolves to the peak is a quantum interference phenomenon observed in a diffusive system and is widely used to analyze the phase and spin relaxations of electron waves [155-157].

Before the analyze the WAL, the classical *MR* (MR_{ord}) has been excluded from the MR(H) curves. MR_{ord} is proportional to the square of mobility (μ) and magnetic field (*H*) (MR_{ord}~$(\mu H)^2$) because it is related to the cyclone motion of the charge in a vertical magnetic field. Therefore, MR_{ord} can be expressed as $MR(H) = k(H/\rho_0)^2$ through Kohler's rule, and the constant k is a temperature invariant constant assuming that the carrier density is independent of temperature [158]. k has been extracted from *MR*(*H*) of high temperature (100K) at which MR_{ord} dominates *MR*(*H*), and MR_{ord} at 1.8K has been reproduced with this k (Graphical representation of this process is shown in Figure 79).

Figure 80 shows $MR_{wal}(H)$ which is released by subtracting MR_{ord} from $MR(H)$ (Figure 78).

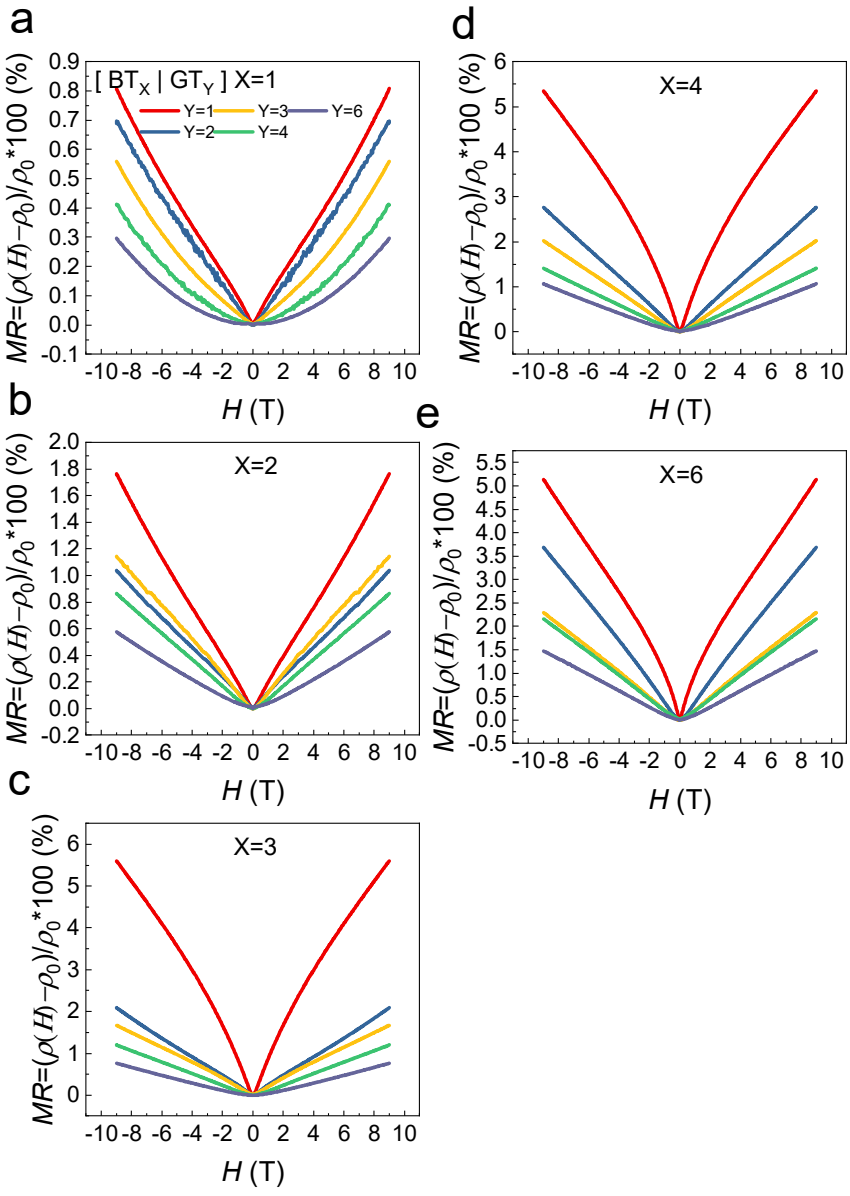

Figure 74. Magnetoresistance as a function of the magnetic field of [BT|GT] SLs.

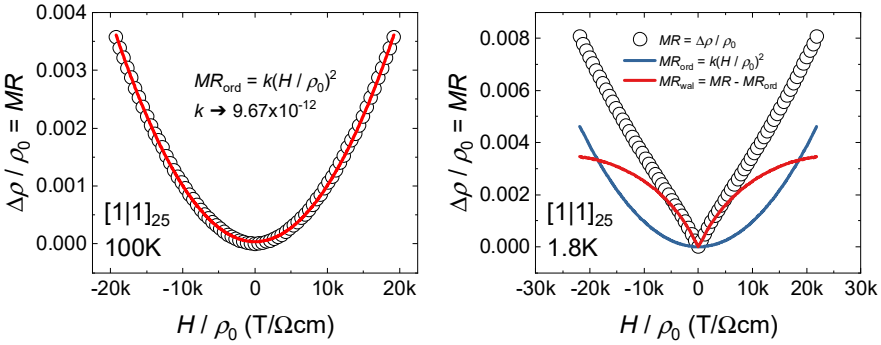

Figure 75. Graphical representation of the extraction process of *MR_{WAL} (H).*

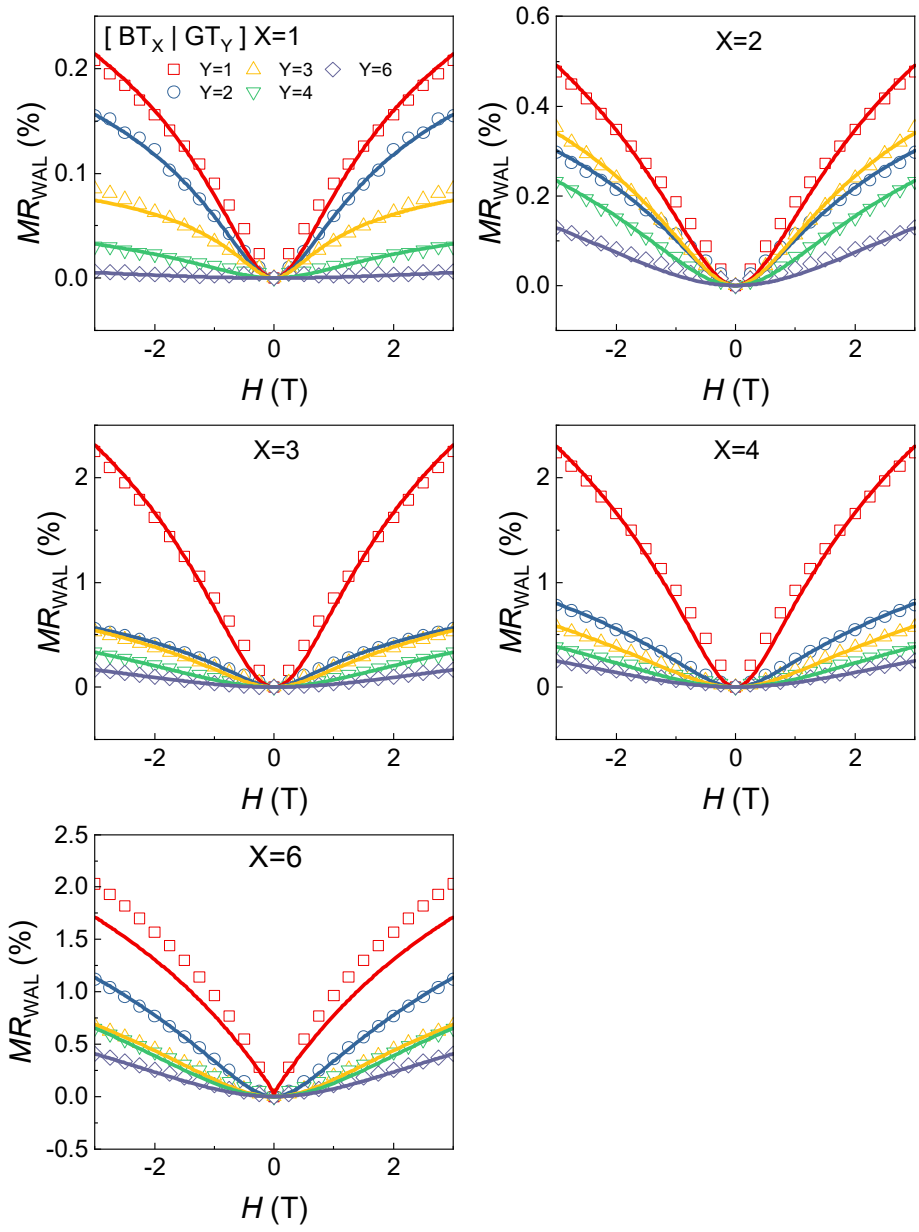

Figure 76. MR_{WAL} vs. H curves of [BT|GT] SLs.

There are several models which express the WAL according to the spin relaxation mechanism (Elliot-Yafet (EY) or D'yakonov-Perel (DP)) [20] and the dimensionality of the transport channel. The Fukuyama-Hoshino (FH) model has been selected to fit the $MR_{WAL}(H)$ considering the 3D transport and D'yakonov-Perel (DP) [157,159-163] mechanism in the [BT|GT] SLs. The used FH model [97,156,158,164-166] is expressed as below:

$$MR_{WAL}(H) = 100\rho_0 \frac{e^2}{2\pi^2\hbar}\sqrt{\frac{eH}{\hbar}}\left(\frac{1}{2\sqrt{1-\gamma}}\left[f_3\left(\frac{H}{B_-}\right) - f_3\left(\frac{H}{B_+}\right)\right] - f_3\left(\frac{H}{B_2}\right) - \sqrt{\frac{4B_{so}}{3H}}\left[\frac{1}{\sqrt{1-\gamma}}\left(\sqrt{t_+} - \sqrt{t_-}\right) + \sqrt{t} - \sqrt{t+1}\right]\right)$$

$$f_3(y) = \sum_{n=0}^{\infty}\left[2\left(n+1+\frac{1}{y}\right)^{\frac{1}{2}} - 2\left(n+\frac{1}{y}\right)^{\frac{1}{2}} - \left(n+\frac{1}{2}+\frac{1}{y}\right)^{-\frac{1}{2}}\right]$$

$$\gamma = \left[\frac{3g^*\mu_B H}{4eD(2B_{so}-B_0)}\right]^2$$

$$B_{\pm} = B_{\phi} + \frac{1}{3}(2B_{so}-B_0)\left(1 \pm \sqrt{1-\gamma}\right)$$

$$B_{\phi} = B_i + B_0$$

$$B_2 = B_i + \frac{1}{3}B_0 + \frac{4}{3}B_{so}$$

$$\mathrm{t} = \frac{3B_\phi}{2(2B_{so} - B_0)}$$

$$t_\pm = t + \frac{1}{2}\left(1 \pm \sqrt{1-\gamma}\right)$$

where $\hbar$ is the reduced Planck constant, B_x (x=*i*,*0*,ϕ, and *so*) is the characteristic field for inelastic scattering, remanent, dephasing, and spin-orbit interaction, g* is the effective Landé g factor, μ_B is Bohr magneton, and D is the diffusion coefficient. It can be seen that the fitting results (solid lines in Figure 80) using only two fitting parameters (B_ϕ and B_{so}) describe the experimental data (open circles in Figure 80) very well. The extracted parameters of B_ϕ and B_{so} are shown in Figure 81.

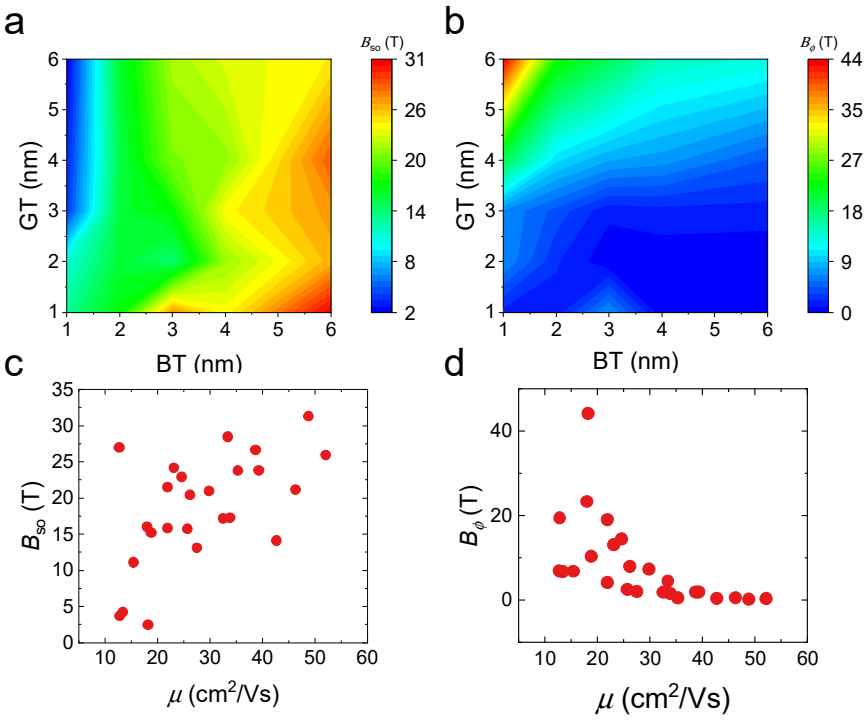

Figure 77. The extracted fitting parameters of the WAL fitting shown in Figure 80.

The B_{ϕ} decreases as the mobility increases implying that the dephasing mechanism is dominated by e-e scattering [156]. The B_{so} increases as the mobility increases implying the DP spin relaxation mechanism [159]. When the spin relaxation follows the DP mechanism, the Rashba constant, α_R can be calculated by the relationship of $\alpha_R = \sqrt{e\hbar^3 B_{so}}/m$ [157,161].

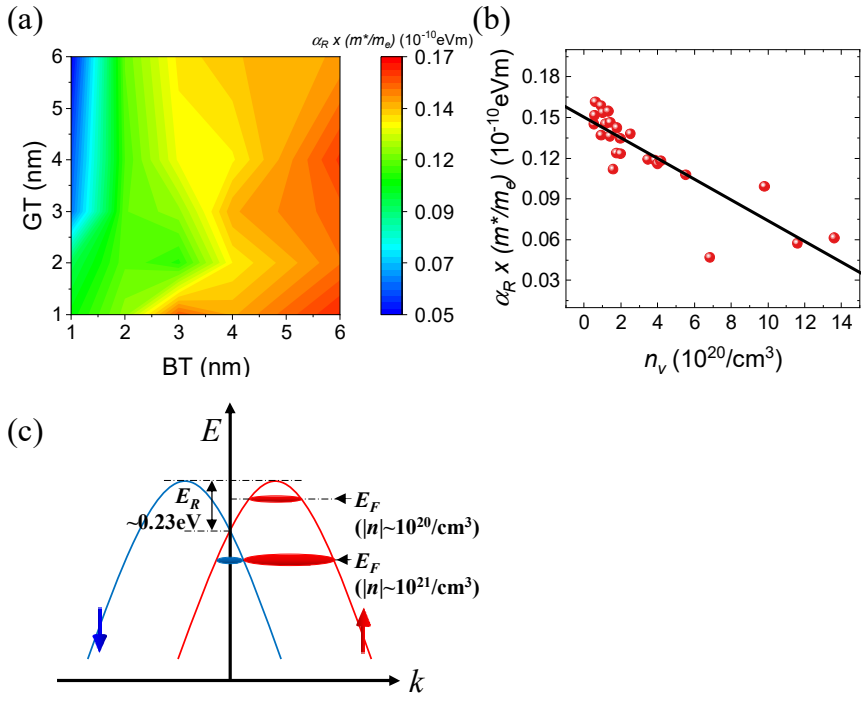

Figure 78. Calculated Rashba constant (α_R) from the WAL fitting parameter of [BT|GT] SLs.

The calculated α_R is shown in Figure 82 as a color map as a function of n. A linear relationship with a negative slope between α_R and n is confirmed. In the recent calculation of the spin Hall conductivity of GeTe [120], a relatively small spin Hall angle of only 0.01 was predicted despite a very large Rashba constant of 3.4 eV/Å in GeTe. This was due to the high charge conductivity of GeTe, and it was suggested that carrier density optimization is necessary to obtain a large spin Hall angle. In a similar vein, the observed carrier density

dependent α_R in [BT|GT] SLs might indicate the restoration of the Rashba constant reduced by the high p-type carrier density of GeTe. The schematic electronic band which shows a change of the Rashba splittings according to the carrier densities is represented in Figure 82(c). It shows that the Rashba spin splitting is reduced when the fermi energy exceeds the Rashba energy (~0.23 eV) [167].

5.4 Conclusion

We have systematically investigated the [BT|GT] SLs to reduce the carrier density to enhance the ferroelectric switching efficiency of GT. The observed compensation doping effect was enhanced as the mobile charges (the product of n and volume) of the BT and GT domains have been more the same, indicating a 1:1 compensation between charges of BT and GT induced by the charge transfer effect. The condition to acquire the maximal compensation effect of BT/GT ~ 3 and BT > 2 nm has been confirmed. These conditions can be generalized as follows: the compositional ratio, BT/GT is identical to the ratio of absolute carrier density of $|n_{BT}| / |p_{GT}|$ and the BT critical thickness of t_{BT} corresponds to the depletion length formed in the BT layer. With the WAL analysis, we have found that increasing α_R as carrier density decrease. It is associated with the restoration of the Rashba effect of GT as the fermi energy decrease to the Rashba energy. We expect our result is not only worthwhile for the spintronics applications which is our first motivation, but also for the thermoelectric applications which also suffer from the high carrier density of GT.

Bibliography

[1] J. E. Boschker, R. Wang, and R. Calarco, CrystEngComm **19**, 5324 (2017).

[2] R. A. Hein, J. W. Gibson, R. Mazelsky, R. C. Miller, and J. K. Hulm, Physical Review Letters **12**, 320 (1964).

[3] M. Wang and M. Rais-Zadeh, Journal of Micromechanics and Microengineering **27** (2017).

[4] D. H. Damon, M. S. Lubell, and R. Mazelsky, **28**, 520 (1967).

[5] D. Wu *et al.*, Journal of the American Chemical Society **136**, 11412 (2014).

[6] S.-J. Gong, F. Zheng, and A. M. Rappe, Physical Review Letters **121** (2018).

[7] D. Di Sante, P. Barone, R. Bertacco, and S. Picozzi, **25**, 509 (2013).

[8] S. Picozzi, Frontiers in Physics **2** (2014).

[9] H. Przybylińska, G. Springholz, R. T. Lechner, M. Hassan, M. Wegscheider, W. Jantsch, and G. Bauer, **112** (2014).

[10] H. J. Elmers *et al.*, **94** (2016).

[11] J. Krempaský *et al.*, Nature Communications **7**, 13071 (2016).

[12] J. Krempaský *et al.*, **94** (2016).

[13] E.-W. Du, S.-J. Gong, X. Tang, J. Chu, A. M. Rappe, and C. Gong, Nano Letters **20**, 7230 (2020).

[14] K. Taguchi, T. Yokoyama, and Y. Tanaka, **89** (2014).

[15] S. Sayed, S. Hong, and S. Datta, Scientific Reports **6**, 35658 (2016).

[16] J.-H. Lee, H.-J. Kim, J. Chang, S. H. Han, H. C. Koo, S. Sayed, S. Hong, and S. Datta, Scientific Reports **8** (2018).

[17] A. Fert, Reviews of Modern Physics **80**, 1517 (2008).

[18] *Handbook of Spintronics* (Springer Dordrecht, 1 edn.

[19] A. Hirohata, K. Yamada, Y. Nakatani, I.-L. Prejbeanu, B. Diény, P. Pirro, and B. Hillebrands, Journal of Magnetism and Magnetic Materials **509**, 166711 (2020).

[20] I. Žutić, J. Fabian, and S. Das Sarma, Reviews of Modern Physics **76**, 323 (2004).

[21] B. Dieny *et al.*, Nature Electronics **3**, 446 (2020).

[22] Z. Guo, J. Yin, Y. Bai, D. Zhu, K. Shi, G. Wang, K. Cao, and W. Zhao, Proceedings of the IEEE **109**, 1398 (2021).

[23] Y. A. Bychkov and E. I. Rashba, Journal of physics C: Solid state physics **17**, 6039 (1984).

[24] H. C. Koo *et al.*, Advanced Materials, 2002117 (2020).

[25] A. Manchon, H. C. Koo, J. Nitta, S. M. Frolov, and R. A. Duine, Nature Materials **14**, 871 (2015).

[26] K. Ishizaka *et al.*, Nature Materials **10**, 521 (2011).

[27] Z. Zhong, L. Si, Q. Zhang, W.-G. Yin, S. Yunoki, and K. Held, **2**, n/a (2015).

[28] V. Garcia *et al.*, Science **327**, 1106 (2010).

[29] K. Frohna *et al.*, Nature Communications **9** (2018).

[30] N. Yamada, E. Ohno, K. Nishiuchi, N. Akahira, and M. Takao, Journal of Applied Physics **69**, 2849 (1991).

[31] N. Yamada and T. Matsunaga, Journal of Applied Physics **88**, 7020 (2000).

[32] N. N. Eliseev, A. V. Kiselev, V. V. Ionin, V. A. Mikhalevsky, A. A. Burtsev, M. A. Pankov, D. N. Karimov, and A. A. Lotin, Results in Physics **19** (2020).

[33] P. Kumar, R. Thangaraj, and T. S. Sathiaraj, physica status solidi (a) **208**, 838 (2011).

[34] G. Bruns, P. Merkelbach, C. Schlockermann, M. Salinga, M.

Wuttig, T. D. Happ, J. B. Philipp, and M. Kund, Applied Physics Letters **95** (2009).

[35] L. Perniola *et al.*, IEEE Electron Device Letters **31**, 488 (2010).

[36] G. C. Sosso, G. Miceli, S. Caravati, J. Behler, and M. Bernasconi, Physical Review B **85** (2012).

[37] P. Borodulin, N. El-Hinnawy, C. R. Padilla, A. Ezis, M. R. King, D. R. Johnson, D. T. Nichols, and R. M. Young, in *2017 IEEE MTT-S International Microwave Symposium (IMS)*2017), pp. 285.

[38] M. Hong, J. Zou, and Z. G. Chen, Adv Mater **31**, e1807071 (2019).

[39] S. Perumal, S. Roychowdhury, and K. Biswas, Journal of Materials Chemistry C **4**, 7520 (2016).

[40] X. Zhang, Z. Bu, S. Lin, Z. Chen, W. Li, and Y. Pei, Joule **4**, 986 (2020).

[41] J. E. Boschker, E. Tisbi, E. Placidi, J. Momand, A. Redaelli, B. J. Kooi, F. Arciprete, and R. Calarco, AIP Advances **7** (2017).

[42] Y. Saito, P. Fons, A. V. Kolobov, and J. Tominaga, physica status solidi (b) **252**, 2151 (2015).

[43] J. Liu, Journal of Materials Chemistry C **10**, 9891 (2022).

[44] I. Hilmi, A. Lotnyk, J. W. Gerlach, P. Schumacher, and B. Rauschenbach, Materials & Design **168**, 107657 (2019).

[45] N. Bathaei, B. Weng, and H. Sigmarsson, Materials Science in Semiconductor Processing **96**, 73 (2019).

[46] C. Rinaldi *et al.*, **4**, 032501 (2016).

[47] A. V. Kolobov, D. J. Kim, A. Giussani, P. Fons, J. Tominaga, R. Calarco, and A. Gruverman, **2**, 066101 (2014).

[48] R. Wang, J. E. Boschker, E. Bruyer, D. D. Sante, S. Picozzi, K. Perumal, A. Giussani, H. Riechert, and R. Calarco, **118**, 29724 (2014).

[49] X. Sun, B. Yu, G. Ng, and M. Meyyappan, The Journal of Physical Chemistry C **111**, 2421 (2007).

[50] S. Meister, H. Peng, K. McIlwrath, K. Jarausch, X. F. Zhang, and Y. Cui, Nano letters **6**, 1514 (2006).

[51] P. Krogstrup, N. L. Ziino, W. Chang, S. M. Albrecht, M. H. Madsen, E. Johnson, J. Nygard, C. M. Marcus, and T. S. Jespersen, Nat Mater **14**, 400 (2015).

[52] J. Kampmeier, S. Borisova, L. Plucinski, M. Luysberg, G. Mussler, and D. Grützmacher, Crystal Growth & Design **15**, 390 (2015).

[53] Y. J. Lin, K. Jiménez-García, and I. B. Spielman, Nature **471**, 83 (2011).

[54] G. Liu, S.-L. Zhu, S. Jiang, F. Sun, and W. M. Liu, Physical Review A **82**, 053605 (2010).

[55] R. Liao, Y. Yi-Xiang, and W.-M. Liu, Physical Review Letters **108**, 080406 (2012).

[56] X.-L. Qi and S.-C. Zhang, Reviews of Modern Physics **83**, 1057 (2011).

[57] Y. Sun, Y. Zhang, C. Felser, and B. Yan, Physical Review Letters **117**, 146403 (2016).

[58] I. M. Miron *et al.*, Nature **476**, 189 (2011).

[59] L. Liu, C.-F. Pai, Y. Li, H. W. Tseng, D. C. Ralph, and R. A. Buhrman, Science **336**, 555 (2012).

[60] L. Liu, O. J. Lee, T. J. Gudmundsen, D. C. Ralph, and R. A. Buhrman, Physical Review Letters **109**, 096602 (2012).

[61] J. Kim, J. Sinha, M. Hayashi, M. Yamanouchi, S. Fukami, T. Suzuki, S. Mitani, and H. Ohno, Nature Materials **12**, 240 (2012).

[62] C. Nayak, S. H. Simon, A. Stern, M. Freedman, and S. Das Sarma, Reviews of Modern Physics **80**, 1083 (2008).

[63] A. C. Potter and P. A. Lee, Physical Review B **83**, 184520 (2011).

[64] N. H. D. Khang, Y. Ueda, and P. N. Hai, Nature Materials **17**, 808 (2018).

[65] C. R. Ast, J. Henk, A. Ernst, L. Moreschini, M. C. Falub, D. Pacilé, P. Bruno, K. Kern, and M. Grioni, Physical Review Letters **98**, 186807 (2007).

[66] K. Ishizaka *et al.*, Nature Materials **10**, 521 (2011).

[67] D. Di Sante, P. Barone, R. Bertacco, and S. Picozzi, Advanced Materials **25**, 509 (2013).

[68] J. Han, A. Richardella, S. A. Siddiqui, J. Finley, N. Samarth, and L. Liu, Physical Review Letters **119**, 077702 (2017).

[69] J. C. R. Sánchez, L. Vila, G. Desfonds, S. Gambarelli, J. P. Attané, J. M. De Teresa, C. Magén, and A. Fert, Nature Communications **4**, 2944 (2013).

[70] A. Stern and N. H. Lindner, Science **339**, 1179 (2013).

[71] S. Picozzi, Frontiers in Physics **2** (2014).

[72] A. Narayan, Physical Review B **92**, 220101 (2015).

[73] K. Schubert and H. Fricke, ZEITSCHRIFT FUR METALLKUNDE **44**, 457 (1953).

[74] T. Chattopadhyay, J. X. Boucherle, and H. G. vonSchnering, Journal of Physics C: Solid State Physics **20**, 1431 (1987).

[75] M. J. Polking *et al.*, Nature Materials **11**, 700 (2012).

[76] J. Krempaský *et al.*, Physical Review B **94**, 205111 (2016).

[77] K. M. Rabe and J. D. Joannopoulos, Physical Review B **36**, 6631 (1987).

[78] M. Liebmann *et al.*, Advanced Materials **28**, 560 (2016).

[79] V. L. Deringer, M. Lumeij, and R. Dronskowski, The Journal of Physical Chemistry C **116**, 15801 (2012).

[80] R. Wang, J. E. Boschker, E. Bruyer, D. D. Sante, S. Picozzi, K. Perumal, A. Giussani, H. Riechert, and R. Calarco, The Journal of

Physical Chemistry C **118**, 29724 (2014).

[81] B. L. Altshuler, D. Khmel'nitzkii, A. I. Larkin, and P. A. Lee, Physical Review B **22**, 5142 (1980).

[82] S. Datta, *Electronic Transport in Mesoscopic Systems* (Cambridge University Press, 1997).

[83] S. Hikami, A. I. Larkin, and Y. Nagaoka, Progress of Theoretical Physics **63**, 707 (1980).

[84] J. Hu, J. Y. Liu, and Z. Q. Mao, Journal of Physics: Condensed Matter **26**, 095801 (2014).

[85] J. M. Ziman, *Electrons and Phonons: The Theory of Transport Phenomena in Solids* (OUP Oxford, 1960).

[86] S. W. Cho, M. Lee, S. Woo, K. Yim, S. Han, W. S. Choi, and S. Lee, Scientific Reports **8**, 5739 (2018).

[87] A. D. Caviglia, M. Gabay, S. Gariglio, N. Reyren, C. Cancellieri, and J. M. Triscone, Physical Review Letters **104**, 126803 (2010).

[88] G. Herranz *et al.*, **6**, 6028 (2015).

[89] D. Pesin and L. Balents, Nat Phys **6**, 376 (2010).

[90] Q. Cui *et al.*, Physical Review Letters **117**, 176603 (2016).

[91] X. Wan, A. M. Turner, A. Vishwanath, and S. Y. Savrasov, Physical Review B **83**, 205101 (2011).

[92] M. N. Baibich, J. M. Broto, A. Fert, F. N. Van Dau, F. Petroff, P. Etienne, G. Creuzet, A. Friederich, and J. Chazelas, Physical Review Letters **61**, 2472 (1988).

[93] M. Koyano, S. Horisaka, H. Negishi, M. Sasaki, M. Inoue, N. Suzuki, and K. Motizuki, Journal of Low Temperature Physics **78**, 141 (1990).

[94] A. Urushibara, Y. Moritomo, T. Arima, A. Asamitsu, G. Kido, and Y. Tokura, Physical Review B **51**, 14103 (1995).

[95] A. H. Edwards, A. C. Pineda, P. A. Schultz, M. G. Martin, A. P.

Thompson, H. P. Hjalmarson, and C. J. Umrigar, Physical Review B **73**, 045210 (2006).

[96] M. Wuttig, D. Lüsebrink, D. Wamwangi, W. Wełnic, M. Gilleßen, and R. Dronskowski, Nature Materials **6**, 122 (2006).

[97] H. Fukuyama and K. Hoshino, Journal of the Physical Society of Japan **50**, 2131 (1981).

[98] A. G. A. B. L. Altshuler, A. I. Larkin, and D. E. Khmelnitskii, Sov. Phys. JETP **54** (1981).

[99] A. Kawabata, Journal of the Physical Society of Japan **49**, 628 (1980).

[100] X. Chen, D. Parker, and D. J. Singh, Scientific Reports **3**, 3168 (2013).

[101] K. Chang *et al.*, Science **353**, 274 (2016).

[102] S. Datta and B. Das, Applied Physics Letters **56**, 665 (1990).

[103] H. C. Koo, J. H. Kwon, J. Eom, J. Chang, S. H. Han, and M. Johnson, Science **325**, 1515 (2009).

[104] J. Wunderlich, B.-G. Park, A. C. Irvine, L. P. Zârbo, E. Rozkotová, P. Nemec, V. Novák, J. Sinova, and T. Jungwirth, Science **330**, 1801 (2010).

[105] A. Sasaki, S. Nonaka, Y. Kunihashi, M. Kohda, T. Bauernfeind, T. Dollinger, K. Richter, and J. Nitta, Nature Nanotechnology **9**, 703 (2014).

[106] W. Y. Choi, H. J. Kim, J. Chang, S. H. Han, H. C. Koo, and M. Johnson, Nat Nanotechnol **10**, 666 (2015).

[107] A. Manchon and S. Zhang, Physical Review B **78** (2008).

[108] P. M. Haney, H.-W. Lee, K.-J. Lee, A. Manchon, and M. D. Stiles, Physical Review B **87** (2013).

[109] L. Wang, R. J. Wesselink, Y. Liu, Z. Yuan, K. Xia, and P. J. Kelly, Phys Rev Lett **116**, 196602 (2016).

[110] S. C. Baek *et al.*, Nat Mater **17**, 509 (2018).
[111] V. P. Amin, J. Zemen, and M. D. Stiles, Phys Rev Lett **121**, 136805 (2018).
[112] I. M. Miron *et al.*, Nature **476**, 189 (2011).
[113] L. Liu, C.-F. Pai, Y. Li, H. Tseng, D. Ralph, and R. Buhrman, Science **336**, 555 (2012).
[114] S.-W. Lee and K.-J. Lee, Proceedings of the IEEE **104**, 1831 (2016).
[115] Y. L. Chen *et al.*, Nature Physics **9**, 704 (2013).
[116] A. Narayan, Physical Review B **92** (2015).
[117] T. Chattopadhyay and J. Boucherle, Journal of Physics C: Solid State Physics **20**, 1431 (1987).
[118] M. J. Polking *et al.*, Nature Materials **11**, 700 (2012).
[119] W. Zhang, Z. Teng, H. Zeng, H. Zhang, J. Železný, and W. Zhang, physica status solidi (b), 2000143 (2020).
[120] H. Wang, P. Gopal, S. Picozzi, S. Curtarolo, M. Buongiorno Nardelli, and J. Sławińska, npj Computational Materials **6** (2020).
[121] C. O. Avci, K. Garello, M. Gabureac, A. Ghosh, A. Fuhrer, S. F. Alvarado, and P. Gambardella, Physical Review B **90** (2014).
[122] N. Roschewsky, E. S. Walker, P. Gowtham, S. Muschinske, F. Hellman, S. R. Bank, and S. Salahuddin, Physical Review B **99** (2019).
[123] L. Liu, T. Moriyama, D. C. Ralph, and R. A. Buhrman, Phys Rev Lett **106**, 036601 (2011).
[124] J. Yu *et al.*, Nat Mater **18**, 29 (2019).
[125] A. Manchon, J. Železný, I. M. Miron, T. Jungwirth, J. Sinova, A. Thiaville, K. Garello, and P. Gambardella, Reviews of Modern Physics **91** (2019).
[126] X. Qiu *et al.*, Nat Nanotechnol **10**, 333 (2015).

[127] K. U. Demasius, T. Phung, W. Zhang, B. P. Hughes, S. H. Yang, A. Kellock, W. Han, A. Pushp, and S. S. P. Parkin, Nat Commun **7**, 10644 (2016).
[128] H. An, Y. Kageyama, Y. Kanno, N. Enishi, and K. Ando, Nat Commun **7**, 13069 (2016).
[129] S. Fukami, T. Anekawa, C. Zhang, and H. Ohno, Nat Nanotechnol **11**, 621 (2016).
[130] M. He, H. Sun, and Q. L. He, Frontiers of Physics **14** (2019).
[131] S.-H. Yang, R. Naaman, Y. Paltiel, and S. S. P. Parkin, Nature Reviews Physics **3**, 328 (2021).
[132] Q. L. He, T. L. Hughes, N. P. Armitage, Y. Tokura, and K. L. Wang, Nature Materials **21**, 15 (2021).
[133] D. D. Awschalom and M. E. Flatté, Nature Physics **3**, 153 (2007).
[134] J. Puebla, J. Kim, K. Kondou, and Y. Otani, Communications Materials **1** (2020).
[135] A. Hoffmann and S. D. Bader, Physical Review Applied **4** (2015).
[136] M. S. Bahramy, R. Arita, and N. Nagaosa, Physical Review B **84** (2011).
[137] H. Murakawa, M. S. Bahramy, M. Tokunaga, Y. Kohama, C. Bell, Y. Kaneko, N. Nagaosa, H. Y. Hwang, and Y. Tokura, Science **342**, 1490 (2013).
[138] S. Varotto *et al.*, Nature Electronics **4**, 740 (2021).
[139] J. Krempaský *et al.*, Journal of Physics and Chemistry of Solids **128**, 237 (2019).
[140] Y.-H. Meng, W. Bai, H. Gao, S.-J. Gong, J.-Q. Wang, C.-G. Duan, and J.-H. Chu, Nanoscale **9**, 17957 (2017).
[141] J. Krempaský *et al.*, Physical Review Research **2** (2020).
[142] J. Jeon *et al.*, NPG Asia Materials **13** (2021).
[143] C. Rinaldi *et al.*, Nano Letters **18**, 2751 (2018).

[144] A. Edwards, A. Pineda, P. Schultz, M. Martin, A. Thompson, H. Hjalmarson, and C. Umrigar, Physical Review B **73** (2006).

[145] V. L. Deringer, M. Lumeij, and R. Dronskowski, **116**, 15801 (2012).

[146] P. Nukala, M. Ren, R. Agarwal, J. Berger, G. Liu, A. T. C. Johnson, and R. Agarwal, Nature Communications **8**, 15033 (2017).

[147] K. Jeong, H. Lee, C. Lee, L. H. Wook, H. Kim, E. Lee, and M.-H. Cho, Applied Materials Today **24** (2021).

[148] J. Krumrain, G. Mussler, S. Borisova, T. Stoica, L. Plucinski, C. M. Schneider, and D. Grützmacher, Journal of Crystal Growth **324**, 115 (2011).

[149] H. Zhang, D. T. Yimam, S. De Graaf, J. Momand, P. A. Vermeulen, Y. Wei, B. Noheda, and B. J. Kooi, ACS Nano **15**, 2869 (2021).

[150] Y. L. Chen *et al.*, Science **325**, 178 (2009).

[151] S. W. Cho, K.-C. Kim, S. K. Kim, B.-K. Cheong, J.-S. Kim, and S. Lee, Journal of Alloys and Compounds **723**, 942 (2017).

[152] S. W. Cho, M. Lee, S. Woo, K. Yim, S. Han, W. S. Choi, and S. Lee, Scientific Reports **8** (2018).

[153] M. Lee, S. W. Cho, Y. Yi, and S. Lee, Journal of Alloys and Compounds **800**, 81 (2019).

[154] Y. Liu, E. Mu, Z. Wu, Z. Che, F. Sun, X. Fu, F. Wang, X. Wang, and Z. Hu, Nano Converg **7**, 8 (2020).

[155] H. Nakamura, D. Huang, J. Merz, E. Khalaf, P. Ostrovsky, A. Yaresko, D. Samal, and H. Takagi, Nat Commun **11**, 1161 (2020).

[156] J. J. Lin and J. P. Bird, Journal of Physics: Condensed Matter **14**, R501 (2002).

[157] T. Koga, J. Nitta, T. Akazaki, and H. Takayanagi, Physical Review Letters **89**, 046801 (2002).

[158] Y. Nakazawa, M. Uchida, S. Nishihaya, M. Ohno, S. Sato, and M. Kawasaki, Physical Review B **103** (2021).

[159] A. D. Caviglia, M. Gabay, S. Gariglio, N. Reyren, C. Cancellieri, and J. M. Triscone, Physical Review Letters **104** (2010).

[160] C. Niu, G. Qiu, Y. Wang, Z. Zhang, M. Si, W. Wu, and P. D. Ye, Physical Review B **101** (2020).

[161] S. Takasuna, J. Shiogai, S. Matsuzaka, M. Kohda, Y. Oyama, and J. Nitta, Physical Review B **96** (2017).

[162] H. Liang, L. Cheng, L. Wei, Z. Luo, G. Yu, C. Zeng, and Z. Zhang, Physical Review B **92**, 075309 (2015).

[163] W. Han, R. K. Kawakami, M. Gmitra, and J. Fabian, Nat Nanotechnol **9**, 794 (2014).

[164] E. R. Viana, G. M. Ribeiro, A. G. D. Oliveira, M. L. Peres, R. M. Rubinger, and C. P. L. Rubinger, Materials Research **15**, 530 (2012).

[165] S. T. Lim, L. Hui, J. F. Bi, and K. L. Teo, Journal of Applied Physics **110** (2011).

[166] M. L. Peres, V. A. Chitta, N. F. Oliveira, D. K. Maude, P. H. O. Rappl, A. Y. Ueta, and E. Abramof, Physical Review B **79** (2009).

[167] P. C. Verpoort and V. Narayan, Journal of Physics: Condensed Matter **32**, 355704 (2020).

초 록

전자재료에서 신소재의 개발은 단순히 기존 소자의 성능을 향상시키기도 하지만, 완전히 새로운 기능을 가진 신소자의 개발을 이끌기도 한다. 강유전 라쉬바 반도체는 (Ferrolectric Rashba Semiconductors) 이러한 재료 중 하나로, 강유전 분극을 통해 라쉬바 효과를 통제할 수 있는 특징을 가진다. 강유전성과 결합된 라쉬바 효과를 이용하면 비휘발성-스핀트랜지스터 (Non-volatile-spintransistors)와 같은 새로운 스핀트로닉스 (Spintronics) 소자 개발을 가능하게 한다. 대표적 강유전 라쉬바 반도체인, 텔루륨화 게르마늄 (GeTe)은 단순한 조성과 매우 큰 라쉬바 효과 (라쉬바상수, α_R=~4.3 eVÅ)로 인해 유망한 스핀트로닉스 응용재료이다.

하지만, 관련 연구는 이론적 계산과 광학적 라쉬바 효과 검증에 집중되어 있으며, 실제 스핀트로닉스 응용을 위한 전기적 특성에 대한 연구는 전체 연구의 10 %미만이다. 이는 강유전 라쉬바 반도체로써의 GeTe 연구의 높은 학문적 가치에 비해, 부족한 응용성을 반영한 결과로 보인다. GeTe의 응용을 막는 재료적 한계는, GeTe는 강유전체이면서 금속과 같은 높은 전도성을 함께 지닌다는 것이다. GeTe가 가지는 10^{20} /cm^3 이상의 높은 홀농도는 강유전 스위칭 효율을 낮추며 Rashba effect에도 악영향을 미친다. 본 논문에서는, 강유전 라쉬바 반도체인 GeTe의 응용성을 향상시키기 위한 목적의 연구를 진행한다.

열기화증착법으로 성장된 고품질의 에피택시 GeTe 박막을 사용하여, 자기저항분석 (Magnetoresistance Analysis) 그리고 이차홀저항분석 (Second harmonic Hall Resistance Analysis)와 같은 전기적 측정 및 분석법을 기반으로 GeTe의 라쉬바 효과를 검증하였다. 또한, n-타입 위상절연체 (Topological Insulator)인 텔루륨화 비스무트 (Bi_2Te_3)와의 초격자 (Superlattice) 형성을 통하여 GeTe의 전하밀도를 1/10배로 감소하면서 강유전 스위칭 효율과 라쉬바 효과를 향상시킨 연구를 소개한다. GeTe 박막의 성장부터, 기초특성 분석, 응용특성 분석, 그리고 전하밀도 감소를 위한 초격자 연구까지, 강유전 라쉬바 반도체로써 GeTe 활용을 위한 포괄적인 연구를 담은 본 논문은, 현재 정체되어 있는 강유전 라쉬바 반도체의 스핀트로닉스로의 응용에 많은 영감을 제공할 수 있을 것으로 기대된다.

주요어: 강유전 라쉬바 반도체, 텔루륨화 게르마늄, 스핀트로닉스, 스핀-궤도 결합, 전하운송효과, 스핀운송효과, 초격자, 에피택시 박막 성장
학 번: 2018-30391